Crush Behavior of Flanged Plates Under Localized In-Plane Loadings

by

Mohamed Yahiaoui

Master of Science in Mechanical Engineering
Massachusetts Institute of Technology
(1988)

Mechanical Engineer
Massachusetts Institute of Technology
(1992)

Submitted to the Department of Ocean Engineering in partial fulfillment of the requirements for the degree of

DOCTOR OF PHILOSOPHY

at the

MASSACHUSETTS INSTITUTE OF TECHNOLOGY

January, 1996

Author ....
Department of Ocean Engineering
January, 1996

Certified by ....
Tomasz Wierzbicki, Professor of Applied Mechanics
Thesis Supervisor

Accepted by ....
Professor A. Douglas Carmichael
Chairman, Ocean Engineering Department Graduate Committee

Crush Behavior of Flanged Plates Under Localized In-Plane Loadings
by

Mohamed Yahiaoui

Submitted to the Department of Ocean Engineering on January 25, 1996, in partial fulfillment of the requirements for the degree of
Doctor of Philosophy

Abstract

An analytical approximation for the crushing resistance of flanged semi-circular plates subjected to localized in-plane loadings has been derived. Small-scale experiments were conducted to validate the theoretical results. The loading was applied quasi-statically by a cylindrical indenter at the symmetry line of the plate.

This work provides a consistent computational model which leads to a theoretical prediction of the load-deflection characteristics. It provides the link between the two phases of the plate response: pre-failure (in the sense of maximum load) and post-failure phases. During the pre-failure phase, the plate undergoes pre-buckling, buckling, and post-buckling stages. Once the point of maximum strength is reached in the post-buckling stage, the post-failure phase starts. This process is characterized by rapidly falling load due to plastic folding with large strains (up to rupture strain of the material) and large rotations of plate elements. Energy methods are used to analyze the elastic pre- and post-buckling response of the plate. Ultimate strength is calculated, using the membrane yield criterion. Limit analysis, applied incrementally up to large displacements and rotations, is employed in the post-failure range.

The analytical predictions were compared to the experimental results and shown to overestimate the peak force by about 15%. A comparison of the crushing loads in the post-failure phase was also made between the analytical model and test results. The correlation is within -5% to +17% depending on the indenter's radius. Possible causes of discrepancies are commented upon and a preliminary discussion on an alternative model is presented. Finally, indentation tests of flanged rectangular plates are described. This experimental study revealed good correlation with analytical results independently developed by Choi *et. al.* Their model predicts loads only 5-15% higher than experimental results.

The findings of this study prove important in the understanding of the overall ability of vehicle structures, such as ships, submarines, and aircraft, to withstand local damage during accidental loads. For example, the flanged rectangular plate model characterizes the behavior in the flat bottom region of both conventional and unidirectionally stiffened double hull ships during grounding accidents. The flanged circular plate model describes the behavior in the bilge area and provides estimates of the strength of submarine bulkheads in collisions or aircraft fuselages subject to crash landings.

Thesis Supervisor: Tomasz Wierzbicki
Title: Professor of Applied Mechanics, Department of Ocean Engineering

Acknowledgments

My thanks begin with Professor Tomasz Wierzbicki, my thesis advisor. I am very grateful not only for his guidance, insight, support and financial assistance but also for the opportunity to work in the unique learning environment that he created: the Joint MIT-Industry Program on Tanker Safety.

Many thanks to Professor Frank McClintock for his expertise, time and seemingly limitless patience and for providing me with all the advice and support critical to completing this degree. I am indebted to him for all of his constructive criticism.

I would also like to thank Professor Koichi Masubuchi. His comments and suggestions were very helpful towards the completion of this thesis.

I offer my most sincere gratitude to Professors Dick Yue, Kamal Youcef-Toumi, Neville Hogan, David Hardt, and David Gossard, for providing me during the rough times with much needed financial support throughout enjoyable and rewarding teaching assistantships.

Sincere thanks are extended to the friends and colleagues, too numerous to be listed here, that have all contributed in their own distinct and subtle ways to further enhance my educational experience at MIT. My greatest appreciation to each one of you.

A very special thanks to Danielle Guichard-Ashbrook of the International Students Office for assistance and inspiration far beyond the call of duty.

For helping me navigate the sea of bureaucracy, I thank Leslie Regan of the Mechanical Engineering Department and Teresa Coates of the Ocean Engineering Department.

Even though thanks do not even begin to repay the debt I have accumulated, much heartfelt thanks to you, Hassiba, for your help, companionship and love which made the

difference for the completion of this thesis and kept some sort of balance in my life. I am truly thankful for her presence in my life.

Last, but not least, I wish to thank my parents, Malika and Ali, who made it all possible and kept me going with their unconditional love, support and encouragements. I could not have done it without you, and best of all, I can tell you now that I have graduated: I am finally done!

To you my dear parents, I dedicate this thesis.

Table of Contents

List of Figures

List of Tables

Chapter 1

Introduction

1.1 The Need for Study of Flanged Circular and Rectangular Plates

For years, the commercial shipbuilding industry has operated under a set of design standards which are meant to ensure the safe operation of vessels under normal operating conditions. To date, still, ship design practices do not take into account extreme loads such as large impact forces and concentrated loads due to collision and grounding accidents.

With the increased carrying capacity of tank vessels (more than 500,000 DWT for the Very Large Crude Carriers), the dangers of transporting large amounts of oil, chemicals, and other hazardous bulk cargos cannot be ignored anymore. Large oil spills and environmental and ecological adverse effects when grounding or collision accidents occur have become a pressing problem.

Now, the maritime industry which came under severe public scrutiny in the aftermath of the grounding of the tanker EXXON VALDEZ in Alaska's Prince William Sound, is forced to address the issue of vessel performance in grounding and collision. In the United States, this spill lead to increased government regulation through the passage of the Oil Pollution Act of 1990 (OPA 90) mandating that petroleum product cargo ships operating

in U.S. waters will be of double hull construction, or designs of equivalent protection, by January 1, 2015.

OPA 90, along with the ever increasing environment importance, triggered a tremendous amount of research activity in the international community. One major research contribution is the Joint MIT-Industry Project on Tanker Safety launched on July 1, 1992 in the Department of Ocean Engineering at the Massachusetts Institute of Technology. The overall objective of the program has been to develop extensive theoretical and experimentally-validated engineering knowledge in the area of structural mechanics necessary to assess the extent of grounding damage to oil tankers for a variety of hull types and grounding scenarios. The interested reader is refered to Wierzbicki, Yahiaoui, and Sinmao (1994) for the details of the research activities within the project.

The ability of a ship to withstand damage during grounding accidents (which translates directly into tons of oil outflowing in the ocean) depends greatly on the crushing strength of the ship's hull. The crushing strength of the hull comes from a resistance to the longitudinal cutting/tearing of the bottom plating and supporting stiffeners as well as from vertical indentation into longitudinal and transverse framing. The present work addresses the initiation of local damage due to vertical indentation.

1.2 Previous Work

Consistent with the distinction between the two aspects of the damage process, described above, the publications dealing with the mechanics of ship grounding can be divided into two categories: Those studying cutting of plates by a wedge and those devoted to vertical indentation of a punch into a plate or stiffened panel.

Quasi-static and drop-hammer tests in which a rigid rounded-nose wedge was pushed into a plate along an axis parallel to the plate surface have been performed by Akita et al.

(1972), Akita and Kitamura (1972), Vaughan (1979, 1980), Woisin (1982), Jones and Jouri (1987), Goldfinch (1986), Prentice (1986), and Lu and Calladine (1990). This type of research has been proven useful in identifying some important factors which control the resistance force in grounding, including plate thickness, cut length, and ultimate stress of the material. Vaughan (1978), applied the results of the plate cutting experiment to the grounding resistance of ships, following an earlier idea by Minorsky (1959). He postulated that the energy absorption during the grounding process can be approximated by the total volume of damage and proportionality constants determined empirically from the data of Akita and Kitamura (1972). Recently, at MIT several aspects related to this type of research have been extensively studied from the theoretical and experimental point of view. Numerous reports were published during the period from July 1992 to July 1995 under the Joint MIT-Industry Project on Tanker Safety.

The second category of experiments in which a rigid punch was pressed into a stiffened plate along an axis normal to the plate surface are exemplified by the work of Ueda et al. (1978), Arita and Aoki (1985), and Ito *et al.* (1984, 1985, 1986). Finite element analyses were also performed and the two approaches were correlated with good results.

At MIT a theoretical/experimental study was initiated by Culberston-Driscoll (1992) to analytically predict local crushing of flat rectangular flanged plates. A simple model was developed in which the plastic behavior of deforming web girders was viewed as a sequence of "frozen" deformation modes where the plastic zone size was treated as a parameter. Goksoyr (1994) performed a very thorough numerical study of the elastic buckling and the plastic crushing deformation modes using the finite element code ABAQUS. Tests on local crushing of flat rectangular flanged plates were run by Yahiaoui *et al.* (1994). Based on the results of the numerical and experimental work, Choi *et al.* (1994) modified and improved the solution proposed by Culberston-Driscoll (1992). Their

12

new model predicting the load-deflection of a flat rectangular flanged plate subjected to local in-plane crushing loads showed values only 5-15% higher than experimental results. These results showed that a relatively simple analytical solution provides an accuracy at least equal to or surpassing the one of finite element solution.

1.3 Aim of Present Study

The objective of this work is to assess the crushing behavior of flanged semi-circular plates under localized in-plane loadings. A consistent computational model which leads to a theoretical prediction of the load-deflection characteristics is developed. The curved geometry is of great importance in the study of crushing strength of ships in the surroundings of the bilge area (See Figs. 1.1 and 1.2). Such types of damage could occur while under way, docking, maneuvering, turning, and drifting due to loss of steering, power, etc.

This work, will also find a direct application in submarines and aircraft structures. It provides an estimate of the strength of submarine bulkheads in collisions and of aircraft fuselages subject to crash landings.

Small-scale experiments are conducted to validate the theoretical results. Both semi-circular and rectangular flanged plates are tested. The results from the rectangular flanged plates tests are compared to the analytical findings independently developed by Choi *et al* (1994).
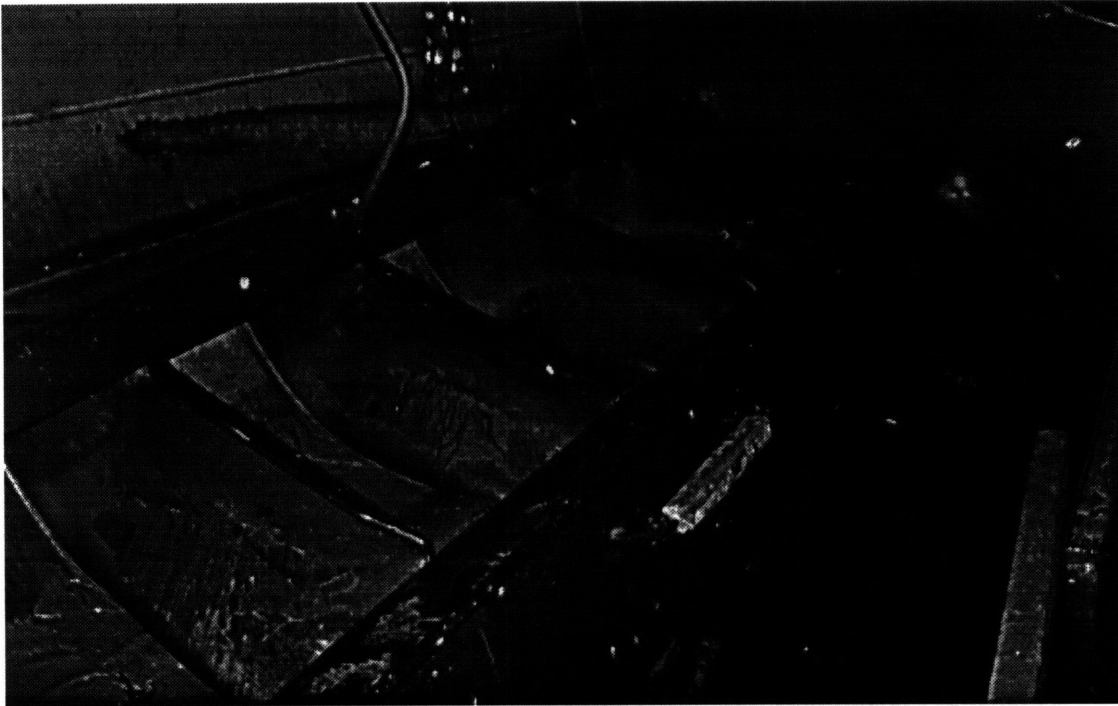
Figure 1.1: Photograph of Damaged Ship Bilge Area

Shell deflection 250mm
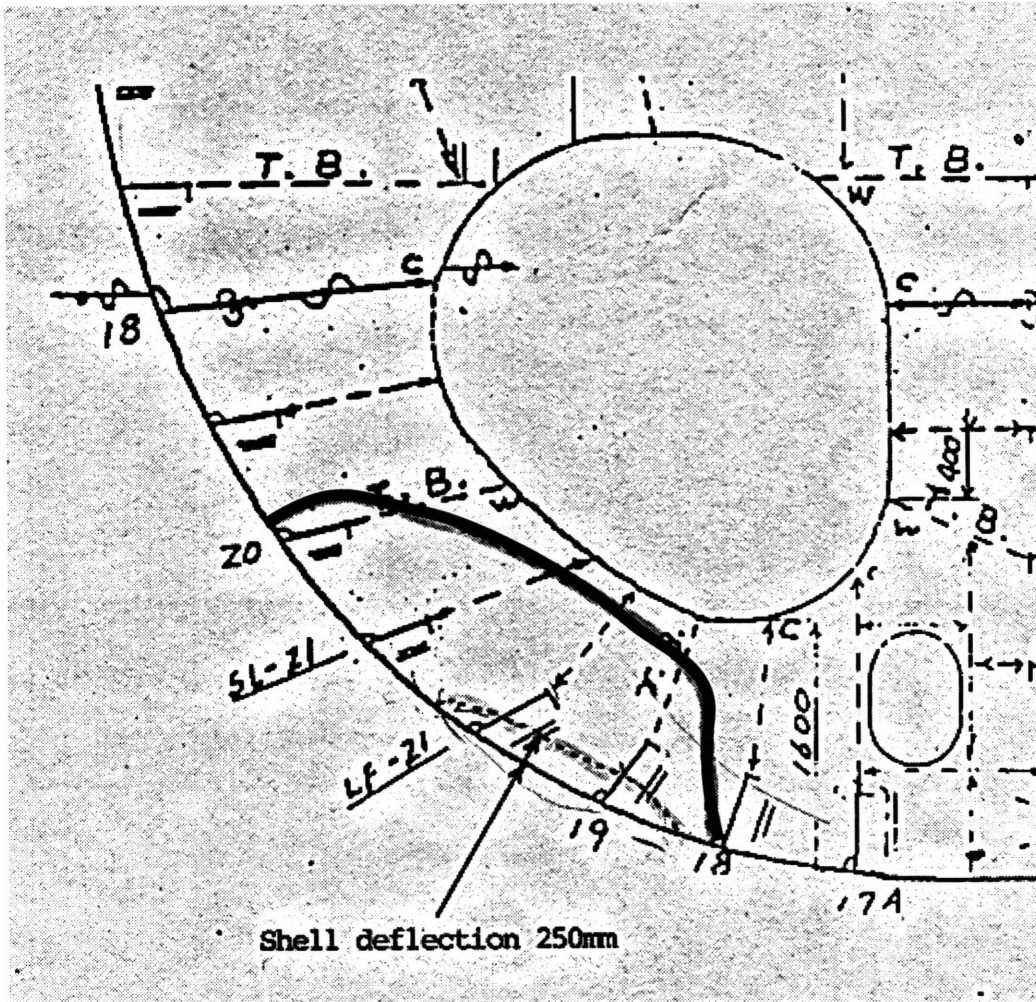
∿∿ Area of Web Frame Buckling

– – – – – Extent of Shell Plate Indentation

Figure 1.2: Extent of Damage

Chapter 2

Circular Flanged Plates - Pre-failure Analysis

In this chapter, the load-deformation characteristics for a flanged semi-circular plate subject to localized in-plane loadings (Fig. 2.1) is derived. The load case considered is a quasi-static indentation by a cylindrical indenter, approximated analytically by a knife-edge loading. The diametral edge of the bulkhead is fully clamped. The circumferential edge is assumed constrained by the flange to only in-plane motions.

The response of the plate consists of two phases; before and after maximum load (here called pre-failure and post-failure phases). In the pre-failure phase, the load is increasing up to the point of maximum strength; rotations are moderately large, but the strains remain small. During this phase (refer to Fig. 2.2), the plate undergoes pre-buckling (OA), buckling (point A), and post-buckling (AB) stages. Near the point of membrane yielding the load is a maximum (point C), and the out-of-plane pattern of deformation becomes constant. This marks the beginning of the post-failure (DE) phase. This process is characterized by rapidly falling loads due to plastic folding, with large strains (up to the rupture strain of the material) and large rotations of plate elements.

Energy methods are used to analyze the elastic pre- and post-buckling response of the plate. Ultimate strength is calculated, using the membrane yield criterion. Limit analysis (Prager, 1959), applied incrementally up to large displacements and rotations is employed in the post-failure range. This leads to a theoretical prediction of the load-deformation characteristics and provides the link between the two phases of the plate response.

In what follows, the pre-failure phase of the plate is analyzed. Each stage of the deformation process is quantified. Critical parameters such as the buckling load "P_{cr}" and the membrane yielding load "P_u" are derived. The membrane yielding load represents the force level at which the membrane yield occurs and is assumed to be the point at which the pre-failure phase ends and the post-failure phase begins. This applies to the materials and geometries in proportions comparable to those of the ship bilge area. A complete analysis of the post-failure phase is undertaken in Chapter 4.

2.1 Displacement Field

In applying energy methods (Timoshenko and Woinowsky-Krieger, 1959), one must first assume suitable displacement fields. The expressions for these fields will contain some arbitrary parameters, the magnitudes of which are found for minimum elastic strain energy or limit load.

Experiments give invaluable information regarding the deformation patterns that take place in the structure. The experimental observations are used in postulating the displacement field and in developing computational models.

2.1.1 Experimental Observations

Fig. 2.3, shows photographs of crushed experimental specimen. As revealed by the photographs, the deformation initially is primarily within a bounded region. As the inden-

tation process progresses, the lateral extent of the bounded region or "deformed zone" remains constant during all tests. Outside of the initial deformed zone, the plate undergoes small but increasing bending along the ridge lines 'OD' and 'OE' as depicted in Fig. 2.4. The lateral extent of the deformed zone is indicated by ζ. It is considered to be an unknown of the process. The curves 'AB', 'BC', 'AC', and 'AOC' represent the bending ridge lines within the deformed zone. Details of the experimental investigation are presented in Chapter 5.

2.1.2 Simplified Two-degree-of-freedom Model

Based on the above experimental observations, a simple two-degree-of-freedom model of the circular flanged plate was developed. Fig. 2.5, shows the assumed model geometry. As indicated, the curved bending ridge lines are approximated by the straight lines 'AB', 'BC', 'AC', 'AO', and 'OC'. Also, piece-wise flat plane surfaces are used to approximate the curved areas 'ABC' and 'AOC'. Moreover, during the pre-failure range, the small amount of bending outside of the deformed zone is neglected. That is, if Γ is the boundary of the deforming zone then:

$$u = v = w \equiv 0 \qquad \text{at } \Gamma$$

where u, v, and w are the displacements in the x, y, and z directions respectively.

The deformation itself, within the constrained zone, consists of in-plane compression and out-of-plane bending. The maximum in-plane displacement is represented by u_0 and the maximum out-of-plane displacement by w_0. Displacement u_0 occurs at the point of application of the compressive load P. When buckling occurs, it is assumed (as shown in Fig. 2.6) that the upper and lower zones within the deformed zone of the model rotate with respect to each other and deform in such a way that the out-of-plane displacement field

18

$w(x, y)$ takes the form of a 'pyramid' with four lines of slope discontinuities. Out-of-plane displacement w_0 occurs at the junction between the upper and lower zones. At this junction, the in-plane displacement is u^*. w_0 and u^* are arbitrary parameters. Their magnitudes as function of u_0 are determined in the next Section.

Note, as shown in Fig. 2.5, the upper zone of the deformed region (where $\eta \le x \le \eta + \lambda$) extends a distance 2ζ laterally and a distance λ transversely while the lower zone (where $0 \le x \le \eta$) extends a same distance 2ζ laterally and a distance η transversely. The distances λ and η are related geometrically to ζ through the radius R of the circular plate as follows:

$$\lambda(\zeta) = R - \sqrt{R^2 - \zeta^2} \tag{2.1}$$

$$\eta(\zeta) = \frac{\zeta\sqrt{R^2 - \zeta^2}}{R + \zeta} \tag{2.2}$$

Consult Appendix A.1 on page 135 for detailed derivation of Eqs. (2.1) and (2.2).

Using all above assumptions, a particular form of the three components of the displacement field $u(x, y)$, $v(x, y)$, and $w(x, y)$ are postulated. u, v, and w are the displacement in x, y, and z directions respectively. As shown in Appendix A.2 on page 136, the displacement field can be expressed by the following equations:

$$u(x, y) = \begin{cases} u^*\left(-\dfrac{x}{\eta} + \dfrac{y}{\zeta}\right) & ; \text{for } 0 \le x \le \eta \\ u_0\left(-\dfrac{x}{\lambda} + \dfrac{\eta}{\lambda}\right) + u^*\left(\dfrac{x}{\lambda} + \dfrac{y}{\zeta} - \dfrac{\eta + \lambda}{\lambda}\right) & ; \text{for } \eta \le x \le \eta + \lambda \end{cases} \tag{2.3}$$

$$v(x, y) = 0 \qquad ; \text{everywhere} \tag{2.4}$$

$$w(x, y) = \begin{cases} w_0\left(\dfrac{x}{\eta} - \dfrac{y}{\zeta}\right) & ; \text{for } 0 \leq x \leq \eta \\[3mm] w_0\left(-\dfrac{x}{\lambda} - \dfrac{y}{\zeta} + \dfrac{\lambda + \eta}{\lambda}\right) & ; \text{for } \eta \leq x \leq \eta + \lambda \end{cases} \qquad (2.5)$$

2.2 Strain Field

From the theory of moderately large displacements of plates, the strain-displacement relations are found to be:

$$\varepsilon_{\alpha\beta} = \frac{1}{2}\left(u_{\alpha,\beta} + u_{\beta,\alpha}\right) + \frac{1}{2}w_{,\alpha}w_{,\beta} \qquad (2.6)$$

Eq. (2.6) is written in indicial notation and reduces explicitly to the following three equations

$$\varepsilon_x = \frac{\partial u}{\partial x} + \frac{1}{2}\left(\frac{\partial w}{\partial x}\right)^2$$

$$\varepsilon_y = \frac{\partial v}{\partial y} + \frac{1}{2}\left(\frac{\partial w}{\partial y}\right)^2$$

$$\varepsilon_{xy} = \frac{1}{2}\left(\frac{\partial u}{\partial y} + \frac{\partial v}{\partial x}\right) + \frac{1}{2}\frac{\partial w}{\partial x}\frac{\partial w}{\partial y}$$

The above equations used in conjunction with the postulated displacement field (Eqs. (2.3), (2.4), and (2.5)) yields a complete description of the strain field.

Appendix A.3 on page 138 shows the detail of the calculations. The three components of the strain field ε_x, ε_y, and ε_{xy} are given by:

$$\varepsilon_x = \begin{cases} -\dfrac{1}{\eta}u^* + \dfrac{1}{2\eta^2}{w_0}^2 & ; \text{for } 0 \le x \le \eta \\[3mm] -\dfrac{1}{\lambda}u_0 + \dfrac{1}{\lambda}u^* + \dfrac{1}{2\lambda^2}{w_0}^2 & ; \text{for } \eta \le x \le \eta + \lambda \end{cases} \qquad (2.7)$$

$$\varepsilon_y = \dfrac{1}{2\zeta^2}{w_0}^2 \qquad ; \text{everywhere} \qquad (2.8)$$

$$\varepsilon_{xy} = \begin{cases} \dfrac{1}{2\zeta}u^* - \dfrac{1}{2\eta\zeta}{w_0}^2 & ; \text{for } 0 \le x \le \eta \\[3mm] \dfrac{1}{2\zeta}u^* + \dfrac{1}{2\lambda\zeta}{w_0}^2 & ; \text{for } \eta \le x \le \eta + \lambda \end{cases} \qquad (2.9)$$

Note that the components of the strain tensor depend only on the known radius of the plate, and unknown in-plane displacements u_0 and u^*, out-of-plane displacement w_0, and parameter of the process ζ. Keep in mind that λ and η are geometrically related to ζ through Eqs. (2.1) and (2.2).

2.3 Primary and Secondary Equilibrium Paths

In what follows, we make use of Wierzbicki and Huang (1991) and Geiger (1989) formulation. They determined the equilibrium path of a crushed box column by using the principal of virtual work.

However, one needs to point out as stated by McClintock and Argon (1966) that for small strains and displacements, there is an upper bond theorem for the elastic stiffness when a complete displacement field is postulated. In the present analysis, as usually done, we neglect through thickness stresses and displacements to end up with a simpler dis-

placement field to use in finding the energies. Strictly speaking this is not an upper bond, but experience has shown that such fields give good approximations.

Considering half of our model (because of symmetry) and defining Π to be the total potential energy, P the total compressive force, and U_m and U_b the membrane and bending energies respectively, we get

$$\Pi\,(u_0,\,w_0)\,=\,U_m\,(u_0,\,w_0)\,+\,U_b\,(u_0,\,w_0)\,-\left(\frac{P}{2}\right)\!u_0 \tag{2.10}$$

The calculation of U_m and U_b are carried out in Appendix A.4 on page 140. The final result is given by the following:

$$U_m\,=\,\frac{Et}{2\,(1-v^2)}\Big[C_1{w_0}^4+C_2u_0{w_0}^2+C_3u^*{w_0}^2+C_4u^*u_0+C_5{u^*}^2+C_6{u_0}^2\Big] \tag{2.11}$$

$$U_b\,=\,\frac{Et^3}{24\,(1-v^2)}C_7{w_0}^2 \tag{2.12}$$

where E and v denote, respectively, the Young's modulus and the Poisson's ratio and t the thickness of the plate. The coefficients C_i ($i\,=\,1,\,...,\,7$) all depend on geometric parameters only, the radius R, and the unknown of the process, ζ. For exact expression of the coefficients, consult Appendix A.4 on page 140.

It should be pointed out that the present model gives a good approximation of the membrane energy, but a less accurate approximation of the bending energy. This is due to the fact that we had to smooth-out the edges of the 'pyramid' in the bending energy calculation because slope discontinuities are not admissible in elastic structures. Details pertinent to the smoothening process are described in Appendix A.4 on page 140.

Making use of Eqs. (2.11) and (2.12), the total potential energy defined by Eq. (2.10) reduces to the following expression

$$\Pi\,(u_0,\,w_0) \;=\; \frac{Et}{2\,(1-v^2)}\Big[C_1 w_0^{\,4} + C_2 u_0 w_0^{\,2} + C_3 u^* w_0^{\,2} + C_4 u^* u_0$$
$$+\; C_5 u^{*2} + C_6 u_0^{\,2} \Big] + \frac{Et^3}{24\,(1-v^2)} C_7 w_0^{\,2} - \frac{1}{2} P u_0$$

The equilibrium condition $\delta\Pi \;=\; \dfrac{\partial\Pi}{\partial u_0}\,\delta u_0 + \dfrac{\partial\Pi}{\partial u^*}\,\delta u^* + \dfrac{\partial\Pi}{\partial w_0}\,\delta w_0 \;=\; 0$ applied to the above expression, gives rise to a system of three nonlinear algebraic equations relating P, u_0 , u^*, and w_0 as follows:

$$\frac{\partial\Pi}{\partial u_0} \;=\; \frac{Et}{2\,(1-v^2)}\Big[C_2 w_0^{\,2} + C_4 u^* + 2 C_6 u_0 \Big] - \frac{1}{2} P \;=\; 0$$

which reduces to

$$P \;=\; \frac{Et}{(1-v^2)}\Big[C_2 w_0^{\,2} + C_4 u^* + 2 C_6 u_0 \Big] \tag{2.13}$$

and

$$\frac{\partial\Pi}{\partial u^*} \;=\; \frac{Et}{2\,(1-v^2)}\Big[C_3 w_0^{\,2} + C_4 u_0 + 2 C_5 u^* \Big] \;=\; 0$$

which reduces to

$$u^* \;=\; -\frac{C_3}{2 C_5} w_0^{\,2} - \frac{C_4}{2 C_5} u_0 \tag{2.14}$$

and

$$\frac{\partial \Pi}{\partial w_0} = \frac{Et}{2(1-v^2)} \left[4C_1 w_0^3 + 2C_2 u_0 w_0 + 2C_3 u^* w_0 \right] + \frac{Et^3}{12(1-v^2)} C_7 w_0 = 0$$

which reduces to

$$w_0 \left[4C_1 w_0^2 + 2C_2 u_0 + 2C_3 u^* + \frac{C_7 t^2}{6} \right] = 0 \qquad (2.15)$$

Now, using the optimal value of the in-plane displacement u^* given by Eq. (2.14) in Eqs. (2.13) and (2.15), the following system of two non-linear equations in u_0 and w_0 is found:

$$P = \frac{Et}{1-v^2} \left[\left(2C_6 - \frac{C_4^2}{2C_5} \right) u_0 + \left(C_2 - \frac{C_3 C_4}{2C_5} \right) w_0^2 \right] \qquad (2.16)$$

and

$$w_0 \left[\left(4C_1 - \frac{C_3^2}{C_5} \right) w_0^2 + \left(2C_2 - \frac{C_3 C_4}{C_5} \right) u_0 + \frac{C_7 t^2}{6} \right] = 0 \qquad (2.17)$$

From Eq. (2.17), one can identify two distinct solutions for the out-of-plane displacement w_0 as function of the in-plane displacement u_0.

The first solution,

$$w_0 = 0$$

for all u_0, defines the in-plane elastic or primary equilibrium path.

The second one,

24

$$\left(4C_1 - \frac{C_3^2}{C_5}\right)w_0^2 + \left(2C_2 - \frac{C_3 C_4}{C_5}\right)u_0 + \frac{C_7 t^2}{6} = 0$$

or

$$w_0^2 = -\frac{\left(2C_2 - \dfrac{C_3 C_4}{C_5}\right)}{\left(4C_1 - \dfrac{C_3^2}{C_5}\right)}u_0 - \frac{\dfrac{C_7 t^2}{6}}{\left(4C_1 - \dfrac{C_3^2}{C_5}\right)} \tag{2.18}$$

defines the buckled elastic or secondary equilibrium path.

Now, one can write the final expression for the primary equilibrium path by inserting the value of $w_0 = 0$ into Eq. (2.16) and letting P_I stand for the primary equilibrium path load. And the final expression for the secondary equilibrium path by inserting Eq. (2.18) in (2.16) and letting P_{II} denote the secondary equilibrium path load. The final result is given by the following two equations;

$$P_I = \frac{Et}{1-v^2}\left(2C_6 - \frac{C_4^2}{2C_5}\right)u_0 \tag{2.19}$$

$$P_{II} = \frac{Et}{1-v^2}\left\{\left[2C_6 - \frac{C_4^2}{2C_5} - 2\frac{\left(C_2 - \dfrac{C_3 C_4}{2C_5}\right)^2}{\left(4C_1 - \dfrac{C_3^2}{C_5}\right)}\right]u_0 - \frac{t^2}{6}\frac{C_7\left(C_2 - \dfrac{C_3 C_4}{2C_5}\right)}{\left(4C_1 - \dfrac{C_3^2}{C_5}\right)}\right\} \tag{2.20}$$

where the coefficients C_i ; $(i = 1, ..., 7)$ are as follows:

$$C_1(\zeta) = \frac{1}{8}\frac{\zeta}{\eta^3} + \frac{1}{8}\frac{\eta}{\zeta^3} + \frac{1}{4}\frac{1}{\eta\zeta} + \frac{1}{8}\frac{\zeta}{\lambda^3} + \frac{1}{8}\frac{\lambda}{\zeta^3} + \frac{1}{4}\frac{1}{\lambda\zeta}$$

$$C_2(\zeta) = -\frac{1}{2}\frac{\zeta}{\lambda^2} - \frac{1}{2}\frac{v}{\zeta}$$

$$C_3(\zeta) = -\frac{1}{2}\frac{\zeta}{\eta^2} - \frac{1}{2}\frac{\zeta}{\lambda^2}$$

$$C_4(\zeta) = -\frac{\zeta}{\lambda}$$

$$C_5(\zeta) = \frac{1}{2}\frac{\zeta}{\eta} + \frac{1}{4}\frac{\eta}{\zeta} - \frac{1}{4}\frac{v\eta}{\zeta} + \frac{1}{2}\frac{\zeta}{\lambda} + \frac{1}{4}\frac{\lambda}{\zeta} - \frac{1}{4}\frac{v\lambda}{\zeta}$$

$$C_6(\zeta) = \frac{1}{2}\frac{\zeta}{\lambda}$$

$$C_7(\zeta) = \frac{\zeta}{\eta^3} + \frac{\eta}{\zeta^3} + \frac{2}{\zeta\eta} + \frac{\zeta}{\lambda^3} + \frac{\lambda}{\zeta^3} + \frac{2}{\lambda\zeta}$$

Using energy methods, we have succeeded with a simple two-degree-of-freedom model to identify, as the parameter ζ changes, a family of primary and secondary equilibrium curves given by Eqs. (2.19) and (2.20).

Now, we will make use of dimensionless parameters to get a generalized description of the process. Working from the dimensionless equations, pre-buckling, buckling, and post-buckling stages of the pre-failure phase will be quantified by tracking how the parameter ζ changes.

An appropriate dimensionless parameter for the unknown of the process ζ is

$$\bar{\zeta} = \frac{\zeta}{R} \tag{2.21}$$

where R is the radius of the circular plate.

Two more dimensionless parameters shall be defined as

$$\bar{P} = \frac{PR}{D} \tag{2.22}$$

and

$$\bar{u} = \frac{uR}{t^2} \tag{2.23}$$

where t is the thickness of the plate and D is the flexural rigidity of the plate defined by the following expression:

$$D = \frac{Et^3}{12(1 - v^2)}$$

With the above definitions, a dimensionless form of Eq. (2.19) is given by:

$$\bar{P}_I = 12 \left(2\bar{C}_6 - \frac{\bar{C}_4^2}{2\bar{C}_5} \right) \bar{u}_0 \tag{2.24}$$

and a dimensionless form of Eq. (2.20) by:

$$\bar{P}_{II} = 12 \left[2\bar{C}_6 - \frac{\bar{C}_4^2}{2\bar{C}_5} - 2\frac{\left(\bar{C}_2 - \frac{\bar{C}_3\bar{C}_4}{2\bar{C}_5} \right)^2}{\left(4\bar{C}_1 - \frac{\bar{C}_3^2}{\bar{C}_5} \right)} \right] \bar{u}_0 - \frac{2\bar{C}_7 \left(\bar{C}_2 - \frac{\bar{C}_3\bar{C}_4}{2\bar{C}_5} \right)}{\left(4\bar{C}_1 - \frac{\bar{C}_3^2}{\bar{C}_5} \right)} \tag{2.25}$$

The step by step derivation is shown in Appendix A.5 on page 145 along with the expressions for the parameters $\bar{C}_i$; $(i = 1, ..., 7)$.

27

2.4 Pre-buckling Stage

Fig. 2.7, shows a family of load-deflection curves in the pre-buckling stage for several values of $\bar{\zeta}$. Clearly, there exists a value of $\bar{\zeta}$ for which the stiffness of the plate is minimum. It is this value of $\bar{\zeta}$ that will govern the pre-buckling stage (plate remains in-plane) of the deformation process. The structure, therefore, follows the primary equilibrium path corresponding to the minimum stiffness. To determine which path it is and the corresponding value of $\bar{\zeta}$, the dimensionless stiffness of the plate as function of the parameter $\bar{\zeta}$ is plotted in Fig. 2.8. The lowest stiffness occurs when $\bar{\zeta} = 1$. Hence, the deformed zone extents to the entire plate during the in-plane elastic phase (pre-buckling).

A limit analysis as $\bar{\zeta}$ approaches the value 1, gives the following:

$$\lim_{\bar{\zeta} \to 1} \bar{\lambda} = 1 \; ; \qquad \lim_{\bar{\zeta} \to 1} \bar{\eta} = 0 \; ; \qquad \lim_{\bar{\zeta} \to 1} \overline{C_6} = \frac{1}{2} \; ;$$

$$\lim_{\bar{\zeta} \to 1} \overline{C_4} = -1 \; ; \qquad \lim_{\bar{\zeta} \to 1} \overline{C_5} = +\infty \; ;$$

and

$$\text{Stiffeness of Primary Path} = \lim_{\bar{\zeta} \to 1} 12 \left(2\overline{C_6} - \frac{\overline{C_4}^2}{2\overline{C_5}} \right) = 12 \; ;$$

Finally the primary equilibrium path is described by:

$$\overline{P_I} = 12\overline{u_0} \tag{2.26}$$

and

$$\bar{\zeta} = 1 \tag{2.27}$$

28

2.5 Buckling Point

Fig. 2.9, shows the pre-buckling load-deformation curve given by Eq. (2.26) and a family of post-buckling curves for several values of $\bar{\zeta}$ given by Eq. (2.25). The locus of the bifurcation loads as $\bar{\zeta}$ varies from 0 to 1 is plotted in Fig. 2.10. The lowest bifurcation load (called here $\overline{P_{cr}}$) is obtained at $\bar{\zeta} = 0.75$, and is assumed to characterize the onset of buckling. It represents the end of the in-plane phase (primary equilibrium path) and the beginning of the buckled phase (secondary equilibrium path).

As seen in Fig. 2.10, the buckling load $\overline{P}_{cr}$ is:

$$\overline{P_{cr}} = 24 \tag{2.28}$$

and the corresponding critical in-plane displacement $\left(\overline{u_0} \right)_{cr}$ is:

$$\left(\overline{u_0} \right)_{cr} = 2 \tag{2.29}$$

The above results are found by first equating Eqs. (2.25) and (2.26) and solving for $\left(\overline{u_0} \right)_{cr}$ as function of $\bar{\zeta}$. Then, second by using this result in Eq. (2.26) and minimizing with respect to $\bar{\zeta}$.

As depicted in Fig. 2.11, the onset of buckling leads to an immediate drop in axial stiffness to about 0.6 of the pre-buckling stiffness. In order to check the validity of our approximate solution, we compared our result with the exact values of 0.5 and 0.408 for rectangular plates loaded in compression by a distributed force with edges kept straight and edges free to wave, respectively (Rhodes, 1989). As seen, our approximate value compares favorably well with the exact ones given the different nature of the problem at hand.

2.6 Post-buckling Stage

Referring to Fig. 2.9, and focussing on the secondary equilibrium path given by:

$$\overline{P}_{II} = 12\left[2\overline{C}_6 - \frac{\overline{C}_4^2}{2\overline{C}_5} - 2\frac{\left(\overline{C}_2 - \frac{\overline{C}_3\overline{C}_4}{2\overline{C}_5}\right)^2}{\left(4\overline{C}_1 - \frac{\overline{C}_3^2}{\overline{C}_5}\right)}\right]\overline{u}_0 - \frac{2\overline{C}_7\left(\overline{C}_2 - \frac{\overline{C}_3\overline{C}_4}{2\overline{C}_5}\right)}{\left(4\overline{C}_1 - \frac{\overline{C}_3^2}{\overline{C}_5}\right)}$$

we see, as the axial shortening increases, a further reduction in the plate stiffness. The load-deflection curve follows the envelope of a family of straight lines with various values of $\overline{\zeta} = \zeta/R$. Fig. 2.12, shows the final result for both the primary equilibrium and secondary equilibrium paths.

The present model predicts that the assumed 'pyramid' shape for $w\,(x,y)$ in the post-buckling stage reduces gradually in size. As the loading progresses, $\overline{\zeta}$ decreases continuously from $(\overline{\zeta})_{cr} = 0.75$ (onset of buckling) to $(\overline{\zeta})_u$ corresponding to the membrane yield of the material. Soon after the membrane yield is reached, the plate would have exhausted most of its load carrying capacity. We identify the force corresponding to the membrane yield as the ultimate strength of the plate $\overline{P}_u$, and is assumed to characterize the end of the secondary equilibrium path.

2.7 Membrane Yield

As stated above, with increasing axial indentation, the plate material will yield. In this section, we identify the most stressed part of the material and calculate the corresponding value of $(\overline{\zeta})_u$.

Assuming that the plate yields due to membrane stresses alone, the plane stress yield condition applies (Ugural, 1981):

$$\sigma_x^2 - \sigma_x\sigma_y + \sigma_y^2 + 3\sigma_{xy}^2 = \sigma_0^2 \tag{2.30}$$

where σ_0 is the yield strength of the material.

At the commencement of yielding, Eq. (2.30) can be expressed in terms of the components of the strain tensor by making use of Hook's law for plane stress (Crandall and Dahl, 1959):

$$\left\{ \begin{aligned} \sigma_x &= \frac{E}{1-v^2}(\varepsilon_x + v\varepsilon_y) \\ \sigma_y &= \frac{E}{1-v^2}(\varepsilon_y + v\varepsilon_x) \\ \sigma_{xy} &= \frac{E}{1+v}\varepsilon_{xy} \end{aligned} \right. \tag{2.31}$$

The corresponding equation by inserting (2.31) in (2.30) takes the following form:

$$\frac{E^2}{(1-v^2)^2}(\varepsilon_x + v\varepsilon_y)^2 - \frac{E^2}{(1-v^2)^2}(\varepsilon_x + v\varepsilon_y)(\varepsilon_y + v\varepsilon_x)$$
$$+ \frac{E^2}{(1-v^2)^2}(\varepsilon_y + v\varepsilon_x)^2 + 3\frac{E^2}{(1+v)^2}\varepsilon_{xy}^2 = \sigma_0^2$$

That is:

$$a_1\left(\varepsilon_x^2 + \varepsilon_y^2\right) - a_2\varepsilon_x\varepsilon_y + a_3\varepsilon_{xy}^2 = \left(\frac{\sigma_0}{E}\right)^2 \tag{2.32}$$

where

$$a_1 = \frac{v^2 - v + 1}{(1 - v^2)^2}$$

$$a_2 = \frac{v^2 - 4v + 1}{(1 - v^2)^2}$$

$$a_3 = \frac{3}{(1 + v)^2}$$

Using the expressions of u^* and w_0 as function of u_0 (Eqs. (2.14) and (2.18)) in Eqs. (2.7), (2.8), and (2.9), one can conveniently express the axial and shear strains as follows:

$$\varepsilon_x = \begin{cases} D_1 u_0 + D_2 & ; \text{for } 0 \le x \le \eta \\ (D_1{}^*) u_0 + D_2{}^* & ; \text{for } \eta \le x \le \eta + \lambda \end{cases} \tag{2.33}$$

$$\varepsilon_y = D_3 u_0 + D_4 = (D_3{}^*) u_0 + D_4{}^* \qquad ; \text{everywhere} \tag{2.34}$$

$$\varepsilon_{xy} = \begin{cases} D_5 u_0 + D_6 & ; \text{for } 0 \le x \le \eta \\ (D_5{}^*) u_0 + D_6{}^* & ; \text{for } \eta \le x \le \eta + \lambda \end{cases} \tag{2.35}$$

where the parameters $D_i(\zeta)$; ($i = 1, ..., 6$) and $D_i{}^*(\zeta)$; ($i = 1, ..., 6$) are given in Appendix A.6 on page 147.

Now, Eqs. (2.33), (2.34), and (2.35) in Eq. (2.32) for the case where $0 \le x \le \eta$ leads the following quadratic equation in u_0:

$$A u_0{}^2 + B u_0 + \left[C - \left(\frac{\sigma_0}{E} \right)^2 \right] = 0 \tag{2.36}$$

where

32

$$A = a_1\left(D_1^2 + D_3^2\right) - a_2 D_1 D_3 + a_3 D_5^2$$

$$B = 2a_1\left(D_1 D_2 + D_3 D_4\right) - a_2\left(D_1 D_4 + D_2 D_3\right) + 2a_3 D_5 D_6$$

$$C = a_1\left(D_2^2 + D_4^2\right) - a_2 D_2 D_4 + a_3 D_6^2$$

This result is also valid for the case where $\eta \leq x \leq \eta + \lambda$. One need only to replace the parameters $D_i(\zeta)$; ($i = 1, ..., 6$) by their counterpart $D_i^*(\zeta)$; ($i = 1, ..., 6$).

A dimensionless form of Eq. (2.36) is given in Appendix A.6 on page 147. The final result is function of the slenderness ratio parameter β defined by $\beta = \dfrac{t}{R}\sqrt{\dfrac{E}{\sigma_0}}$ and takes the following form:

$$\bar{A}\bar{u}_0^2 + \bar{B}\bar{u}_0 + \left(\bar{C} - \frac{1}{\beta^4}\right) = 0 \tag{2.37}$$

The two roots $\left(\bar{u}_0\right)_{u,1}$ and $\left(\bar{u}_0\right)_{u,2}$ of Eq. (2.37) define the yield locus. The corresponding loads plotted as function of $\bar{\zeta}$, delimit a yield surface (Fig. 2.13). Inside this surface, membrane yielding does not occur. Hence, the intersection of the secondary equilibrium path (shown in dotted lines) with the boundary of the yield locus is the point at which membrane yielding occurs. Fig. 2.14, shows the final result for the case where $\eta \leq x \leq \eta + \lambda$.

These two results are for a slenderness parameter $\beta = 0.2315$. This value corresponds to the one of the specimens used in the experimental investigation. In this example, clearly, the upper zone of the model where $\eta \leq x \leq \eta + \lambda$ will yield first. The corresponding non-dimensional ultimate force $\bar{P}_u$ and extent of the deformed zone $\bar{\zeta}$ are:

33

$$\overline{P_u} = 72$$

$$\overline{\zeta_u} = 0.71$$
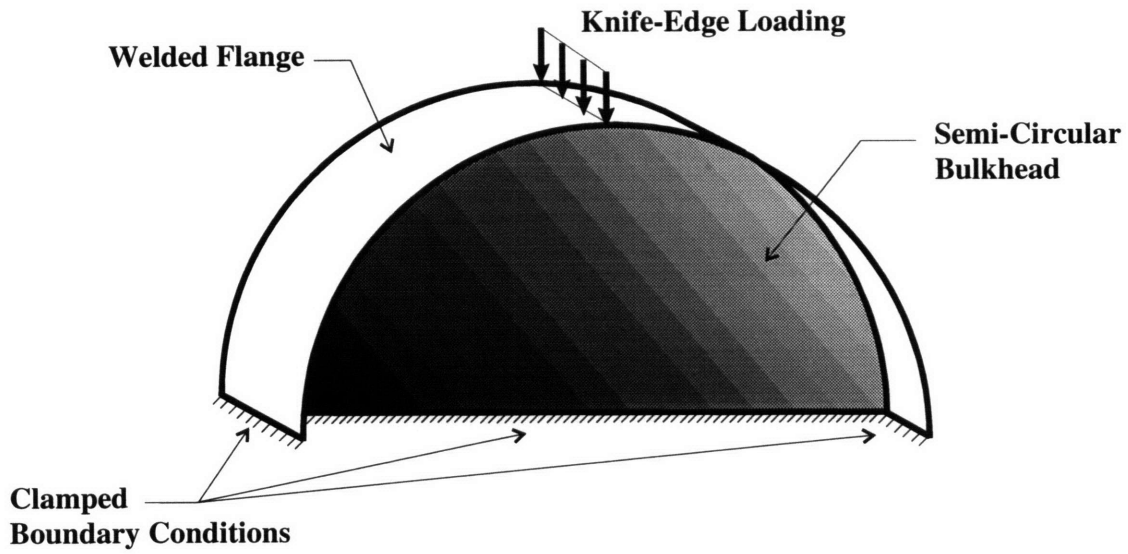
Figure 2.1: Flanged Semi-Circular Plate Unit
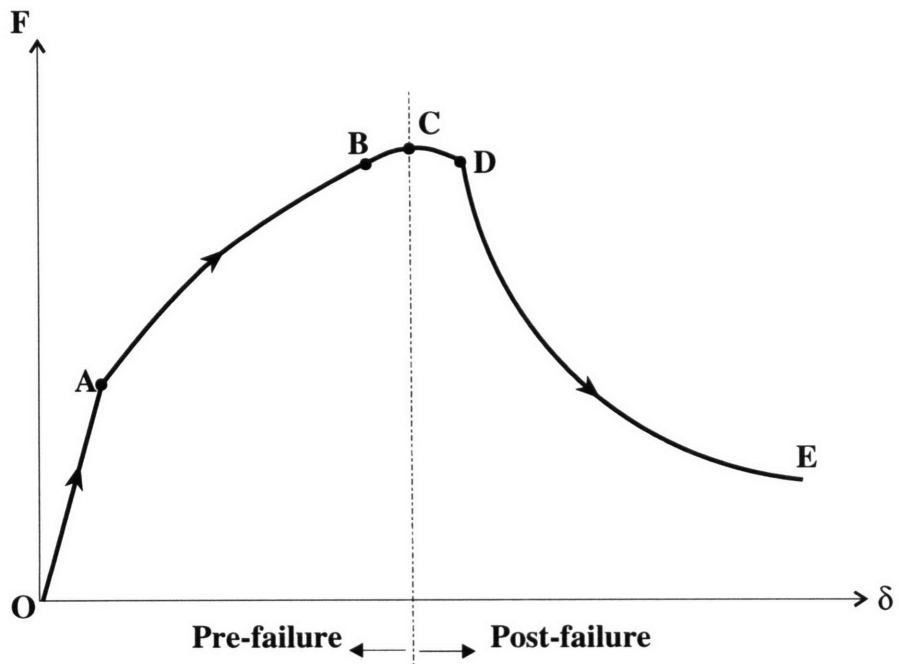
Figure 2.2: Load-Deformation Characteristic
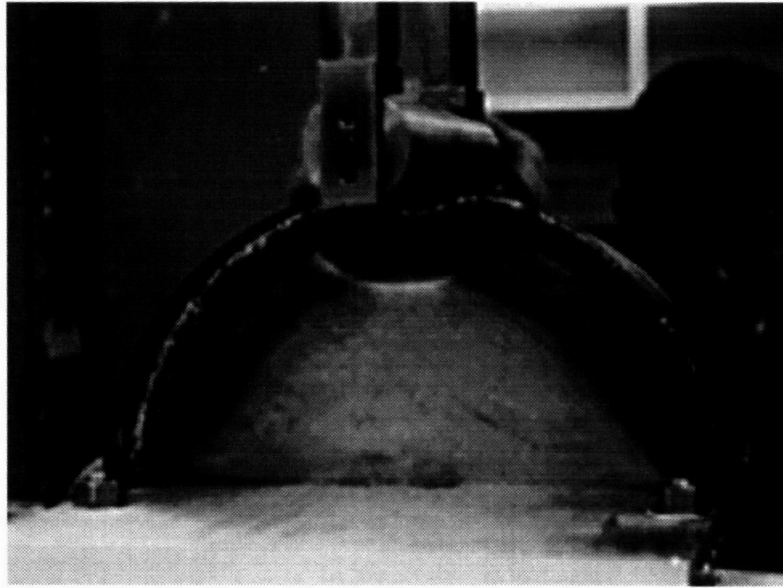
(a) Global View
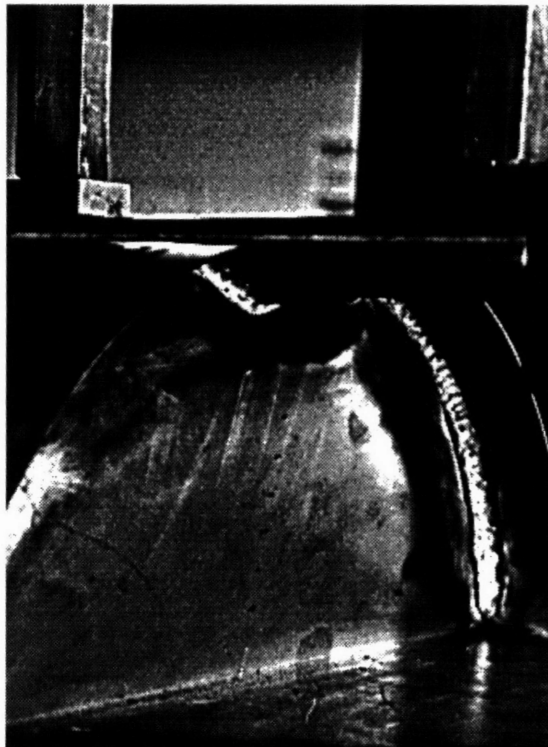
(b) Close-up

Figure 2.3: Crushed Experimental Specimen
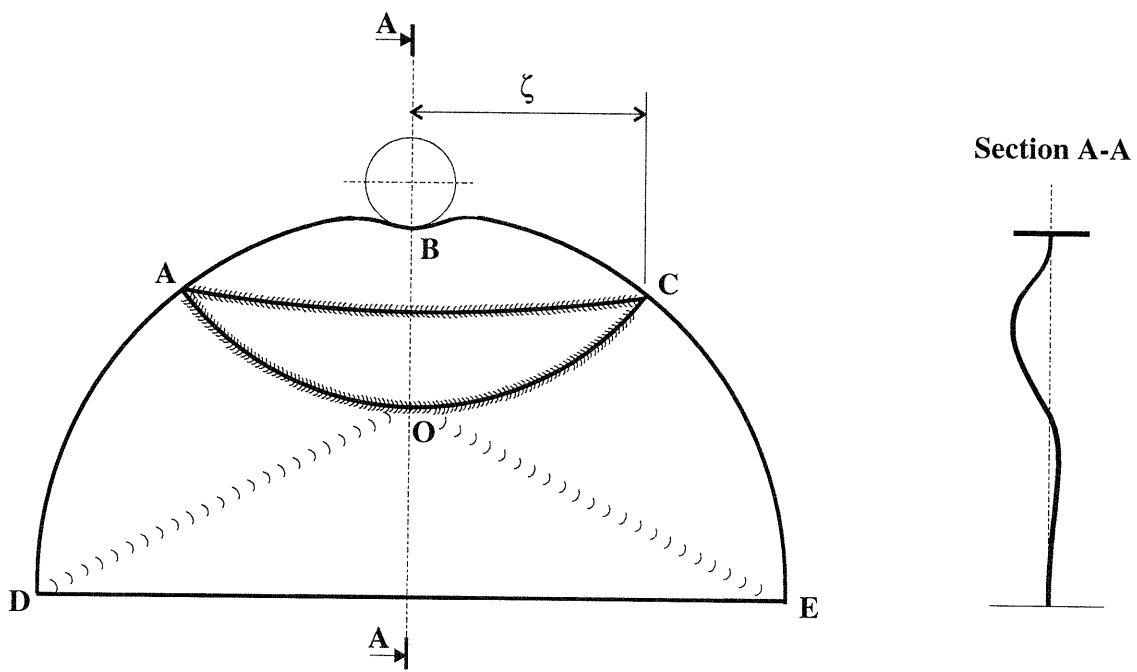
Figure 2.4: Deformed Specimen

(a) Before Membrane Deformation

(b) After Deformation

Figure 2.5: Two-degree-of-freedom Model

Figure 2.6: Displacement Field
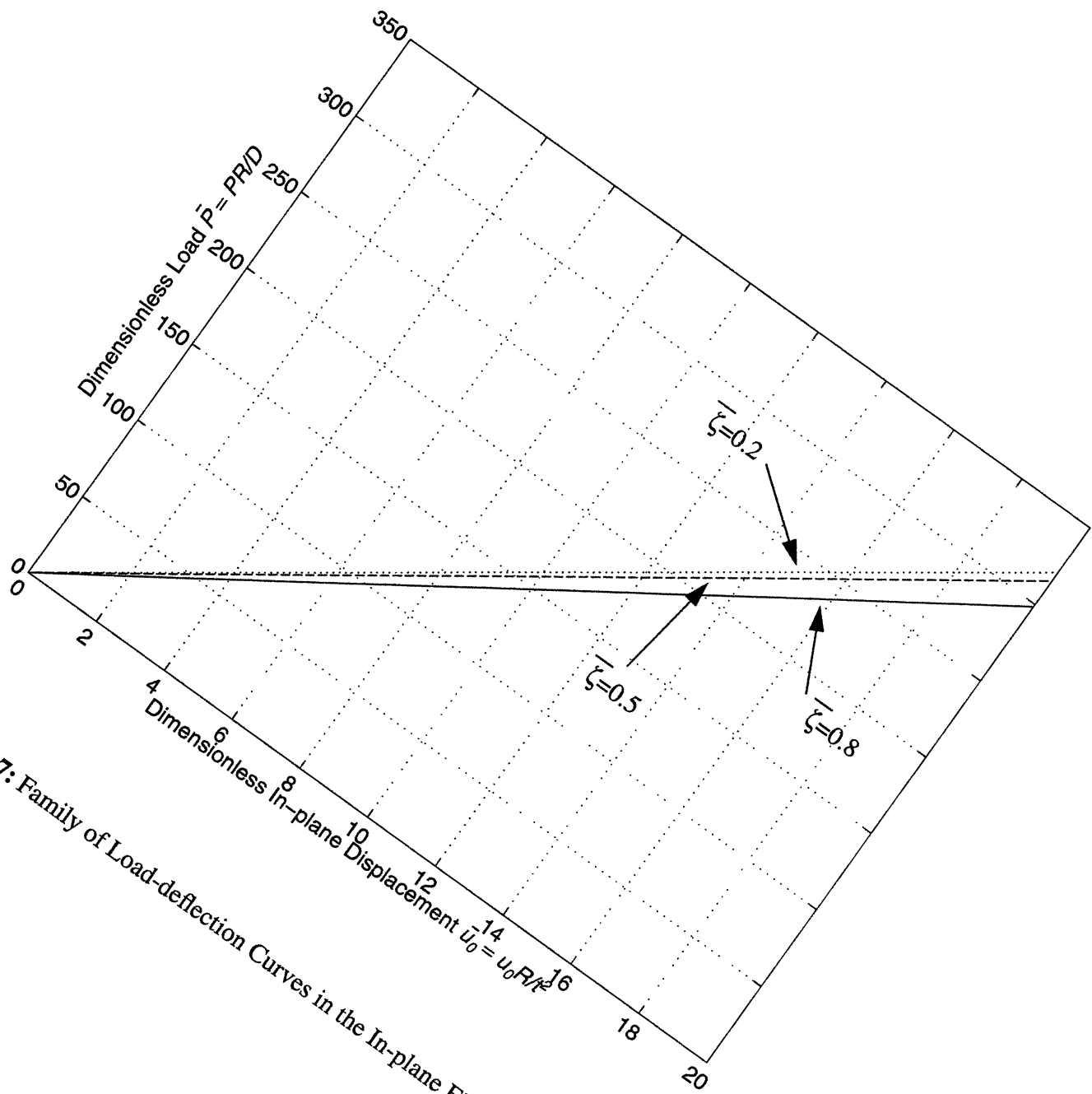
Figure 2.7: Family of Load-deflection Curves in the In-plane Elastic Range

Dimensionless Load $\bar{P} = PR/D$

Dimensionless In-plane Displacement $\bar{u}_0 = u_0 R/t^2$

$\bar{\zeta}=0.2$

$\bar{\zeta}=0.5$

$\bar{\zeta}=0.8$

40
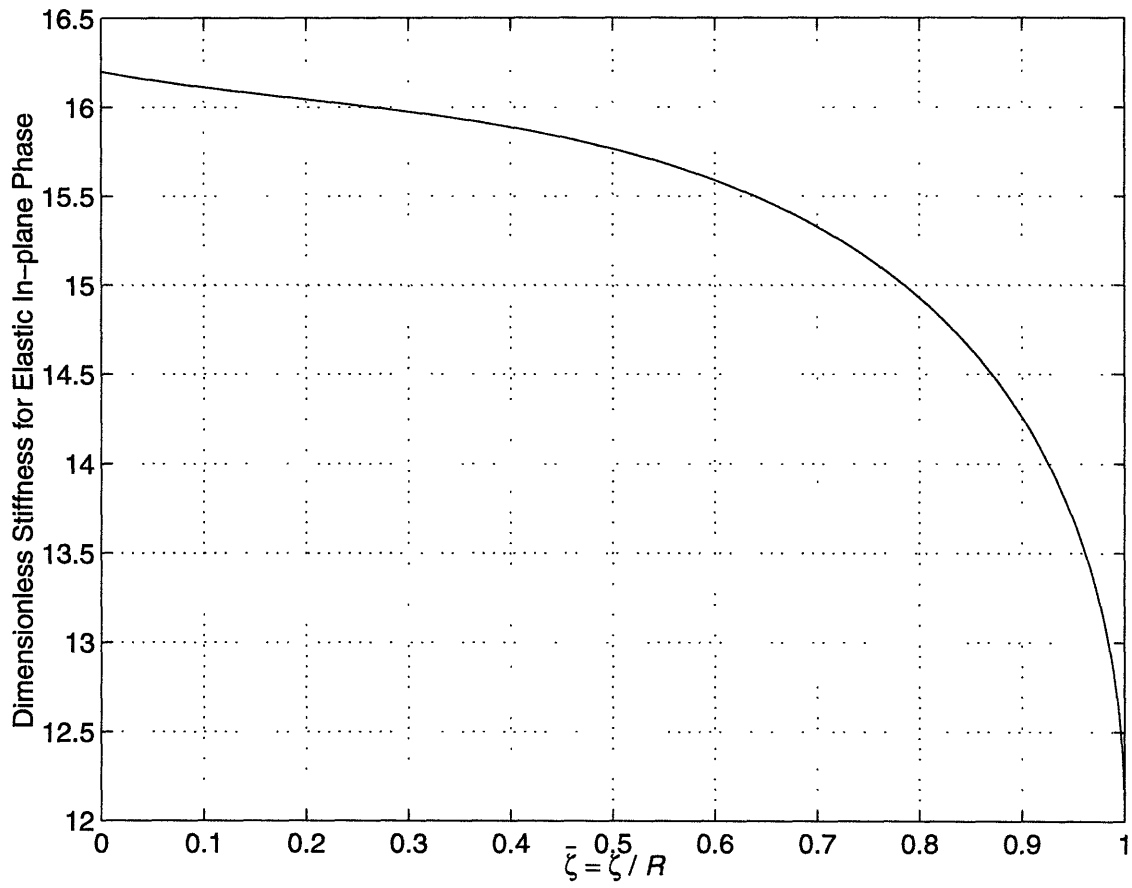
Figure 2.8: Dimensionless Elastic In-plane Stiffness vs. Extent of Damage
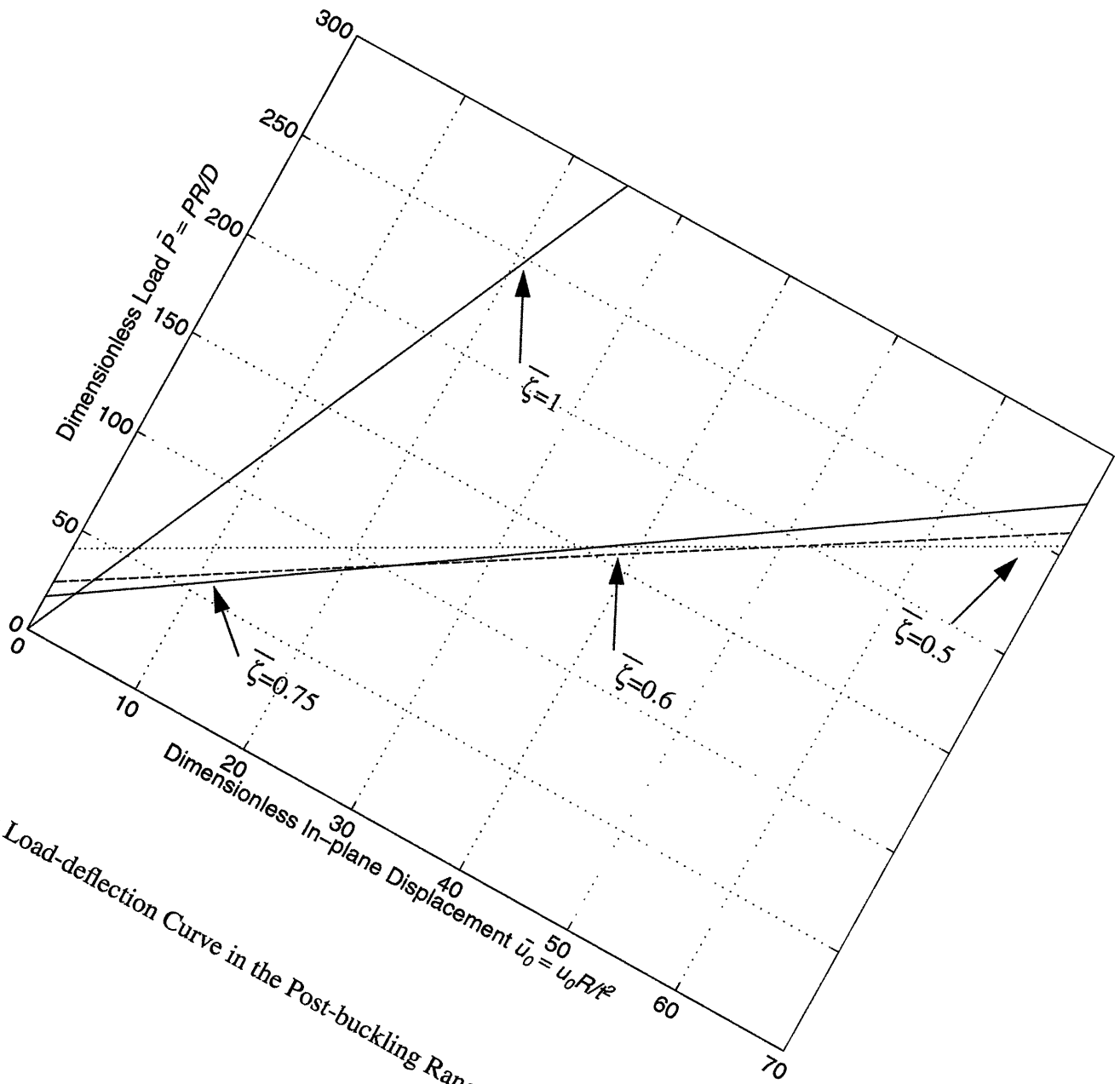
Figure 2.9: Load-deflection Curve in the Post-buckling Range and Mode Transition

Dimensionless Load $\bar{P} = PR/D$

Dimensionless In-plane Displacement $\bar{u}_0 = u_0 R/t^2$

$\bar{\zeta} = 1$

$\bar{\zeta} = 0.75$

$\bar{\zeta} = 0.6$

$\bar{\zeta} = 0.5$

42
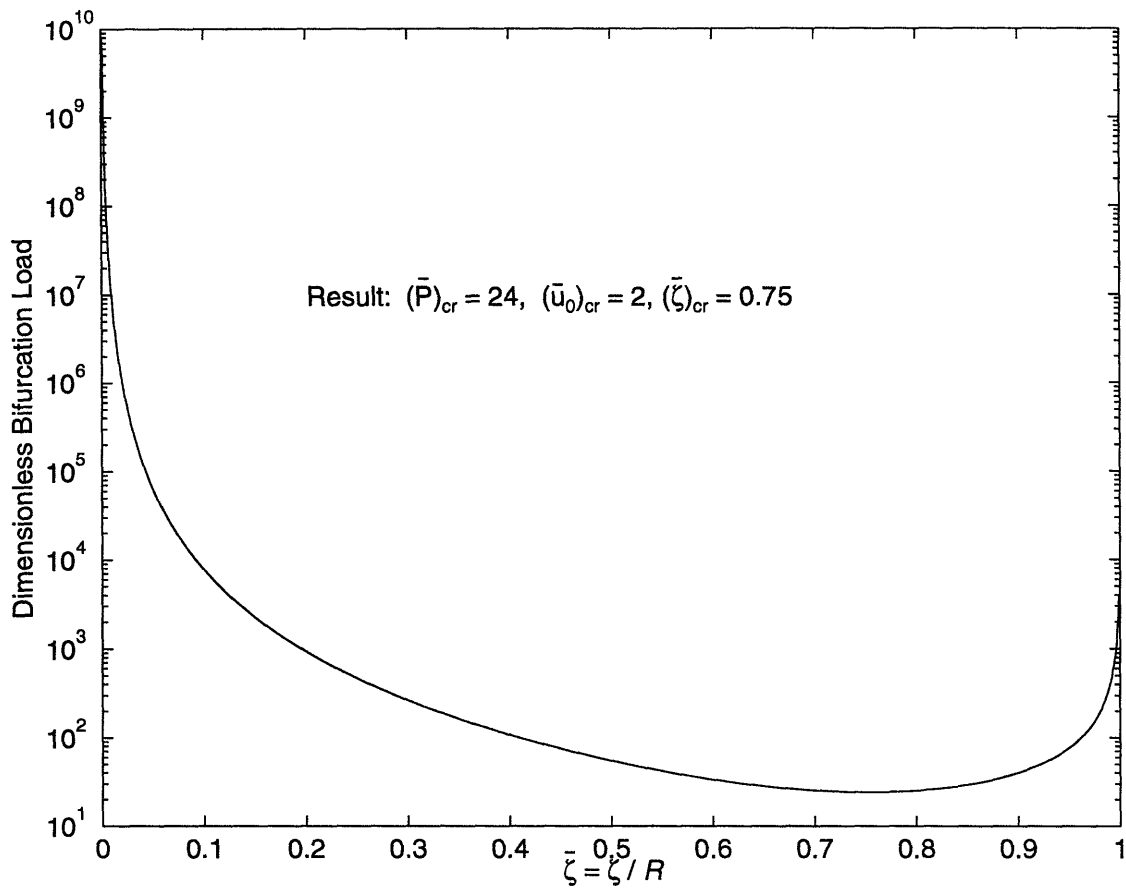
Figure 2.10: Determination of the Buckling Load
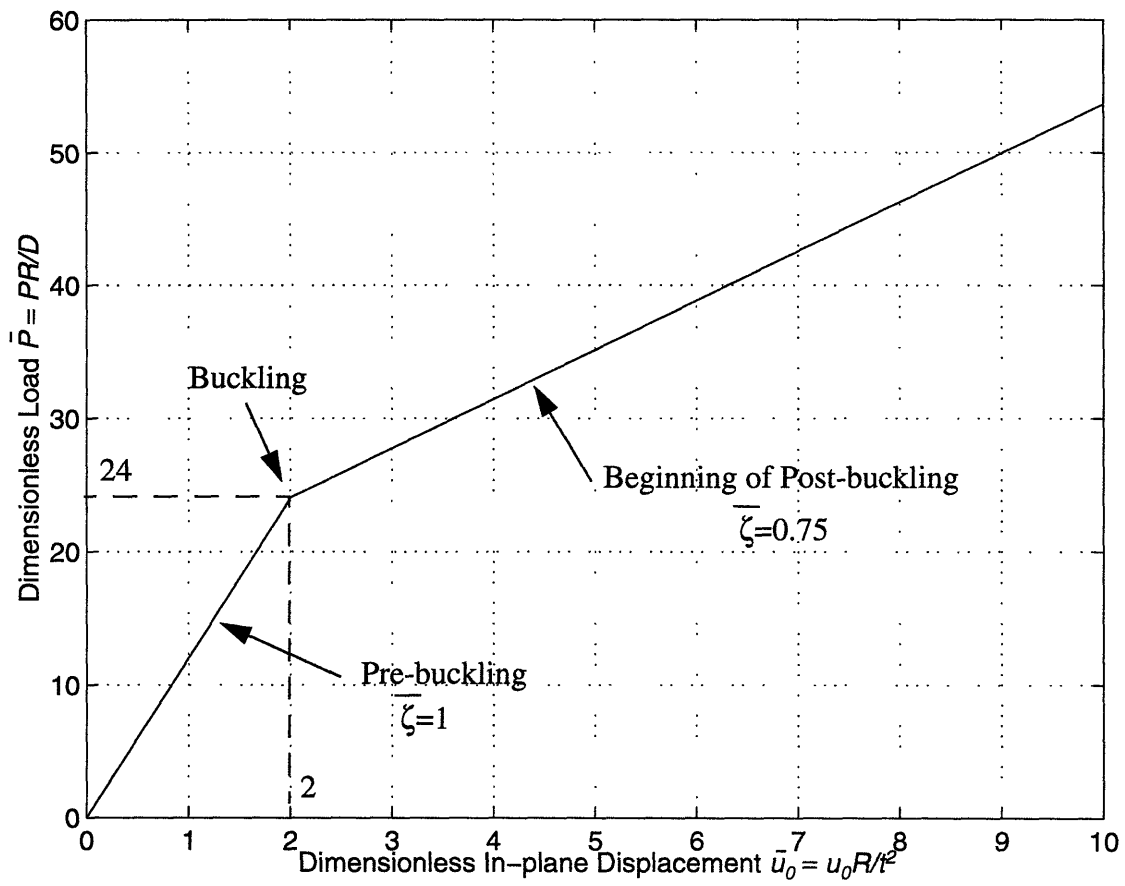
Figure 2.11: Beginning of Post-buckling Phase
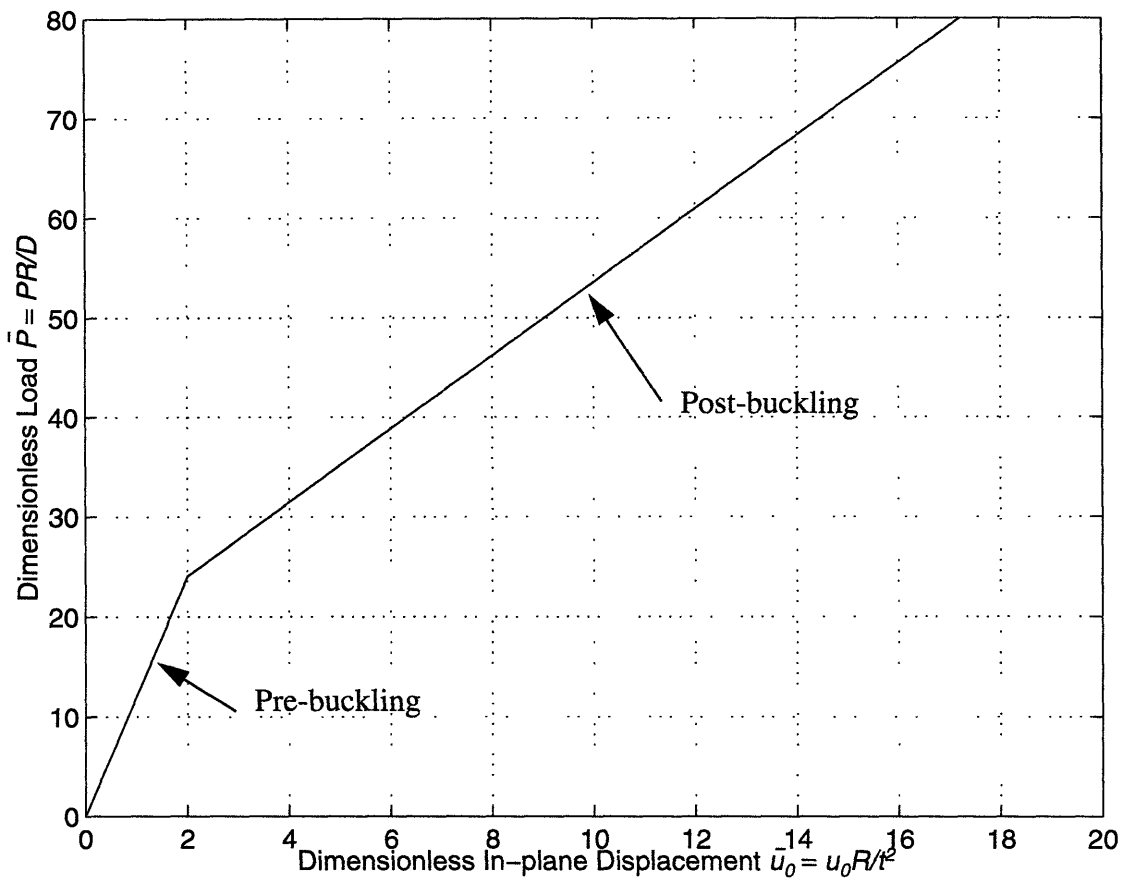
Figure 2.12: Dimensionless Load-deflection Curve for Flanged Semi-circular Plates
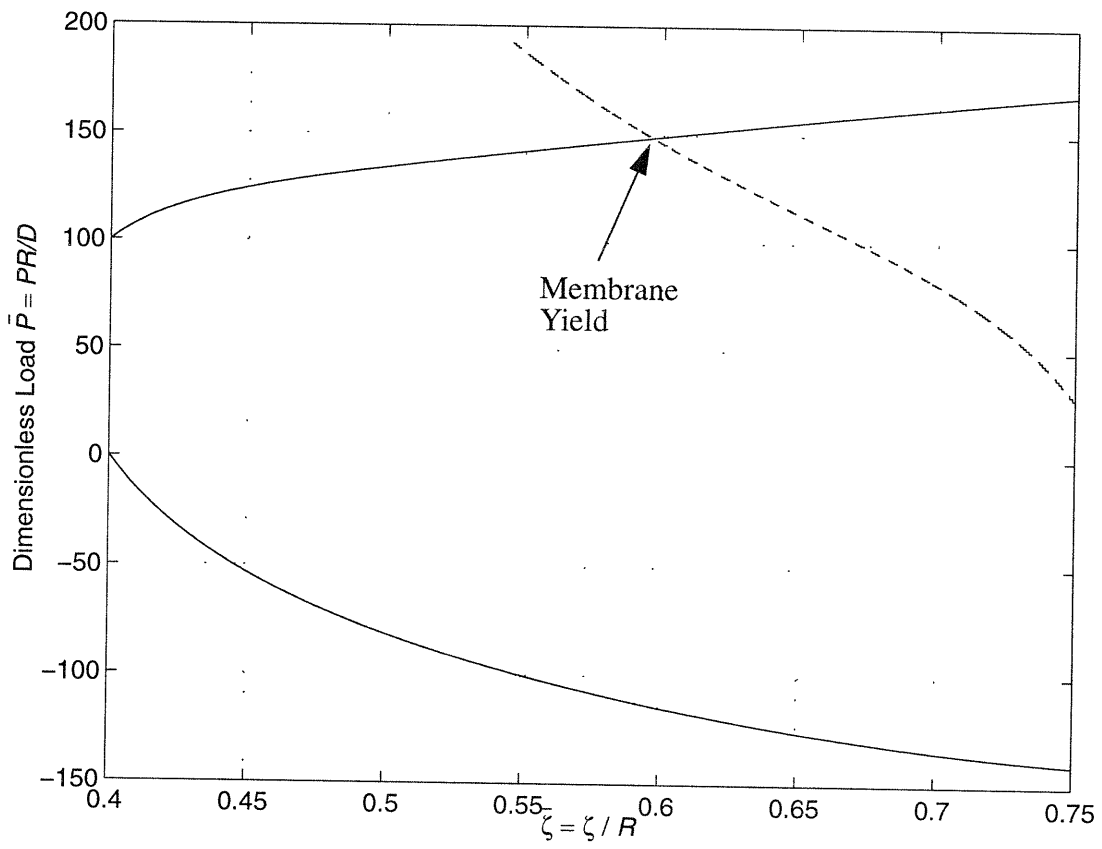
Figure 2.13: Yield Locus for Lower Region of Model
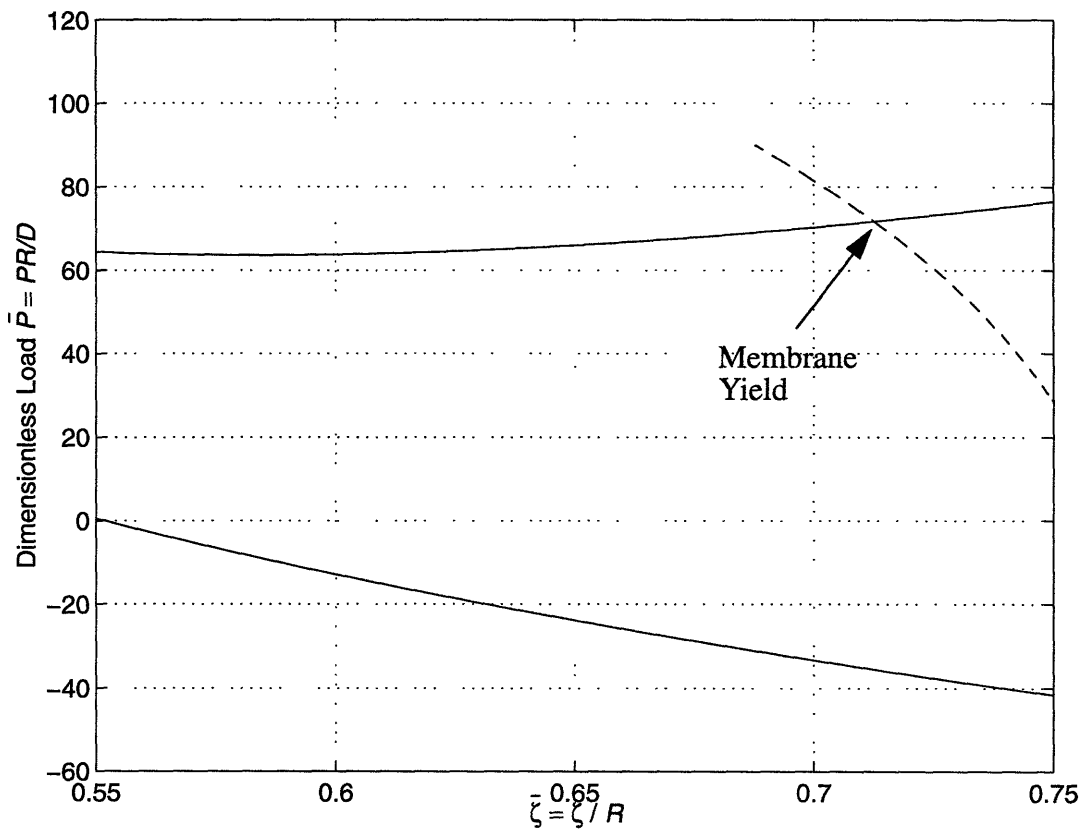
Figure 2.14: Yield Locus for Upper Region of Model

Chapter 3

Circular Flanged Plates - Effect of Initial Imperfections

In the preceding chapter, the plate has been considered to be perfectly flat before load application. Due to structural imperfections and welding distortions, the plate at hand is initially imperfect. In the present chapter, we will investigate the influence of these initial imperfections on the behavior of the structure.

The analysis is carried out following the same logic as in Chapter 2. First, the displacement and strain fields are revisited to include the effect of the initial imperfections. Subsequently, membrane and bending energies are derived from the strain field. Finally, making use of energy methods, the load-deflection curve is determined as function of imperfection magnitudes.

3.1 Displacement and Strain Fields

In addition to the displacement fields $u(x, y)$, $v(x, y)$, and $w(x, y)$ established in Section 2.1 on page 17, we have an additional function $\tilde{w}(x, y)$ representing the initial deviation from the perfectly flat shape. For simplicity, $\tilde{w}(x, y)$ is assumed to be of the same form of the displacement mode $w(x, y)$ with a maximum deflection $\tilde{w}_0$ (Fig. 3.1).

Also, imperfections are introduced only in the transverse direction. There are no imperfections in the in-plane direction.

The new term describing the initial imperfection is given by

$$\tilde{w}(x, y) = \begin{cases} \tilde{w}_0\left(\dfrac{x}{\eta} - \dfrac{y}{\zeta}\right) & ; \text{for } 0 \le x \le \eta \\[3mm] \tilde{w}_0\left(-\dfrac{x}{\lambda} - \dfrac{y}{\zeta} + \dfrac{\lambda + \eta}{\lambda}\right) & ; \text{for } \eta \le x \le \eta + \lambda \end{cases}$$

The entire displacement field is therefore described by the following four functions:

$$u(x, y) = \begin{cases} u^*\left(-\dfrac{x}{\eta} + \dfrac{y}{\zeta}\right) & ; \text{for } 0 \le x \le \eta \\[3mm] u_0\left(-\dfrac{x}{\lambda} + \dfrac{\eta}{\lambda}\right) + u^*\left(\dfrac{x}{\lambda} + \dfrac{y}{\zeta} - \dfrac{\eta + \lambda}{\lambda}\right) & ; \text{for } \eta \le x \le \eta + \lambda \end{cases}$$

$$v(x, y) = 0 \qquad ; \text{everywhere}$$

$$w(x, y) = \begin{cases} w_0\left(\dfrac{x}{\eta} - \dfrac{y}{\zeta}\right) & ; \text{for } 0 \le x \le \eta \\[3mm] w_0\left(-\dfrac{x}{\lambda} - \dfrac{y}{\zeta} + \dfrac{\lambda + \eta}{\lambda}\right) & ; \text{for } \eta \le x \le \eta + \lambda \end{cases}$$

$$\tilde{w}(x, y) = \begin{cases} \tilde{w}_0\left(\dfrac{x}{\eta} - \dfrac{y}{\zeta}\right) & ; \text{for } 0 \le x \le \eta \\[3mm] \tilde{w}_0\left(-\dfrac{x}{\lambda} - \dfrac{y}{\zeta} + \dfrac{\lambda + \eta}{\lambda}\right) & ; \text{for } \eta \le x \le \eta + \lambda \end{cases}$$

From the theory of moderately large displacement of plates and the above postulated displacement field, one can derive the strain field with initial imperfections effect as follows:

49

$$\varepsilon_{\alpha\beta} = \frac{1}{2}(u_{\alpha,\beta} + u_{\beta,\alpha}) + \frac{1}{2}(w_{,\alpha}\, w_{,\beta} - \tilde{w}_{,\alpha}\, \tilde{w}_{,\beta})$$

That is

$$\varepsilon_x = \frac{\partial u}{\partial x} + \frac{1}{2}\left[\left(\frac{\partial w}{\partial x}\right)^2 - \left(\frac{\partial \tilde{w}}{\partial x}\right)^2\right]$$

$$\varepsilon_y = \frac{\partial v}{\partial y} + \frac{1}{2}\left[\left(\frac{\partial w}{\partial y}\right)^2 - \left(\frac{\partial \tilde{w}}{\partial y}\right)^2\right]$$

$$\varepsilon_{xy} = \frac{1}{2}\left(\frac{\partial u}{\partial y} + \frac{\partial v}{\partial x}\right) + \frac{1}{2}\left(\frac{\partial w}{\partial x}\frac{\partial w}{\partial y} - \frac{\partial \tilde{w}}{\partial x}\frac{\partial \tilde{w}}{\partial y}\right)$$

The detailed derivation is presented in Appendix B.1 on page 153 and the final result is:

$$\varepsilon_x = \begin{cases} -\dfrac{1}{\eta}u^* + \dfrac{1}{2\eta^2}\left(w_0^{\,2} - \tilde{w}_0^{\,2}\right) & ;\text{for } 0 \leq x \leq \eta \\[3mm] -\dfrac{1}{\lambda}u_0 + \dfrac{1}{\lambda}u^* + \dfrac{1}{2\lambda^2}\left(w_0^{\,2} - \tilde{w}_0^{\,2}\right) & ;\text{for } \eta \leq x \leq \eta + \lambda \end{cases} \tag{3.1}$$

$$\varepsilon_y = \frac{1}{2\zeta^2}\left(w_0^{\,2} - \tilde{w}_0^{\,2}\right) \qquad ;\text{everywhere} \tag{3.2}$$

$$\varepsilon_{xy} = \begin{cases} \dfrac{1}{2\zeta}u^* - \dfrac{1}{2\eta\zeta}\left(w_0^{\,2} - \tilde{w}_0^{\,2}\right) & ;\text{for } 0 \leq x \leq \eta \\[3mm] \dfrac{1}{2\zeta}u^* + \dfrac{1}{2\lambda\zeta}\left(w_0^{\,2} - \tilde{w}_0^{\,2}\right) & ;\text{for } \eta \leq x \leq \eta + \lambda \end{cases} \tag{3.3}$$

We also need to introduce a curvature field with initial imperfection effect given by,

$$\kappa_{\alpha\beta} = -\left[\frac{\partial^2}{\partial x_\alpha \partial x_\beta}(w - \tilde{w})\right] = (w - \tilde{w})_{,\alpha\beta}$$

3.2 Load-displacement Curve

The load-displacement curve is derived using the principal of virtual work as introduced in Chapter 2. The potential energy, Π, written as a function of the membrane and bending energies is minimized to lead to a set of two nonlinear algebraic equations. The solution of these equations describes the behavior of the structure in terms of a load-displacement curve.

The membrane and bending energies are derived in the same manner as for the case of no initial imperfections. Using the strain field result (Eqs. (3.1), (3.2), and (3.3)) in the expressions for the membrane and bending energies, and the following expressions for the average curvatures

$$(\kappa_x)_{avg} = \begin{cases} (\kappa_{x_I})_{avg} = \dfrac{w_0 - \tilde{w}_0}{\eta^2} \ ; \text{for } 0 \le x \le \eta \\[3mm] (\kappa_{x_{II}})_{avg} = \dfrac{w_0 - \tilde{w}_0}{\lambda^2} \ ; \text{for } \eta \le x \le \eta + \lambda \end{cases}$$

$$(\kappa_y)_{avg} = \dfrac{w_0 - \tilde{w}_0}{\zeta^2}$$

one gets, as detailed in Appendix B.2 on page 156, the following result for the membrane and bending energies with initial imperfections:

$$U_m = \frac{Et}{2(1-\nu^2)} \left[C_1\left(w_0^2 - \tilde{w}_0^2\right)^2 + C_2 u_0\left(w_0^2 - \tilde{w}_0^2\right) \right. $$
$$\left. + C_3 u^*\left(w_0^2 - \tilde{w}_0^2\right) + C_4 u^* u_0 + C_5 u^{*2} + C_6 u_0^2 \right]$$

and

$$U_b = \frac{Et^3}{24(1-\nu^2)} C_7 (w_0 - \tilde{w}_0)^2$$

where C_i ; ($i = 1, ..., 7$) are as defined in Appendix B.2 on page 156.

From the above expressions, the equilibrium path for an initially imperfect plate is derived. The buckling of real (and therefore imperfect) structures is gradual. Therefore, the equilibrium path for an initially imperfect plate is now described with one smooth curve where there is no distinction between the primary and secondary equilibrium paths. In essence, the introduction of initial imperfections, $\tilde{w}_0 \neq 0$, implies that $w_0 \neq 0$ and therefore the secondary equilibrium path describes the entire equilibrium path. The final result is given in terms of the following two non-linear algebraic equations and is derived in Appendix B.3 on page 158.

$$P_{II} = \frac{Et}{1-v^2} \left\{ \left[2C_6 - \frac{C_4^2}{2C_5} - 2\frac{\left(C_2 - \frac{C_3 C_4}{2C_5}\right)^2}{\left(4C_1 - \frac{C_3^2}{C_5}\right)} \right] u_0 - \frac{t^2}{6} \frac{C_7\left(C_2 - \frac{C_3 C_4}{2C_5}\right)}{\left(4C_1 - \frac{C_3^2}{C_5}\right)} \left(1 - \frac{\tilde{w}_0}{w_0}\right) \right\} \tag{3.4}$$

and

$$u_0 = -\frac{\left(4C_1 - \frac{C_3^2}{C_5}\right)}{\left(2C_2 - \frac{C_3 C_4}{C_5}\right)}\left(w_0^2 - \tilde{w}_0^2\right) - \frac{\frac{C_7 t^2}{6}}{\left(2C_2 - \frac{C_3 C_4}{C_5}\right)}\left(1 - \frac{\tilde{w}_0}{w_0}\right) \tag{3.5}$$

Expressions (3.4) and (3.5) furnish a system of two equations with two unknowns, P and w_0. Given u_0 and for some value of the imperfection $\tilde{w}_0$ one finds w_0 from Eq. (3.5), then P from Eq. (3.4).

3.3 Non-dimensionalization

In what follows, we find a non-dimensional form for Eqs. (3.4) and (3.5). Making use of the non-dimensional parameters $\bar{\zeta} = \dfrac{\zeta}{R}$, $\bar{P} = \dfrac{PR}{D}$, and $\bar{u} = \dfrac{uR}{t^2}$, introduced in Section 2.3 on page 21, one can derive the following two dimensionless equations which describe the equilibrium path for the initially imperfect plate.

$$\bar{P} = 12\left[2\bar{C}_6 - \frac{\bar{C}_4^2}{2\bar{C}_5} - 2\frac{\left(\bar{C}_2 - \frac{\bar{C}_3\bar{C}_4}{2\bar{C}_5}\right)^2}{\left(4\bar{C}_1 - \frac{\bar{C}_3^2}{\bar{C}_5}\right)}\right]\bar{u}_0 - \frac{2\bar{C}_7\left(\bar{C}_2 - \frac{\bar{C}_3\bar{C}_4}{2\bar{C}_5}\right)}{\left(4\bar{C}_1 - \frac{\bar{C}_3^2}{\bar{C}_5}\right)}\left(1 - \frac{\tilde{w}_0}{w_0}\right) \tag{3.6}$$

and

$$\bar{u}_0 = -\frac{\left(4\bar{C}_1 - \frac{\bar{C}_3^2}{\bar{C}_5}\right)}{\left(2\bar{C}_2 - \frac{\bar{C}_3\bar{C}_4}{\bar{C}_5}\right)}\left[\left(\frac{w_0}{t}\right)^2 - \left(\frac{\tilde{w}_0}{t}\right)^2\right] - \frac{\bar{C}_7}{6\left(2\bar{C}_2 - \frac{\bar{C}_3\bar{C}_4}{\bar{C}_5}\right)}\left(1 - \frac{\tilde{w}_0}{w_0}\right) \tag{3.7}$$

where

$$\bar{C}_1 = \frac{1}{8}\frac{\bar{\zeta}}{\bar{\eta}^3} + \frac{1}{8}\frac{\bar{\eta}}{\bar{\zeta}^3} + \frac{1}{4}\frac{1}{\bar{\eta}\bar{\zeta}} + \frac{1}{8}\frac{\bar{\zeta}}{\bar{\lambda}^3} + \frac{1}{8}\frac{\bar{\lambda}}{\bar{\zeta}^3} + \frac{1}{4}\frac{1}{\bar{\lambda}\bar{\zeta}}$$

$$\bar{C}_2 = -\frac{1}{2}\frac{\bar{\zeta}}{\bar{\lambda}^2} - \frac{1}{2}\frac{\nu}{\bar{\zeta}}$$

$$\bar{C}_3 = -\frac{1}{2}\frac{\bar{\zeta}}{\bar{\eta}^2} - \frac{1}{2}\frac{\bar{\zeta}}{\bar{\lambda}^2}$$

$$\bar{C}_4 = -\frac{\bar{\zeta}}{\bar{\lambda}}$$

$$\overline{C}_5 = \frac{1}{2}\frac{\overline{\zeta}}{\eta} + \frac{1}{4}\frac{\overline{\eta}}{\zeta} - \frac{1}{4}\frac{v\overline{\eta}}{\zeta} + \frac{1}{2}\frac{\overline{\zeta}}{\lambda} + \frac{1}{4}\frac{\overline{\lambda}}{\zeta} - \frac{1}{4}\frac{v\overline{\lambda}}{\zeta}$$

$$\overline{C}_6 = \frac{1}{2}\frac{\overline{\zeta}}{\lambda}$$

$$\overline{C}_7 = \frac{\overline{\zeta}}{\overline{\eta}^3} + \frac{\overline{\eta}}{\overline{\zeta}^3} + \frac{2}{\overline{\zeta}\eta} + \frac{\overline{\zeta}}{\overline{\lambda}^3} + \frac{\overline{\lambda}}{\overline{\zeta}^3} + \frac{2}{\lambda\zeta}$$

The details of the derivation are omitted because the procedure is similar to the one used in Appendix A.5 on page 145.

Now, defining two new non-dimensional parameters $\overline{w}_0$ and r as follows:

$$\overline{w}_0 = \frac{w_0}{t}$$

and

$$r = \frac{\tilde{w}_0}{t}$$

Eqs. (3.6) and (3.7) can be rewritten in the following final form:

$$P = 12\left[2\overline{C}_6 - \frac{\overline{C}_4^2}{2\overline{C}_5} - 2\frac{\left(\overline{C}_2 - \dfrac{\overline{C}_3\overline{C}_4}{2\overline{C}_5}\right)^2}{\left(4\overline{C}_1 - \dfrac{\overline{C}_3^2}{\overline{C}_5}\right)}\right]\overline{u}_0 - \frac{2\overline{C}_7\left(\overline{C}_2 - \dfrac{\overline{C}_3\overline{C}_4}{2\overline{C}_5}\right)}{\left(4\overline{C}_1 - \dfrac{\overline{C}_3^2}{\overline{C}_5}\right)}\left(1 - \frac{r}{\overline{w}_0}\right) \qquad (3.8)$$

$$\bar{u}_0 = -\frac{\left(4\bar{C}_1 - \dfrac{\bar{C}_3^2}{\bar{C}_5}\right)}{\left(2\bar{C}_2 - \dfrac{\bar{C}_3\bar{C}_4}{\bar{C}_5}\right)}\left(\bar{w}_0^2 - r^2\right) - \frac{\bar{C}_7}{6\left(2\bar{C}_2 - \dfrac{\bar{C}_3\bar{C}_4}{\bar{C}_5}\right)}\left(1 - \frac{r}{\bar{w}_0}\right) \qquad (3.9)$$

Fig. 3.2, shows $\bar{P}$ vs. $\bar{u}_0$ for three different values of the initial imperfection magnitude parameter r ($r = 1, 2,$ and 3). When constructing the load-displacement curve, the values $\bar{P}$ are found for each increment in $\bar{u}_0$ by minimizing $\bar{P}$ with respect to ζ. Therefore, each point of the curve is characterized by an in-plane displacement $\bar{u}_0$ and its corresponding minimum load $\bar{P}$ with respect to ζ. As loading progresses, ζ decreases continuously until the membrane yield of the material corresponding to $\bar{\zeta}_u$ is reached.

3.4 Membrane Yield

The most stressed part of the material and corresponding non-dimensional ultimate load $\bar{P}_u$ are found in the same manner as for the case with no initial imperfection. First, the expressions for the axial and shear strains are conveniently expressed as follows:

$$\varepsilon_x = \begin{cases} D_1 u_0 + D_2\left(1 - \dfrac{\tilde{w}_0}{w_0}\right) & ; \text{for } 0 \leq x \leq \eta \\[3mm] (D_1^*)\, u_0 + (D_2^*)\left(1 - \dfrac{\tilde{w}_0}{w_0}\right) & ; \text{for } \eta \leq x \leq \eta + \lambda \end{cases}$$

$$\varepsilon_y = D_3 u_0 + D_4\left(1 - \dfrac{\tilde{w}_0}{w_0}\right) = (D_3^*)\, u_0 + (D_4^*)\left(1 - \dfrac{\tilde{w}_0}{w_0}\right) \qquad ; \text{everywhere}$$

$$\varepsilon_{xy} = \begin{cases} D_5 u_0 + D_6\left(1 - \dfrac{\tilde{w}_0}{w_0}\right) & ; \text{for } 0 \leq x \leq \eta \\[3mm] (D_5^*)\, u_0 + (D_6^*)\left(1 - \dfrac{\tilde{w}_0}{w_0}\right) & ; \text{for } \eta \leq x \leq \eta + \lambda \end{cases}$$

where the parameters $D_i(\zeta)$; $(i = 1, ..., 6)$ and $D_i^*(\zeta)$; $(i = 1, ..., 6)$ remain identical to the ones derived in Appendix A.6 on page 147.

Using the above equations in the plane stress yield condition (Eq. (2.32) on page 31) yields a quadratic equation in u_0,

$$A u_0^2 + B\left(1 - \frac{\tilde{w}_0}{w_0}\right)u_0 + \left[C\left(1 - \frac{\tilde{w}_0}{w_0}\right)^2 - \left(\frac{\sigma_0}{E}\right)^2\right] = 0 \qquad (3.10)$$

from which the following dimensionless form, as detailed in Appendix B.4 on page 160, is derived:

$$\bar{A}\bar{u}_0^2 + \bar{B}\left(1 - \frac{r}{w_0}\right)\bar{u}_0 + \left[\bar{C}\left(1 - \frac{r}{w_0}\right)^2 - \frac{1}{\beta^4}\right] = 0 \qquad (3.11)$$

For a given slenderness parameter ratio, $\beta = \frac{t}{R}\sqrt{\frac{E}{\sigma_0}}$, and for some value of the initial imperfection r, the ultimate load $\overline{P}_u$ is found from Eqs. (3.8), (3.9), and (3.11). The methodology is to determine $\bar{u}_0$ as function of $\bar{\zeta}$ for every increment in $\overline{w}_0$ using Eq. (3.9). This result in Eq. (3.8) gives $\bar{P}$ as function of $\bar{\zeta}$. Minimization with respect to $\bar{\zeta}$ leads to a $\bar{P}$ and $\bar{u}_0$ for each increment $\overline{w}_0$. The found value $\bar{u}_0$ is used to construct the left hand side of Eq. (3.11). Membrane yield commences at the first positive root, $(\overline{w}_0)_u$, of Eq. (3.11). Finally, from this solution ultimate load $\overline{P}_u$ and corresponding $\bar{\zeta}_u$ are found.

In Fig. 3.2, the membrane yield for the special case $\beta = 0.2315$ is represented by an asterisk symbol '*' for the three initial imperfection magnitude parameter $r=1$, 2, and 3. As an illustration of the final results, we find for $r = 3$ the following:

$$\overline{P}_u = 70$$

$$(\overline{u_0})_u = 18$$

$$\overline{\zeta}_u = 0.8$$
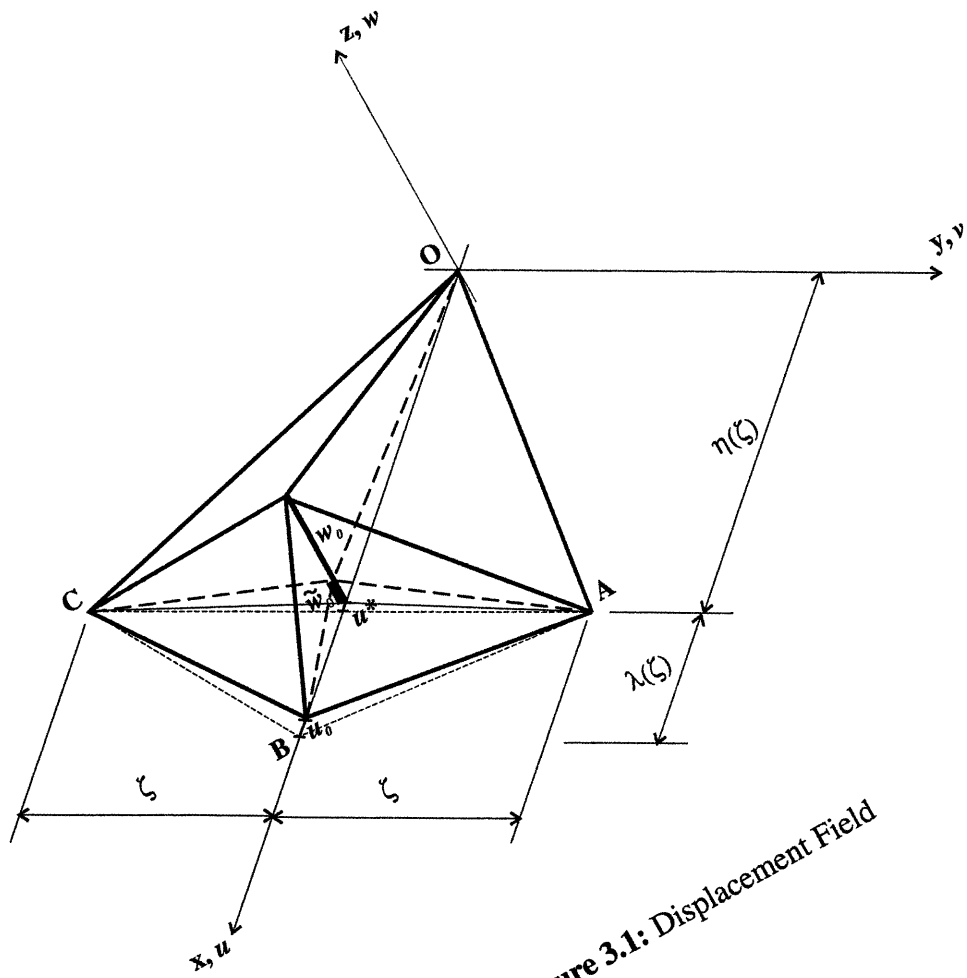
Figure 3.1: Displacement Field
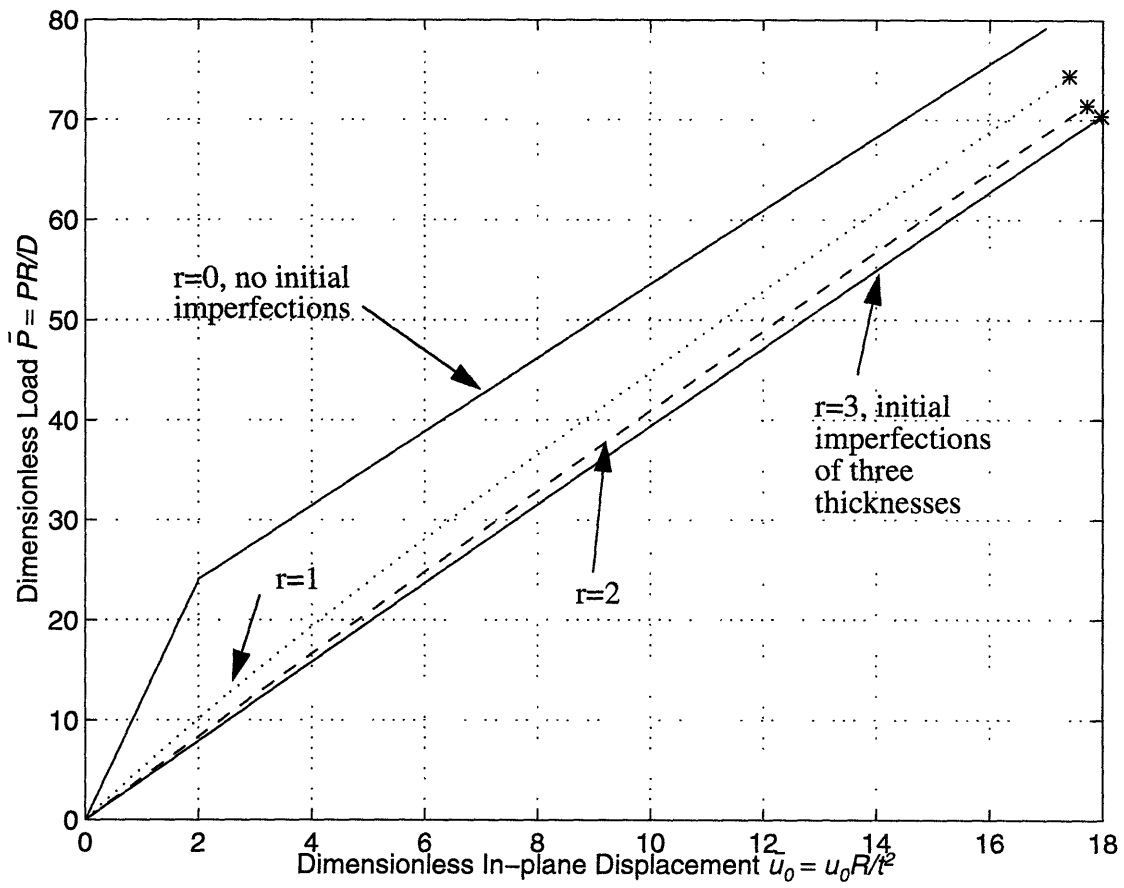
Figure 3.2: Load-deflection Curves for Several Values of Initial Imperfections

Chapter 4

Circular Flanged Plates: Post-failure Analysis

In this chapter, we develop a computational model for analysis of the plate crushing resistance in the post-failure phase. Using limit analysis, applied incrementally up to large displacements and rotations, an approximate solution for the load-deformation relationship is obtained. In this post-failure phase, the process is characterized by falling loads due to plastic folding, with large strains (up to the rupture strain of the material) and large rotations.

4.1 One-degree-of-freedom Model

Once the ultimate strength evaluated from the membrane yield condition in Section 2.7 on page 30 is reached, the plate load carrying capacity decreases. Our two-degree-of-freedom model developed in Section 2.1.2 on page 18 can be extended into the post-failure range. This model is valid up to the point of the membrane yield. Beyond this point, the plate is subjected to further unloading, and plastic deformations spread outside of the bounded region. From experimental observations, referring to Fig. 2.4 on page 37, five hinge lines 'OD', 'OE', 'DE', 'AD', and 'CE' are activated. From this point on, the in-

plane and out-of-plane deformations are related through the geometry of the problem and the number of degrees of freedom is reduced to one. Fig. 4.1, shows a one-degree-of-freedom model based on the above discussion. As indicated, the curved hinge lines are all approximated by straight ones.

Further experimental observations reveal that after a slight increase in the amount of axial deflection, the out-of-plane displacement w_1 grows in much faster proportion than w_0 ($w_1 \gg w_0$). To simplify the calculation, we assume that $w_0 \approx 0$. Under this assumption, a final simplified one-degree-of-freedom model is constructed and shown in Fig. 4.2. Because of symmetry, only half of the model is considered. The notation is defined as follows:

ζ - parameter that determines the location of all hinge lines

R - specimen radius

θ_i - rotation of the ith hinge line ($i = 1, ..., 5$)

l_i - length of the ith hinge line ($i = 1, ..., 5$)

α - angle between first and second hinge lines

β - angle between second and fifth hinge lines

γ - angle between third and fourth hinge lines

δ - angle between third and fifth hinge lines

ϕ_1 - projection of ($\alpha + \beta$)

ϕ_2 - projection of ($\gamma + \delta$)

P - applied force

Δ - indentation depth

As crushing progresses, the second and third hinge lines move out-of-plane while the first, fourth, and fifth hinge lines remain in-plane. An overlap between the adjacent left and right triangular elements is induced. This overlap is indicated by a shaded area and represents the amount of compression each deformed triangular element is subjected to.

Note that the angles α, β, γ, and δ are determined from the geometry of the problem. They are function of the parameter ζ and found in Appendix C.1 on page 163 to be:

$$\alpha(\zeta) = \text{atan}\left(\frac{\sqrt{R^2 - \zeta^2}}{R + \zeta}\right)$$

$$\beta(\zeta) = \frac{\pi}{2} - 2\alpha(\zeta)$$

$$\gamma(\zeta) = \alpha(\zeta)$$

$$\delta = \frac{\pi}{2}$$

4.2 General Solution Approach and Idealization

McClintock and Argon (1966) state the upper bound theorem as follows:

In a rigid-plastic continuum, deformation must occur under any system of loads, F_i, for which a distribution of incremental displacements, $\dot{u}_i$, can be found such that

(a) the displacement boundary conditions, if any, are satisfied,

(b) the displacements can be differentiated to give a strain, $\dot{\varepsilon}_{ij}$, with no change in volume anywhere, and

(c) the resulting plastic work done throughout the volume, V, of material, found from the resulting strain, is less than (or equal to) the work done by the external loads acting through the assumed displacements:

$$\int_S F_i \dot{u}_i dS \geq \int_V \sigma_{ij} \dot{\varepsilon}_{ij} dV$$

where σ_{ij} are the components of the stress tensor, and $i,j=1,2,3$ in indicial notation.

If it is assumed that in the plate there are no through thickness components of displacement or gradient $\left(u_3 = 0 , \dfrac{\partial}{\partial x_3} = 0 \right)$, then $i, j \rightarrow \alpha, \beta = 1, 2$. It turns out that the volume integral can be rewritten in terms of the bending moment times the rate of curvature, $M_{\alpha\beta} \dot{\kappa}_{\alpha\beta}$, and the axial force times the strain rate, $N_{\alpha\beta} \dot{\varepsilon}_{\alpha\beta}$, over an area, S, as

$$\int_S F_i \dot{u}_i dS \geq \int_S (M_{\alpha\beta} \dot{\kappa}_{\alpha\beta} + N_{\alpha\beta} \dot{\varepsilon}_{\alpha\beta}) \, dS \tag{4.1}$$

Note that the bending moment and force tensors, $M_{\alpha\beta}$ and $N_{\alpha\beta}$, are coupled through the yield criterion of the functional form $f(M_{\alpha\beta}, N_{\alpha\beta}) = 0$. It is assumed that in regions experiencing high bending stresses, there are small membrane stresses. Likewise, in regions of high membrane stresses, there are small bending stresses. This decoupling of $M_{\alpha\beta}$ and $N_{\alpha\beta}$ is accomplished by inscribing the yield locus inside a rectangle as in Fig. 4.3.

The right hand side of Eq. (4.1), that is the rate of internal plastic work, is now the sum of internal bending work rate and membrane work rate and expressed as follows:

$$\dot{W}_{in} = \dot{W}_B + \dot{W}_M \tag{4.2}$$

where

$$\dot{W}_B = \int_S M_{\alpha\beta} \dot{\kappa}_{\alpha\beta} dS + \sum_i M_0 \left[\dot{\theta}_i \right] l_i \tag{4.3}$$

$$\dot{W}_M = \int_S N_{\alpha\beta} \dot{\varepsilon}_{\alpha\beta} dS \tag{4.4}$$

For a rigid-perfectly plastic material, the bending expression contains a continuous deformation field as well as a discontinuous field, where $M_0 = \dfrac{\sigma_0 t^2}{4}$ is the fully plastic bending moment, $\dot{\theta}_i$ is the rate of rotation at the ith plastic hinge and l_i is the length of the hinge line.

In our model, as is done in most practical applications, the velocity fields were constructed so that the plastic bending deformations are contained only in plastic hinges and plane deformations between them. Consequently, the plane rate tensor in the continuous deformation region vanishes ($\dot{\kappa}_{\alpha\beta} = 0$) and Eq. (4.3) simplifies to

$$\dot{W}_B = \sum_i M_0 \left[\dot{\theta}_i \right] l_i \tag{4.5}$$

Also, the membrane work rate (Eq. (4.4)) is simplified by identifying direction of a predominant axial deformation and neglecting all other components of the strain rate tensor. The membrane work rate takes the following form

$$\dot{W}_M = \int_S N_0 \dot{\varepsilon}\, dS \tag{4.6}$$

where $N_0 = \sigma_0 t$ is the fully plastic membrane force.

In the case of a single applied load P, the external work rate is

$$\dot{W}_{ext} = P \dot{\Delta} \tag{4.7}$$

where $\dot{\Delta}$ is the rate of indentation.

4.3 Rate of Internal Plastic Work

In what follows, we derive the rate of internal plastic work for our simplified one-degree-of-freedom model. As explained in the previous section, the internal bending work rate and membrane work rate are calculated separately. Their sum, Eq. (4.2) is the internal plastic work rate.

4.3.1 Bending Work Rate

As established earlier, the internal bending work rate is given by Eq. (4.5). For our model with five hinge lines, we have

$$\dot{W}_B = \sum_{i=1}^{5} M_0 [\dot{\theta}_i] l_i \tag{4.8}$$

where, recall

$\dot{\theta}_i$ - is the rate of rotation at the ith plastic hinge

l_i - is the length of the ith hinge line

$M_0 = \dfrac{\sigma_0 t^2}{4}$ - is the fully plastic bending moment

Expansion of Eq. (4.8), considering the entire plate, gives

$$\dot{E}_B = 2M_0 \left([\dot{\theta}_1] l_1 + [\dot{\theta}_2] l_2 + [\dot{\theta}_3] l_3 + [\dot{\theta}_4] l_4 + [\dot{\theta}_5] l_5 \right)$$

which from geometry
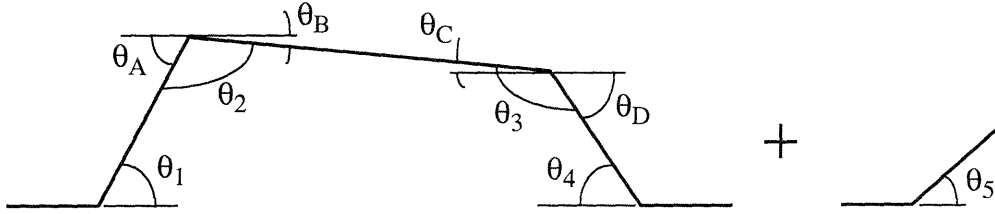
becomes

$$\dot{E}_B = 2M_0 \left(\dot{\theta}_1 l_1 + \dot{\theta}_A l_2 + \dot{\theta}_B l_2 + \dot{\theta}_D l_3 - \dot{\theta}_C l_3 + \dot{\theta}_4 l_4 + \dot{\theta}_5 l_5 \right)$$

and reduces to

$$\dot{E}_B = 2M_0 \left[\dot{\theta}_1 l_1 + (\dot{\theta}_A + \dot{\theta}_B) l_2 + (\dot{\theta}_D - \dot{\theta}_C) l_3 + \dot{\theta}_4 l_4 + \dot{\theta}_5 l_5 \right] \qquad (4.9)$$

Also from geometry we have:

$$\theta_A + \theta_B = \pi - \theta_2 \quad \Rightarrow \quad \dot{\theta}_A + \dot{\theta}_B = -\dot{\theta}_2 \qquad (4.10)$$

and

$$\theta_D - \theta_C = \pi - \theta_3 \quad \Rightarrow \quad \dot{\theta}_D - \dot{\theta}_C = -\dot{\theta}_3 \qquad (4.11)$$

Eqs. (4.10) and (4.11) in (4.9) gives:

$$\dot{W}_B = 2M_0 \left(\dot{\theta}_1 l_1 - \dot{\theta}_2 l_2 - \dot{\theta}_3 l_3 + \dot{\theta}_4 l_4 + \dot{\theta}_5 l_5 \right) \qquad (4.12)$$

66

At this point, we need to determine the rate of rotations $\dot{\theta}_i$, $(i = 1, ..., 5)$. We first find from geometry the rotations θ_i as detailed in Appendix C.2 on page 164. The final result is as follows:

$$\cos\theta_1 = \frac{\cos\beta - \cos\alpha\cos\phi_1}{\sin\alpha\sin\phi_1} \tag{4.13}$$

$$\cos\theta_2 = \frac{\cos\phi_1 - \cos\alpha\cos\beta}{\sin\alpha\sin\beta} \tag{4.14}$$

$$\cos\theta_3 = \frac{\cos\phi_2}{\sin\alpha} \tag{4.15}$$

$$\cos\theta_4 = -\frac{\cos\alpha\cos\phi_2}{\sin\alpha\sin\phi_2} \tag{4.16}$$

$$\cos\theta_5 = \frac{\cos\alpha - \cos\beta\cos\phi_1}{\sin\beta\sin\phi_1} \tag{4.17}$$

Alternatively, as explained in Appendix C.2 on page 164, θ_5 is also found to be

$$\cos\theta_5 = \frac{\cos\alpha}{\sin\phi_2} \tag{4.18}$$

Differentiation of Eqs. (4.13) through (4.18) with respect to time leads to the following rate of rotations

$$\dot{\theta}_1 = -\dot{\phi}_1 \frac{\cos\alpha - \cos\beta\cos\phi_1}{\sin\phi_1\sqrt{(\sin\alpha)^2 - (\cos\beta)^2 + 2\cos\alpha\cos\beta\cos\phi_1 - (\cos\phi_1)^2}} \tag{4.19}$$

$$\dot{\theta}_2 = \dot{\phi}_1 \frac{\sin\phi_1}{\sqrt{(\sin\alpha)^2 - (\cos\beta)^2 + 2\cos\alpha\cos\beta\cos\phi_1 - (\cos\phi_1)^2}} \tag{4.20}$$

$$\dot\theta_3 = \dot\phi_2 \frac{\sin\phi_2}{\sqrt{(\sin\alpha)^2 - (\cos\phi_2)^2}} \qquad (4.21)$$

$$\dot\theta_4 = -\dot\phi_2 \frac{\cos\alpha}{\sin\phi_2\sqrt{(\sin\alpha)^2 - (\cos\phi_2)^2}} \qquad (4.22)$$

$$\dot\theta_5 = -\dot\phi_1 \frac{\cos\beta - \cos\alpha\cos\phi_1}{\sin\phi_1\sqrt{(\sin\alpha)^2 - (\cos\beta)^2 + 2\cos\alpha\cos\beta\cos\phi_1 - (\cos\phi_1)^2}} \qquad (4.23)$$

or alternatively

$$\dot\theta_5 = \dot\phi_2 \frac{\cos\alpha\cos\phi_2}{\sin\phi_2\sqrt{(\sin\alpha)^2 - (\cos\phi_2)^2}} \qquad (4.24)$$

Using Eqs. (4.19) through (4.23) in Eq. (4.12), gives the following expression for the bending work rate.

$$\dot W_B = 2M_0 \left\{ \dot\phi_1 l_1 \frac{\cos\beta\cos\phi_1 - \cos\alpha}{\sin\phi_1\sqrt{(\sin\alpha)^2 - (\cos\beta)^2 + 2\cos\alpha\cos\beta\cos\phi_1 - (\cos\phi_1)^2}} \right. \qquad (4.25)$$
$$- \dot\phi_1 l_2 \frac{\sin\phi_1}{\sqrt{(\sin\alpha)^2 - (\cos\beta)^2 + 2\cos\alpha\cos\beta\cos\phi_1 - (\cos\phi_1)^2}}$$
$$- \dot\phi_2 l_3 \frac{\sin\phi_2}{\sqrt{(\sin\alpha)^2 - (\cos\phi_2)^2}} - \dot\phi_2 l_4 \frac{\cos\alpha}{\sin\phi_2\sqrt{(\sin\alpha)^2 - (\cos\phi_2)^2}}$$
$$\left. - \dot\phi_1 l_5 \frac{\cos\beta - \cos\alpha\cos\phi_1}{\sin\phi_1\sqrt{(\sin\alpha)^2 - (\cos\beta)^2 + 2\cos\alpha\cos\beta\cos\phi_1 - (\cos\phi_1)^2}} \right\}$$

In order to eliminate $\dot\phi_2$ from the above equation, one can use Eqs. (4.23) and (4.24) to get $\dot\phi_2$ in terms of $\dot\phi_1$.

68

$$\dot{\phi}_2 = \dot{\phi}_1 \frac{\sin\phi_2 (\cos\alpha\cos\phi_1 - \cos\beta) \sqrt{(\sin\alpha)^2 - (\cos\phi_2)^2}}{\cos\alpha\cos\phi_2 \sin\phi_1 \sqrt{(\sin\alpha)^2 - (\cos\beta)^2 + 2\cos\alpha\cos\beta\cos\phi_1 - (\cos\phi_1)^2}} \quad (4.26)$$

Finally, Eq. (4.26) in (4.25) give the following final result for the internal bending work rate

$$\dot{W}_B = \frac{2M_0\dot{\phi}_1}{\sin\phi_1 \sqrt{(\sin\alpha)^2 - (\cos\beta)^2 + 2\cos\alpha\cos\beta\cos\phi_1 - (\cos\phi_1)^2}} \quad (4.27)$$

$$\left[l_1 (\cos\beta\cos\phi_1 - \cos\alpha) - l_2 (\sin\phi_1)^2 - \frac{l_3 (\sin\phi_2)^2 (\cos\alpha\cos\phi_1 - \cos\beta)}{\cos\alpha\cos\phi_2} \right.$$

$$\left. - l_4 \frac{\cos\alpha\cos\phi_1 - \cos\beta}{\cos\phi_2} + l_5 (\cos\alpha\cos\phi_1 - \cos\beta) \right]$$

where ϕ_2 is related to ϕ_1 as follows:

$$\sin\phi_2 = \frac{\cos\alpha\sin\beta\sin\phi_1}{\cos\alpha - \cos\beta\cos\phi_1} \quad (4.28)$$

This result is arrived to by combining Eqs. (4.17) and (4.18).

In Eq. (4.27) the hinge line lengths, which are assumed to remain constant during the deformation process, are found from geometry and given by

$$l_1 = R$$

$$l_2 = \sqrt{R^2 - \rho^2}$$

$$l_3 = \sqrt{\zeta^2 - \eta^2}$$

69

$$l_4 = \zeta$$

$$l_5 = \sqrt{(R - \zeta)^2 + (R - \lambda)^2}$$

Using the values of λ, ρ, and η from Appendix A.1 on page 135, we get:

$$l_1 = R \tag{4.29}$$

$$l_2 = \sqrt{R^2 + \frac{R^2\left(R^2 - \zeta^2\right)}{(R + \zeta)^2}} = R\sqrt{\frac{2R}{R + \zeta}} \tag{4.30}$$

$$l_3 = \sqrt{\zeta^2 + \frac{\zeta^2\left(R^2 - \zeta^2\right)}{(R + \zeta)^2}} = \zeta\sqrt{\frac{2R}{R + \zeta}} \tag{4.31}$$

$$l_4 = \zeta \tag{4.32}$$

$$l_5 = \sqrt{(R - \zeta)^2 + \left(R^2 - \zeta^2\right)} = \sqrt{2R(R - \zeta)} \tag{4.33}$$

Note that for convenience, in all subsequent derivations we will continue to denote the hinge line lengths by l_i.

4.3.2 Membrane Work Rate

As established earlier, the internal membrane work rate is given by Eq. (4.6). That is

$$\dot{W}_M = \int_S N_0 \dot{\varepsilon}\, dS \tag{4.34}$$

where $N_0 = \sigma_0 t$ is the fully plastic membrane force, $dS = dr\, ds$, and $\dot{\varepsilon} = \dfrac{d\dot{u}}{dr}$ is the velocity strain rate in the local coordinates (r, s) rotating with the plate element. Therefore, with the consideration that material points are on either side of the centerline of the shaded area in Fig. 4.2, Eq. (4.34) becomes

$$\dot{W}_M = \iint_{r\,s} N_0 \frac{d\dot{u}}{dr} dr ds = 2N_0 \int_0^s \dot{u} ds$$

that is

$$\dot{W}_M = 2N_0 \int_0^s \dot{u} ds \qquad (4.35)$$

There are two contributions to the membrane work rate. The first one from the compression of the flange and the second one from that of the web or bulkhead.

$$\dot{W}_M = \dot{W}_{M_{flange}} + \dot{W}_{M_{web}} \qquad (4.36)$$

Making use of Eq. (4.35) and according to the assumed deformation mode, as shown in Appendix C.3 on page 166, each contribution is given by

$$\dot{W}_{M_{flange}} = 2N_0 H \dot{\phi}_1 f(\phi_1, \phi_2) \qquad (4.37)$$

and

$$\dot{W}_{M_{web}} = N_0 \dot{\phi}_1 \left[(\lambda + \eta) g(\phi_1, \phi_2) + \lambda f(\phi_1, \phi_2) \right] \qquad (4.38)$$

where H is the width of the flange, $\lambda(\zeta)$ and $\eta(\zeta)$ are given by Eqs. (A.1) and (A.2) on page 135 and page 136 respectively,

$$f(\phi_1, \phi_2) \;=\; -l_5\sin\phi_1 + l_4\sin(\phi_1 + \phi_2) + \lambda\cos(\phi_1 + \phi_2)$$

$$+ \; [\,l_4\sin(\phi_1 + \phi_2) + \lambda\cos(\phi_1 + \phi_2)\,]$$

$$\left[\frac{\sin\phi_2\,(\cos\alpha\cos\phi_1 - \cos\beta)\,\sqrt{(\sin\alpha)^2 - (\cos\phi_2)^2}}{\cos\alpha\cos\phi_2\sin\phi_1\sqrt{(\sin\alpha)^2 - (\cos\beta)^2 + 2\cos\alpha\cos\beta\cos\phi_1 - (\cos\phi_1)^2}}\right]$$

$$g(\phi_1, \phi_2) \;=\; -l_5\sin\phi_1 + l_4\sin(\phi_1 + \phi_2) +$$

$$\frac{l_4\sin(\phi_1 + \phi_2)\,\sin\phi_2\,(\cos\alpha\cos\phi_1 - \cos\beta)\,\sqrt{(\sin\alpha)^2 - (\cos\phi_2)^2}}{\cos\alpha\cos\phi_2\sin\phi_1\sqrt{(\sin\alpha)^2 - (\cos\beta)^2 + 2\cos\alpha\cos\beta\cos\phi_1 - (\cos\phi_1)^2}}$$

and ϕ_1, ϕ_2 are related by Eq. (4.28).

4.4 Rate of External Work

As established earlier, the rate of external work is given by Eq. (4.7). That is

$$\dot{W}_{ext} = P\dot{\Delta} \tag{4.39}$$

where, recall

P - is the applied force

$\dot{\Delta}$ - is the rate of indentation depth

From geometry, as shown in Appendix C.4 on page 171, the rate of indentation depth is found as function of $\dot{\phi}_1$, ϕ_1, and ϕ_2 as follows:

72

$$\dot{\Delta} = \dot{\phi}_1 \, h \, (\phi_1, \phi_2) \tag{4.40}$$

where

$$h \, (\phi_1, \phi_2) = -l_5 \cos \phi_1 + l_4 \cos \, (\phi_1 + \phi_2) - \lambda \sin \, (\phi_1 + \phi_2)$$

$$+ \, [l_4 \cos \, (\phi_1 + \phi_2) - \lambda \sin \, (\phi_1 + \phi_2) \,]$$

$$\left[\frac{\sin \phi_2 \, (\cos \alpha \cos \phi_1 - \cos \beta) \sqrt{(\sin \alpha)^2 - (\cos \phi_2)^2}}{\cos \alpha \cos \phi_2 \sin \phi_1 \sqrt{(\sin \alpha)^2 - (\cos \beta)^2} + 2 \cos \alpha \cos \beta \cos \phi_1 - (\cos \phi_1)^2} \right]$$

And inserting Eq. (4.40) into Eq. (4.39) leads the following final result for the external work rate.

$$\dot{W}_{ext} = P \dot{\phi}_1 \, h \, (\phi_1, \phi_2) \tag{4.41}$$

4.5 Crushing Force

We now are in position to derive the crushing force, P, by equating the previously calculated internal work rates to the above rate of external work. That is

$$\dot{W}_{ext} = \dot{W}_{in} = \dot{W}_B + \dot{W}_{M_{flange}} + \dot{W}_{M_{web}} \tag{4.42}$$

Eqs. (4.27), (4.37), (4.38), and (4.41) in Eq. (4.42) gives, as shown in Appendix C.5 on page 173, an expression for the crushing force as follows:

$$P = 2M_0 \frac{k(\phi_1, \phi_2)}{h(\phi_1, \phi_2)} + N_0(2H + \lambda)\frac{f(\phi_1, \phi_2)}{h(\phi_1, \phi_2)} + N_0(\lambda + \eta)\frac{g(\phi_1, \phi_2)}{h(\phi_1, \phi_2)} \tag{4.43}$$

where

$$k(\phi_1, \phi_2) = \frac{1}{\sin\phi_1 \sqrt{(\sin\alpha)^2 - (\cos\beta)^2 + 2\cos\alpha\cos\beta\cos\phi_1 - (\cos\phi_1)^2}}$$
$$\left[l_1(\cos\beta\cos\phi_1 - \cos\alpha) - l_2(\sin\phi_1)^2 \right.$$
$$- l_3\frac{(\sin\phi_2)^2(\cos\alpha\cos\phi_1 - \cos\beta)}{\cos\alpha\cos\phi_2} - l_4\frac{\cos\alpha\cos\phi_1 - \cos\beta}{\cos\phi_2}$$
$$\left. + l_5(\cos\alpha\cos\phi_1 - \cos\beta) \right]$$

$$h(\phi_1, \phi_2) = -l_5\cos\phi_1 + l_4\cos(\phi_1 + \phi_2) - \lambda\sin(\phi_1 + \phi_2)$$

$$+ [l_4\cos(\phi_1 + \phi_2) - \lambda\sin(\phi_1 + \phi_2)]$$

$$\left[\frac{\sin\phi_2(\cos\alpha\cos\phi_1 - \cos\beta)\sqrt{(\sin\alpha)^2 - (\cos\phi_2)^2}}{\cos\alpha\cos\phi_2\sin\phi_1\sqrt{(\sin\alpha)^2 - (\cos\beta)^2 + 2\cos\alpha\cos\beta\cos\phi_1 - (\cos\phi_1)^2}} \right]$$

$$g(\phi_1, \phi_2) = -l_5\sin\phi_1 + l_4\sin(\phi_1 + \phi_2) +$$

$$\frac{l_4\sin(\phi_1 + \phi_2)\sin\phi_2(\cos\alpha\cos\phi_1 - \cos\beta)\sqrt{(\sin\alpha)^2 - (\cos\phi_2)^2}}{\cos\alpha\cos\phi_2\sin\phi_1\sqrt{(\sin\alpha)^2 - (\cos\beta)^2 + 2\cos\alpha\cos\beta\cos\phi_1 - (\cos\phi_1)^2}}$$

$$f(\phi_1, \phi_2) = -l_5 \sin\phi_1 + l_4 \sin(\phi_1 + \phi_2) + \lambda \cos(\phi_1 + \phi_2)$$

$$+ [l_4 \sin(\phi_1 + \phi_2) + \lambda \cos(\phi_1 + \phi_2)]$$

$$\left[\frac{\sin\phi_2 (\cos\alpha\cos\phi_1 - \cos\beta) \sqrt{(\sin\alpha)^2 - (\cos\phi_2)^2}}{\cos\alpha\cos\phi_2 \sin\phi_1 \sqrt{(\sin\alpha)^2 - (\cos\beta)^2 + 2\cos\alpha\cos\beta\cos\phi_1 - (\cos\phi_1)^2}} \right]$$

In all above relations, ϕ_1, and ϕ_2 are related by

$$\tan\phi_2 = \frac{\left(\dfrac{\cos\alpha\sin\beta\sin\phi_1}{\cos\alpha - \cos\beta\cos\phi_1} \right)}{\sqrt{1 - \left(\dfrac{\cos\alpha\sin\beta\sin\phi_1}{\cos\alpha - \cos\beta\cos\phi_1} \right)^2}} \tag{4.44}$$

(note that the use of $\tan\phi_2$ instead of $\sin\phi_2$, as done in Eq. (4.28), is for programing purposes.)

Also, ϕ_1 and ϕ_2 are geometrically related to Δ. The detail of the derivation is presented in Appendix C.4 on page 171. The final result is

$$\Delta = R - l_5 \sin\phi_1 + l_4 \sin(\phi_1 + \phi_2) + \lambda \cos(\phi_1 + \phi_2) \tag{4.45}$$

Eqs. (4.43), (4.44), and (4.45) represent a set of three equations with three unknowns ϕ_1, ϕ_2, and P. Given a Δ increment, ϕ_1 and ϕ_2 are calculated from Eqs. (4.45) and (4.44). The result is then used in Eq. (4.43) to lead the corresponding crushing load P. In this manner, the load-deflection curve is constructed as function of ζ for the post-failure stage.

For completeness, the remaining parameters are as follows:

$$\tan\alpha = \frac{\sqrt{R^2 - \zeta^2}}{R + \zeta} \ ; \qquad \beta = \frac{\pi}{2} - 2\alpha \ ;$$

$$l_1 = R \ ; \qquad l_2 = R\sqrt{\frac{2R}{R + \zeta}} \ ; \qquad l_3 = \zeta\sqrt{\frac{2R}{R + \zeta}} \ ;$$

$$l_4 = \zeta \ ; \qquad l_5 = \sqrt{2R(R - \zeta)} \ ;$$

$$\lambda = R - \sqrt{R^2 - \zeta^2} \ ; \qquad \eta = \frac{\zeta\sqrt{R^2 - \zeta^2}}{R + \zeta} \ ;$$

4.6 Non-dimensionalization

In what follows we derive a dimensionless form of Eqs. (4.43) and (4.45).

Staring from the dimensionless parameters defined in Section 2.3 on page 21, that is:

$$\bar{\zeta} = \frac{\zeta}{R} \ ; \qquad \bar{P} = \frac{PR}{D} \ ; \qquad \bar{\Delta} = \frac{\Delta R}{t^2} \ ;$$

where

$$D = \frac{Et^3}{12(1 - v^2)}$$

one can derive, as detailed in Appendix C.6 on page 174, the following dimensionless final expression for the loads in the post-failure phase

$$\bar{P} = \frac{12\bar{\sigma}(1 - v^2)}{\beta^2 \bar{h}}\left[\frac{\bar{k}}{2\bar{R}} + (2\bar{H} + \bar{\lambda})\ \bar{f} + (\bar{\lambda} + \bar{\eta})\bar{g}\right] \tag{4.46}$$

and the following dimensionless final expression for the corresponding deflections

$$\bar{\Delta} = \bar{R}^2 \left[1 - \bar{l}_5 \sin \phi_1 + \bar{l}_4 \sin (\phi_1 + \phi_2) + \bar{\lambda} \cos (\phi_1 + \phi_2) \right] \qquad (4.47)$$

where

$\beta = \dfrac{t}{R} \sqrt{\dfrac{E}{\sigma_Y}}$ is the slenderness ratio parameter

$\bar{\sigma} = \dfrac{\sigma_0}{\sigma_Y}$ is the ratio of the material flow stress to the material yield stress

$$\bar{R} = \frac{R}{t}, \bar{H} = \frac{H}{R}, \bar{\lambda} = 1 - \sqrt{1 - \bar{\zeta}^2}, \bar{\eta} = \frac{\bar{\zeta}\sqrt{1 - \bar{\zeta}^2}}{1 + \bar{\zeta}}, \bar{l}_4 = \bar{\zeta}, \bar{l}_5 = \sqrt{2(1 - \bar{\zeta})}$$

and

$\overline{h(\phi_1, \phi_2)}$, $\overline{k(\phi_1, \phi_2)}$, $\overline{f(\phi_1, \phi_2)}$, and $\overline{g(\phi_1, \phi_2)}$ are as defined in Appendix C.6 on page 174.

Also ϕ_1, and ϕ_2 are related as follows:

$$\tan \phi_2 = \frac{\left(\dfrac{\cos \alpha \sin \beta \sin \phi_1}{\cos \alpha - \cos \beta \cos \phi_1} \right)}{\sqrt{1 - \left(\dfrac{\cos \alpha \sin \beta \sin \phi_1}{\cos \alpha - \cos \beta \cos \phi_1} \right)^2}} \qquad (4.48)$$

To implement this result and plot the load-deflection characteristics, it is convenient to first increment ϕ_1 from ϕ_{1min} to ϕ_{1max}, find corresponding values of ϕ_2 from Eq. (4.48) insert both values, in Eqs. (4.47) and (4.46) and find respectively the values of $\bar{\Delta}$ and $\bar{P}$.

The limits of the angle ϕ_1 are found in Appendix C.7 on page 179 from geometric limitations imposed on the model. The corresponding final results are:

$$\phi_{1min} = 2\,\mathrm{atan}\left(\frac{\cos\alpha\sin\beta + \cos\beta\sin\alpha}{\cos\alpha + \cos\beta}\right)$$

and

$$\phi_{1max} = \alpha + \beta$$

Fig. 4.4, illustrates this final result. It is a plot of the dimensionless load-deflection characteristics for several values of the parameter $\bar{\zeta}$. Note that all the curves correspond to the special case where $\beta = 0.2315$ (slenderness ratio parameter of experimental specimen).

Front View Before Deformation
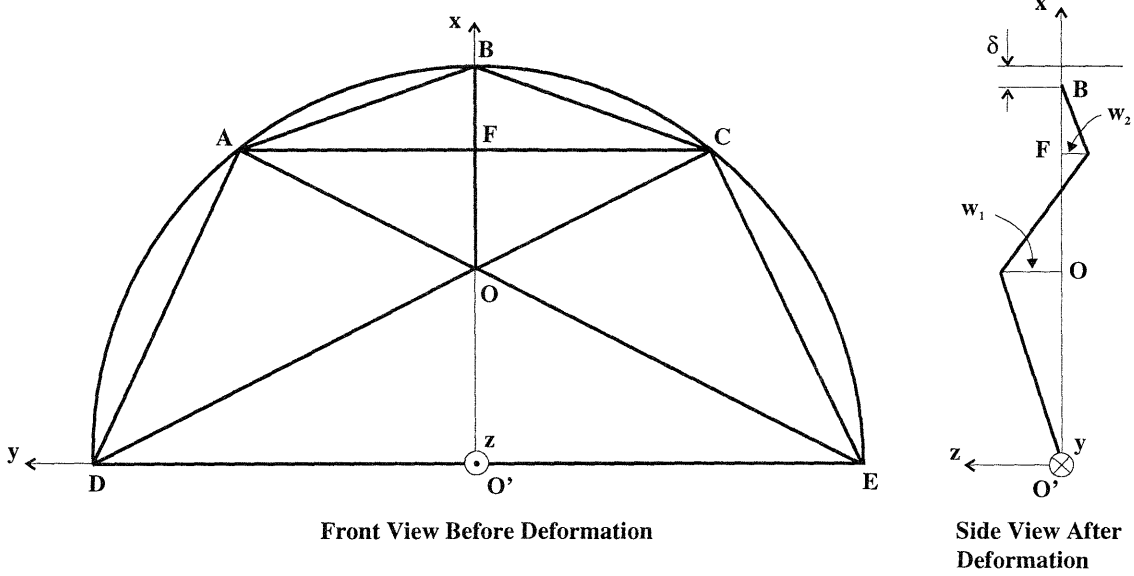
Side View After Deformation
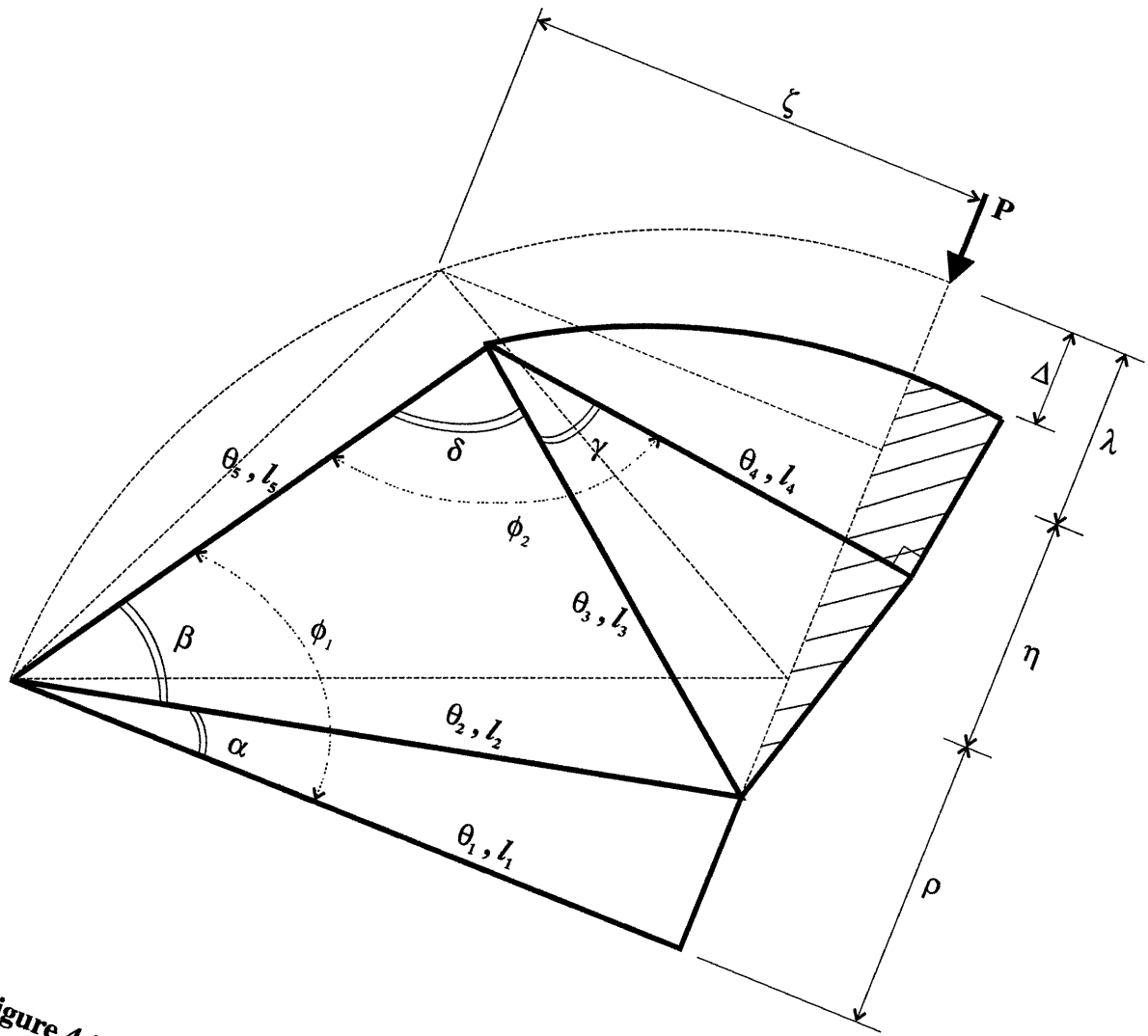
Figure 4.1: One-degree-of-freedom Model

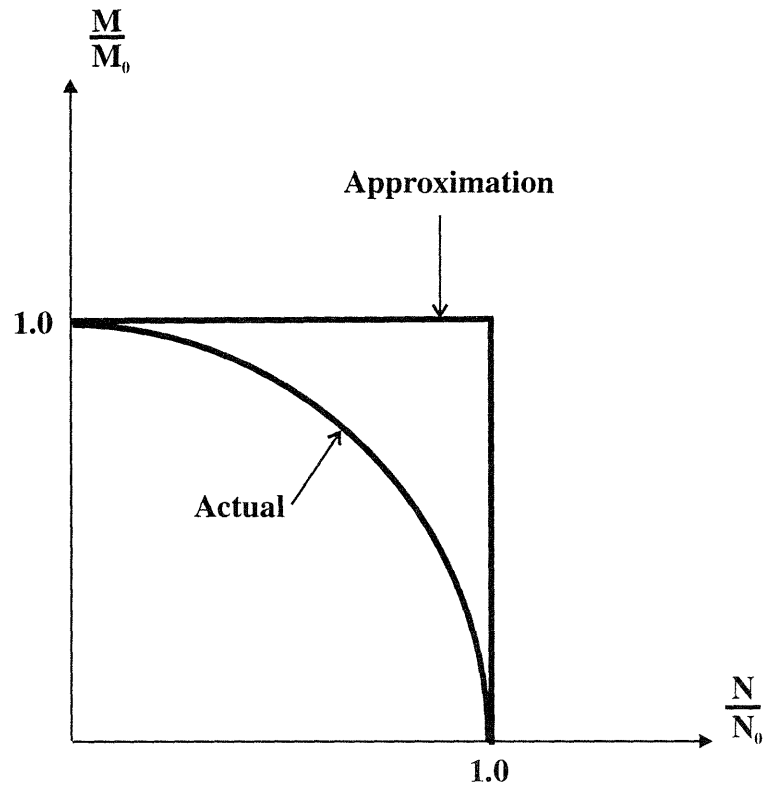**Figure 4.2:** Simplified One-degree-of-freedom Model

Figure 4.3: Decoupling of Yield Locus - Actual and Idealized
(only one quadrant shown)
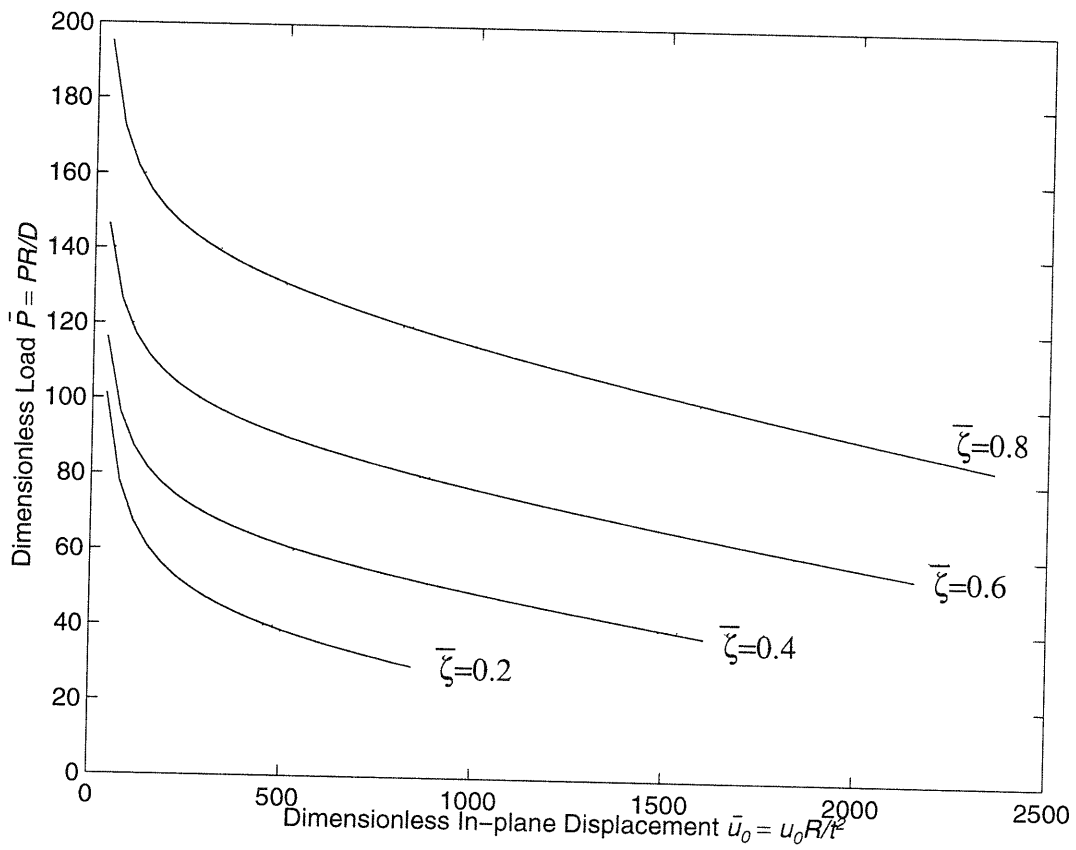
Figure 4.4: Dimensionless Load-deflection Curves in the Post-failure Range

Chapter 5

Circular Flanged Plates - Experimental Study

In this chapter, the experimental study undertaken in support of the project is described. First, the geometry of scale model specimens is determined and their fabrication is discussed. Next, the consideration, design, and fabrication of the testing apparatus are outlined, along with the choice of the indenters that simulate the accidental loadings. Finally, the description of the tests conducted and results obtained are presented.

Also supporting experiments described in Appendix D, related to finding the stiffness of the Instron machine (Section D.4 on page 190), investigating the specimen initial imperfections magnitude (Section D.5 on page 191), and determining the material stress-strain characteristic (Section D.6 on page 193) were undertaken.

5.1 Geometry and Fabrication of Experiment Specimens

Fig. 5.1 shows the geometry of the test specimen selected. It consists of a semi-circular plate (bulkhead) of radius R and thickness t, and the attached hull plating (flange) of width H and thickness t. In this section the sizing (i.e determination of R, t, and H) of the specimen and its fabrication are described.

5.1.1 Scale Model Geometry

The goal is to determine a realistic radius-to-thickness ratio (R/t) typically observed at the bulkhead-plating interface of ships bilge area, aircraft, and submarines. Depending on the application considered the geometric proportions vary, thus making it difficult to pick one typical design on which to base the scale test models. Furthermore, because of the unavailability of detailed technical drawings for aircraft fuselage and submarines, the scale models were based solely on ships bilge area. Three representative ship designs were selected. An average prototype radius-to-thickness ratio of $R/t = 136$, on which to base the scale models geometry, was found. Consult Appendix D.1 on page 185 for the details of the calculation. Also for completeness, as shown in Appendix D.2 on page 187, an order of magnitude of the radius-to-thickness ratio for aircraft and submarines was determined.

In determining the geometry of the models, for simplicity the bulkhead and flange thicknesses were taken equal. Four available plate thicknesses of 0.406, 0.749, 1.130, and 1.829 mm were evaluated. The 0.406 mm plate failed to meet the minimum thickness required for the selected welding technique. The 1.829 mm plate was not used because it exceeds the maximum thickness capacity of the machine used to roll the flange.

The next task was to evaluate the radius R that would yield a reasonably sized specimen. Based on the Instron machine workspace constraint, a radius of 6 in. (152.4 mm) was selected. Consequently, the plate thickness of 1.130 mm was preferred over the 0.749 mm one to give a radius-to-thickness ratio of $R/t = 134.83$. This ratio is in line with the prototype value established above and is considered satisfactory. A summary of specimen dimensions and radius-to-thickness ratios is given in Table 5.1.

Table 5.1: Test Specimen Dimensions

Plate (Bulkhead)	Flange	Radius-to-thickness ratio (Specimen)	Radius-to-thickness ratio (Prototype)
t = 1.130 mm (0.0445 in.)	t = 1.130 mm (0.0445 in.)	R/t = 134.83	R/t = 136
R = 152.4 mm (6 in.)	H = 76.2 mm (3 in.)		

As shown, the width of the flange was chosen to equal half the specimen radius ($H = R/2$). This was driven by the overall goal of the testing. For these tests, the goal was to understand the crushing strength of a typical bulkhead member where the contribution from the flange would be reasonably negligeable. The flange is considered to only provide appropriate boundary conditions. Therefore, we limited our experimental study to the case of narrow flanges ($H < R$).

5.1.2 Test Specimen Fabrication

Both the web and the flange were machined from the 1.130 mm sheet metal. The flange was sheared to dimension and rolled to a radius slightly higher than that of the web. The circular shape of the web was achieved using a lathe. Subsequently, it was cut into two halves on a milling machine with a precision circular saw.

To assemble the two pieces, the Ocean Engineering Welding Laboratory at MIT has suggested the use of electron beam or brazing. The electron beam technique is a fusion joining process in which the workpiece is bombarded with a dense stream of high velocity electrons in an evacuated chamber. Brazing coalescence is produced by using a nonferrous filler metal having a melting point below that of the base metal. The filler metal is distributed between the closely fitted joint surfaces by capillary action.

85

As opposed to the flanged rectangular plates where electron-beam welding was used for reasons explained in Chapter 7, here we preferred the brazing method. It is a simpler and cheaper process which does not require an evacuated chamber. It presents, nevertheless, the drawback of requiring very tight joint fit up tolerances. Otherwise, the filler metal will not flow and gaps will ensue. This will result in a weakened bond. To relax the required tight joint tolerances a nickel braze filler metal was used. However, this process introduced considerable distortions. As described in Appendix D.5 on page 191, out-of-plane initial imperfections of the order of three to four thicknesses were detected.

5.2 Testing Apparatus

Fig. 5.2 shows the experimental set-up which consists of the following equipment

- Instron (Model TTDL) Universal Test Machine (screw driven, 20 kip capacity)
- Test Fixture
- Indenter
- Indenter-to-Load Cell Adapter
- 433/L *Optiplex Dell* desk top personal computer (IBM compatible)
- *National Instruments* Data Acquisition Board and Software Program

5.2.1 Test Fixture

The specimen, shown in Fig. 5.3, is fixed in a test fixture on the crosshead of the Instron machine. The fixture consists of a 16x12x1 in. aluminum base in which a 0.045 in. wide slit was machined. The radial edge of the bulkhead is tight-fitted in the slit. Four side bolts provide, via the flange, the needed clamping force.

5.2.2 Indenter Geometries

The indenters are designed to simulate the case of localized crushing loadings. A simple cylindrical shape was selected for this purpose. Three different indenters with radii of 0.5, 1, and 1.5 in. were fabricated. They were all machined from solid blocks of cold rolled mild steel. Fig. 5.4 shows the indenter of radius 1.5 in.

5.2.3 Indenter-to-Load Cell Adapter

Two indenter-to-load-cell adaptors were used depending on the indenter diameter. Fig. 5.5 shows the connector for the 1 and 2 in. diameter indenters and Fig. 5.6 shows the one for the 3 in. diameter indenter. All components were made from mild steel.

In operation, the adapter is attached directly to the load cell located at the top of the Instron machine. The indenter is attached to the bottom of the adapter. It was then driven into the specimen in a downward motion and the in-plane force was measured.

5.2.4 Instrumentation

The Instron test machine 20,000 lb capacity load cell transducer, provides a voltage signal that is converted to a force measurement. The signal passes through a filter installed in the test machine. The load cell is integrated with the Instron test machine. It has a self-contained power source and the output is filtered to prevent signal contamination by ambient and power noises related to the machine operation. The output signal ranges from 0 to 4 Volts (twice the set rated capacity). Tests were performed on the Instron transducer to ensure that it is calibrated properly and that the output signal was linear. Appendix D.3 on page 188 contains the specific information on these tests. The Instron output signal composes the force measurements. A *lab-PC+* data acquisition board was chosen as the analog to digital converter. The board is made by *National Instruments* under the brand name of *NI-Daq* which was installed in a 433/L *Optiplex Dell* desk top computer. The associated

Daqware software package was used for data recording and real-time viewing of the recorded values. The principal goal of the data acquisition board was to obtain sound data at sampling rate that was adequate to capture all of the information while avoiding susceptibility to small voltage fluctuations that may erroneously influence the data. See Appendix D.3 on page 188 for more details on the Instron machine operation, data acquisition program, and subsequent data reduction.

5.3 Tests and Results

This section covers the description of the tests conducted and results obtained. Three experiments were run each with a different indenter diameter. In all experiments, the crosshead traveled at a displacement rate of 0.2 inch/minute.

5.3.1 Observations

In all three experiments, despite the fact that the indenter's radii were different, the exact pattern of deformation was observed. Very early in the process, the initial deformation was primarily within a bounded region. The force level raised abruptly and reached a peak value of about 11,000 Newtons in less than 20 seconds. Soon after the peak load, outside of the initial deformed zone, the semi-circular plate underwent small but increasing bending deformation. The load level was observed to drop monotonically while the lateral extent of the bounded region remained constant throughout all three tests.

5.3.2 Results

Three tests were performed with indenter's radii of 0.5, 1, and 1.5 in. respectively.

Test #1:

The indenter of radius 0.5 in. was used for this test. Fig. 5.7 shows the load-displacement graph. The recorded peak load was 10,877 Newtons. At the end of the test after a 14 mm travel, the load level was observed to be about 6,000 Newtons.

Test #2:

The indenter of radius 1 in. was used. Fig. 5.8 shows the load-displacement graph. Peak load was 10,983 Newtons and dropped to about 6,800 Newtons at the end of the travel.

Test #3:

The indenter of radius of 1.5 in. was used. Fig. 5.9 shows the load-displacement graph. As the two previous tests, about the same peak load, 11,130 Newtons, was observed. The end of travel load however, remained higher than that of the earlier tests. It was estimated at about 7,500 Newtons.

Note that the peak load was reached in all the three tests after the same crushing distance of about 1.5 mm.
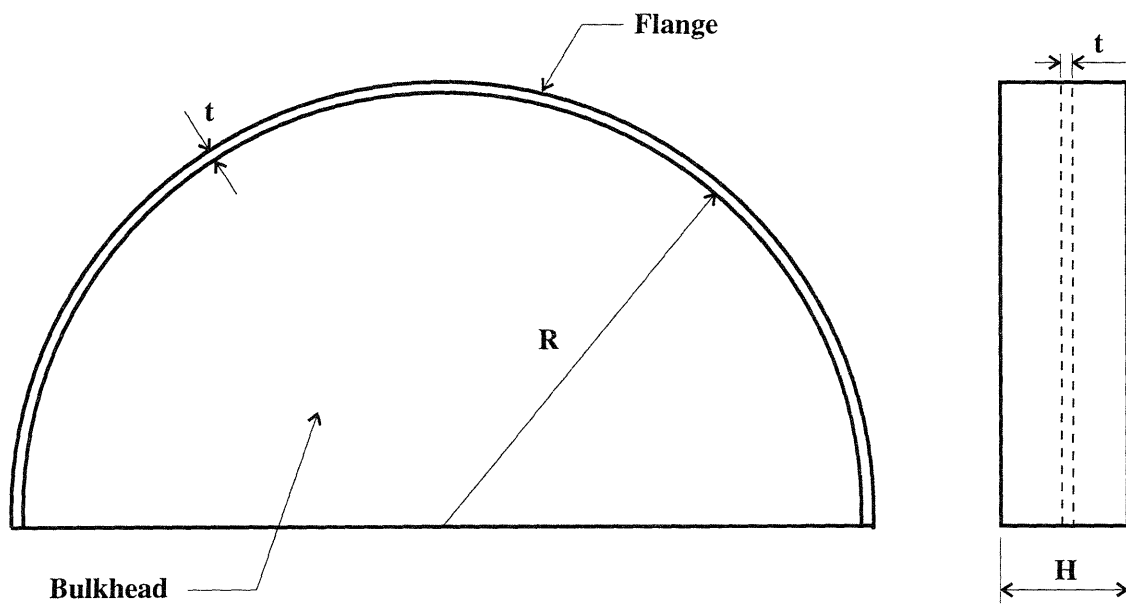
Figure 5.1: Test Specimen Geometry

Input

3

1

4

2

5

6

**20 Kip Instron
(Model TTDL)**
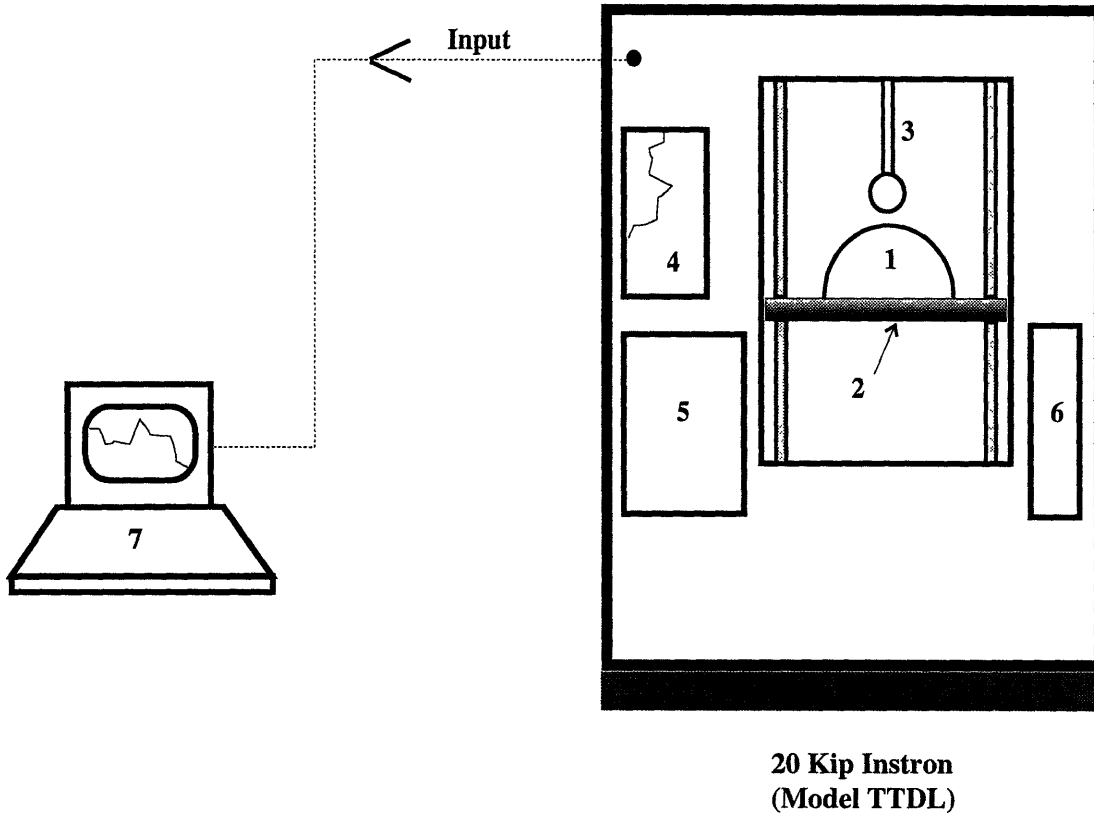
Legend: 1. Specimen
           2. Crosshead
           3. Indenter and Adapter
           4. Built-in Chart Recorder
           5. Machine Control Panel
           6. Crosshead Control Panel
           7. Data Acquisition Computer

7

Figure 5.2: Experimental Set-up
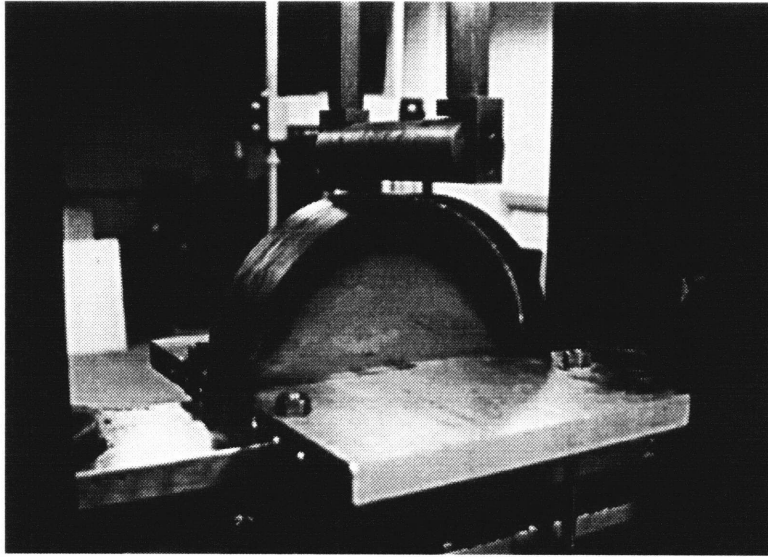
91

Figure 5.3: Test Fixture
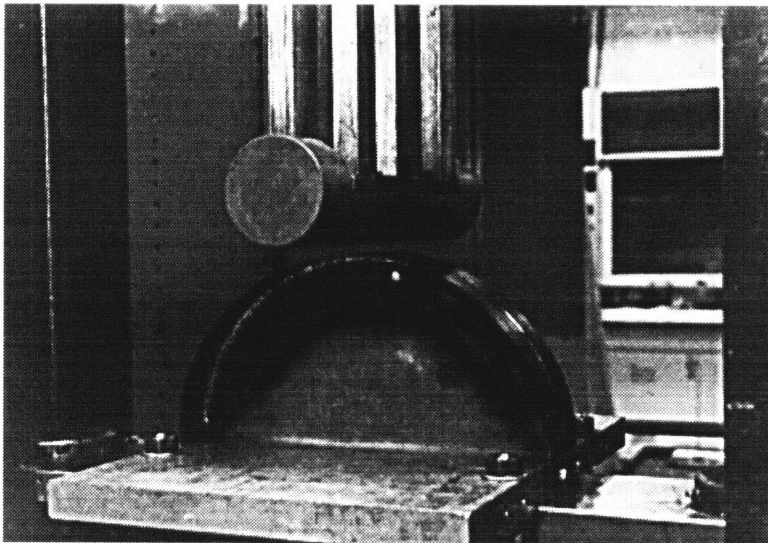
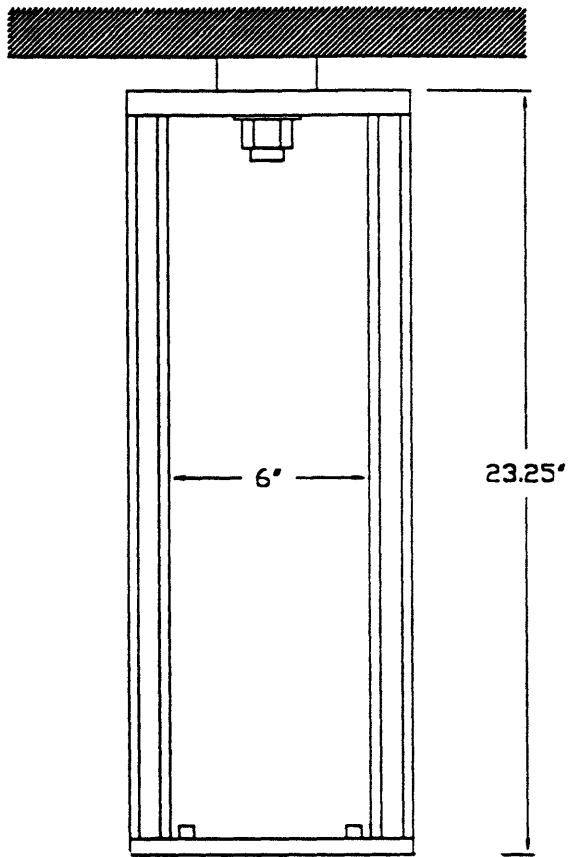**Figure 5.4:** Indenter of Radius 1.5 in.
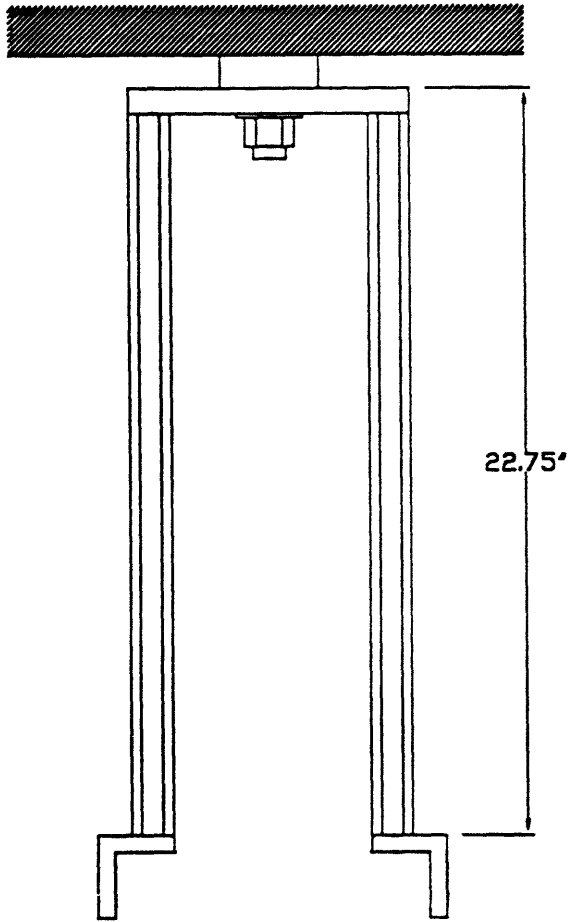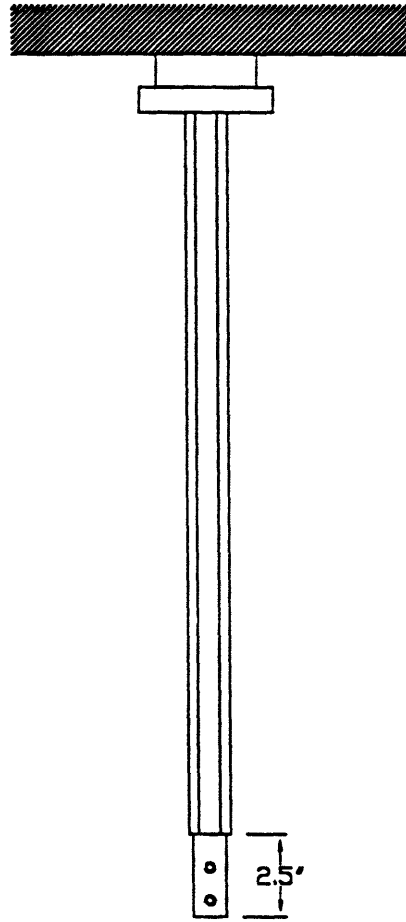
Figure 5.5: Adaptor for Small Indenters

Side View

Front View

A ↓　　　　　　↓ A

23.25'

6'

8.5'

3'
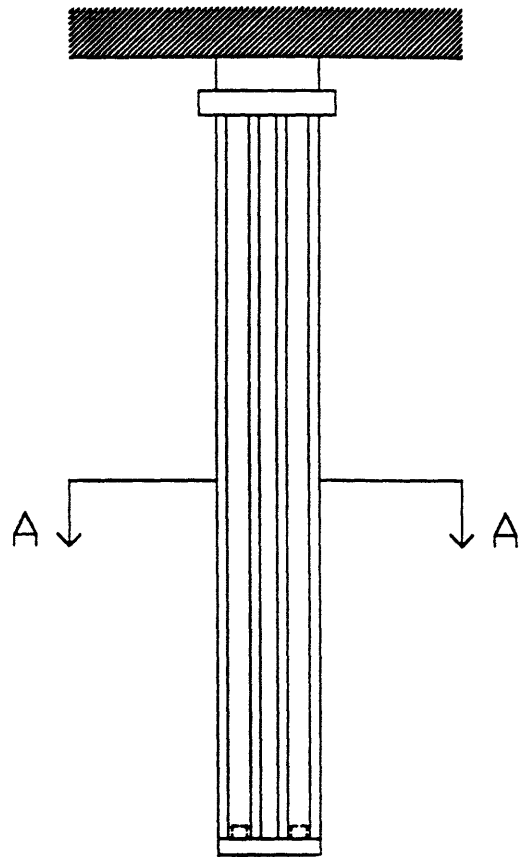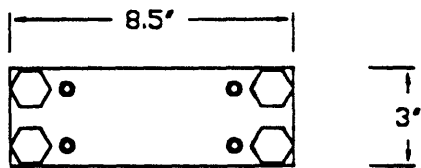
Section A-A

Figure 5.6: Adaptor for Large Indenter
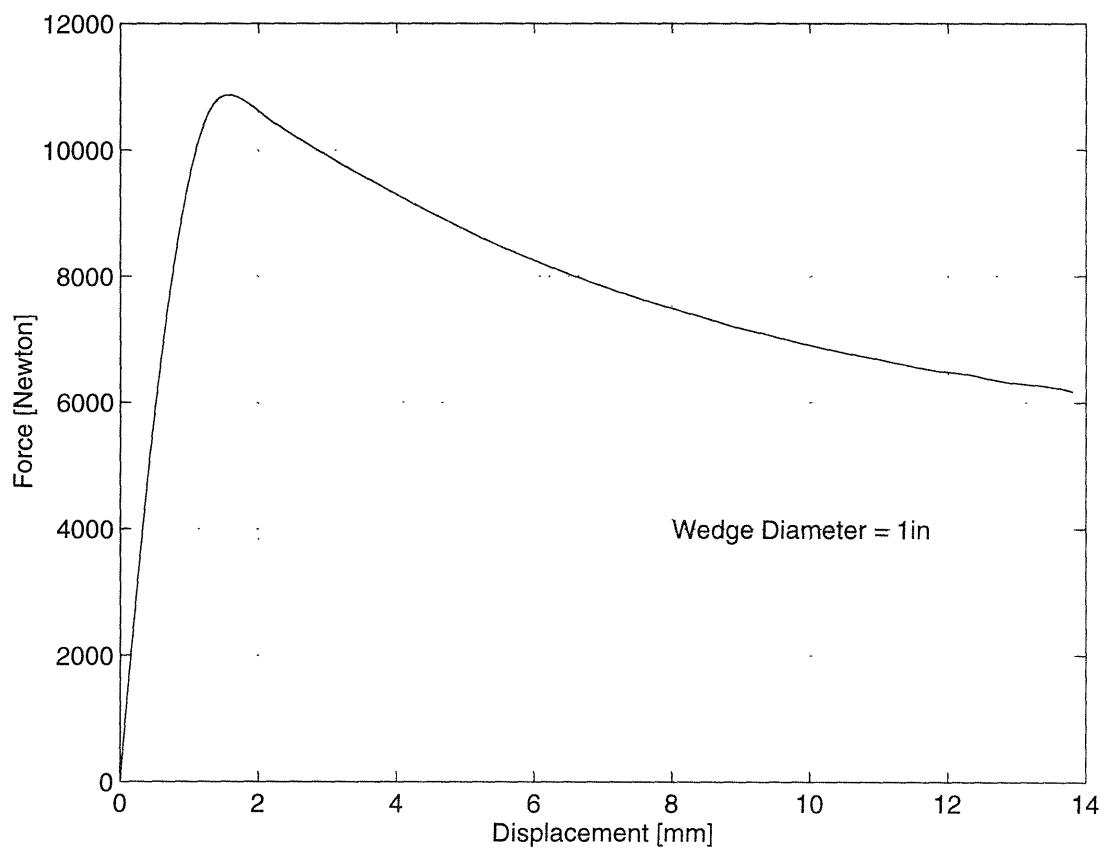
Figure 5.7: Experimental Results for Test #1
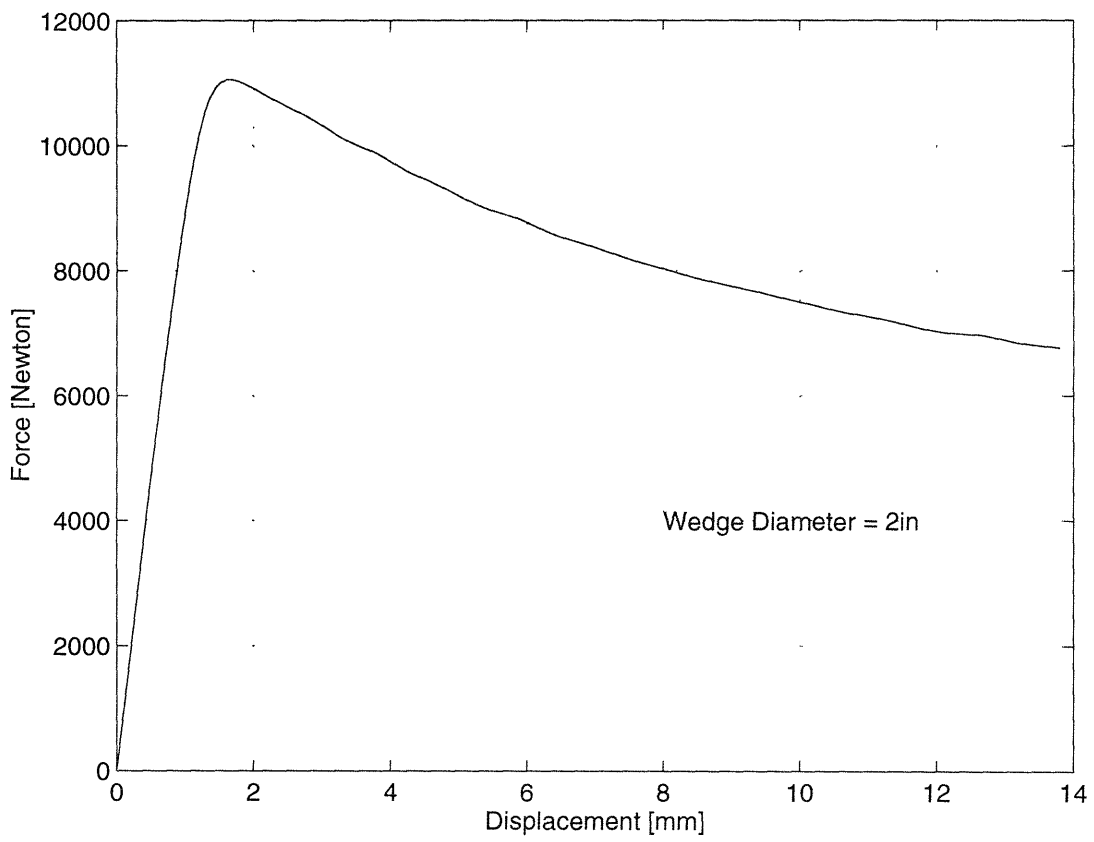
Figure 5.8: Experimental Results for Test #2
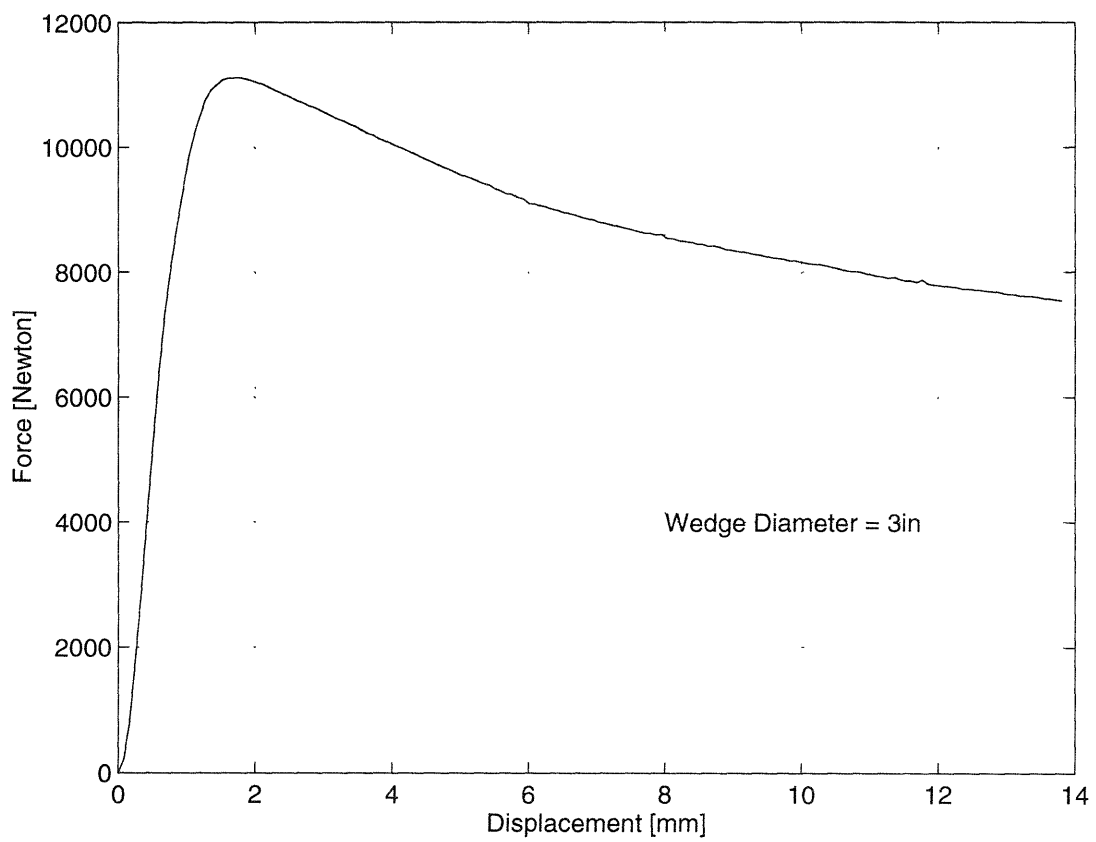
Figure 5.9: Experimental Results for Test #3

Chapter 6

Circular Flanged Plates - Comparison of Experimental Results to Theory

In this chapter, the analytical predictions are compared to the experimental results. Possible causes of discrepancies are commented on and a preliminary discussion of an alternative model is presented.

6.1 Pre-failure Range

Fig. 6.1 shows both the experimental and theoretical pre-failure curves. The theoretical curve is for the case where initial imperfections are three thicknesses and, as derived in Chapter 3, ends at the membrane yield of the material. As is the case in most buckling problems yielding gives the point of maximum load. A slenderness ratio parameter of 0.2315 has been used to determine this point. The experimental curves are for three different radii of indenters. The curves have been truncated at the point where the load is a maximum.

The experimental peak loads corresponding to the indenters with radii 0.5, 1, and 1.5 in. are 10887, 10983, and 11130 Newtons respectively. The predicted theoretical peak load

is 12745 Newtons. It is only overestimating the experimental results by 17%, 16%, and 14.5% respectively. This reveals good correlation with analytical results.

In terms of displacements, the figure reveals what may seem a bad correlation. However, this is misleading because in reality one needs to subtract from the experimental curves the Instron machine deflection. As explained in Appendix D.4 on page 190, the machine does not monitor specimen displacement with time. Therefore, the experimentally recorded indentation depths, which correspond to the Instron screw motion, are not purely the deflections of the specimen. The data is corrupted with the displacements from the flexibility of the Instron cross-head, frame, and indenter adapter.

Once the data are corrected to include the effect of the machine stiffness, the experimental curve is pulled to the left. For example, as detailed in Fig. D.4 on page 190, the corrected experimental displacement at the peak load for the indenter of 2 in radius is 0.075 mm. This value compares favorably with the theoretically predicted displacement of 0.151 mm. It should be pointed out that this comparison is only done to show that the displacements are of comparable magnitude. The differences are smaller than any possible experimental and numerical inaccuracies and could not be considered reliable.

6.2 Post-failure Range

Fig. 6.2 shows the theoretical and experimental curves in the post-failure range. A straight line at the maximum load level is included. In the post-failure phase, we are interested in the portion of the curves to the right of the intersection of this line with the theoretical curve.

The comparison is based on the experimentally observed lateral extent of deformation ($\bar{\zeta}$ = 0.4). Also, the theoretical curve is constructed using the experimental slenderness

ratio parameter 0.2315. In the calculation the effect of the flange was neglected; that is the width of the flange was set equal to zero. The correlation between the theoretical and experimental results is within -5% to +17% depending on the indenter radius.

Figs. 6.3, 6.4, and 6.5 show the global theoretical and experimental load-deflections. As opposed to Fig. 6.2, the elastic theoretical curve is added. Overall, the model with $\bar{\zeta} = 0.4$ provides a good prediction of the observed force levels but does not capture adequately the extent of the deformed zone which was $\bar{\zeta} = 0.8$ at the end of the elastic phase. The theory presented here postulates that the extent of the damaged zone is dictated solely by the value it takes once membrane yielding occurs. The size of the deformed zone was supposed to lock at this specific value. In light of this analysis, we can clearly identify an uncertain transition zone (represented by the horizontal line from the moment when the ultimate strength is reached to the moment it intercepts the theoretical post-failure curve). Certainly, the maximum strength is a good estimate of the force and displacement level but can only be indicative of the damaged zone extent. Indeed, the extent of the deformed zone $\bar{\zeta}$, continues to decrease until when the point of intersection of the horizontal line with the post-failure curve is reached. There is therefore a transition from the point of first yield to the point of full plasticity. This process, which is happening at a constant load is not captured by our model. The tendency of $\bar{\zeta}$ to decrease is clear from Fig. 2.13 on page 46. It is predicted that $\bar{\zeta}$ decreases in the case of no initial imperfections from 0.71 to 0.6 at the onset of yielding of the lower part of the model.

As indicated earlier, the comparison is favorable for a zero flange width. The theoretical loads are overestimated when the full width of the flange is used in the theoretical calculation. A possibility had appeared to be the reduced effective width proposed by von Karman (1932) but no such deformations were observed in the experiments.This reveals a deficiency in our model.

The model at hand makes the flange to be compressed. In reality inextensibility of the flange would not allow this deformation mechanism to take place. However, the derived result is still appropriate to the case of narrow flanges (one order of magnitude less than that the radius of specimen).

6.3 Preliminary Discussion of an Alternative Model

As discussed above, because the inextensibility of the flange is not captured in the base model, an alternative model is developed. This new model is kinematically fully compatible.

6.3.1 Model Geometry

Fig. 6.6 shows the assumed new model geometry. As indicated, the flange is kept inextensible. This imposes the deformation to extend throughout the plate. The experimentally observed curved ridge line 'AOC' (cf. Fig. 2.4 on page 37) is approximated now by three ridge lines 'CD', 'DG', and 'GH'. As indentation progresses, the points 'D' and 'G' move out-of-plane. Relieving tension is shown by the shaded area. Also, the experimentally observed ridge lines 'OD' and 'OE' are now approximated by the lines 'DF' and 'GJ'. The unknown geometric parameter ζ is shown in the figure and represents the horizontal distance between the point of load application 'E' and point 'C' (or point 'H' by symmetry).

In order to capture the experimentally observed deformation pattern better, a slightly modified model can be used and is shown in Fig. 6.7. This model brings the ridge lines 'DF' and 'GJ' to intersect at a point closer to the symmetry line. This geometry is closer to reality. The models are analytically similar in form. In the analysis one need only to adjust the parameter λ (ζ) accordingly for each model.

6.3.2 Pre-buckling Path

In what follows, from a postulated displacement field the pre-buckling equilibrium path is determined. The same approach as in Chapter 2 is used. Fig. 6.8 shows the postulated in-plane displacement field. The maximum in-plane displacement is represented by u_0 and the maximum out-of-plane displacement by w_0. The displacement u_0 occurs at the point of application of the compressive load P. All points on the line 'AD' are assumed to displace the same amount, u_1. One important feature of this alternative model is that now the point 'C' is not stationary. Indeed, point 'C' has to move up a distance u_2 and left a distance v_2 in order to keep the total length 'FCE' constant. In the analysis the displacements u_2 and v_2 are not considered unknown parameters. They are determined geometrically, from the inextensibility condition of the flange. Fig. 6.9 illustrates the form taken by the out-of-plane displacement field $w(x, y)$. Maximum out-of-plane displacement w_1 occurs along the line 'AD'.

A similar analysis as in Chapter 2 was conducted on this model in order to determine the value of $\bar{\zeta}$ for which the stiffness is a minimum in the in-plane deformation mode. As shown in Fig. 6.10, the stiffness is minimum when $\bar{\zeta} = 0$. This means that all the in-plane deformation is localized at a single point under the load. We are faced with a singularity situation. The plate will yield in compression very quickly under low loads. This alternative model predicts plastic buckling mode of deformation rather than elastic buckling as predicted previously. A limit analysis shows that this happens because the structure avoids infinite shear by letting the in-plane displacement u_1 be zero in the minimization process.

In order to determine what governs the value of $\bar{\zeta}$, a new deformation mechanism for the early stages of the crushing process needs to be developed. One approach is to estimate the rate of membrane work and seek a minimum for $\bar{\zeta}$. Another approach is to

include the effect of finite size of the indenters. Indeed, looking at the experimental data, an estimate of the extent of the in-plane plastic zone is estimated to 47 mm for a maximum peak load of 11000 Newtons. This value is comparable to the extent of the damaged zone observed in the specimen $\zeta = 61mm$. This suggests that the analytical approximation of the loading by a knife-edge is not appropriate for this new model.
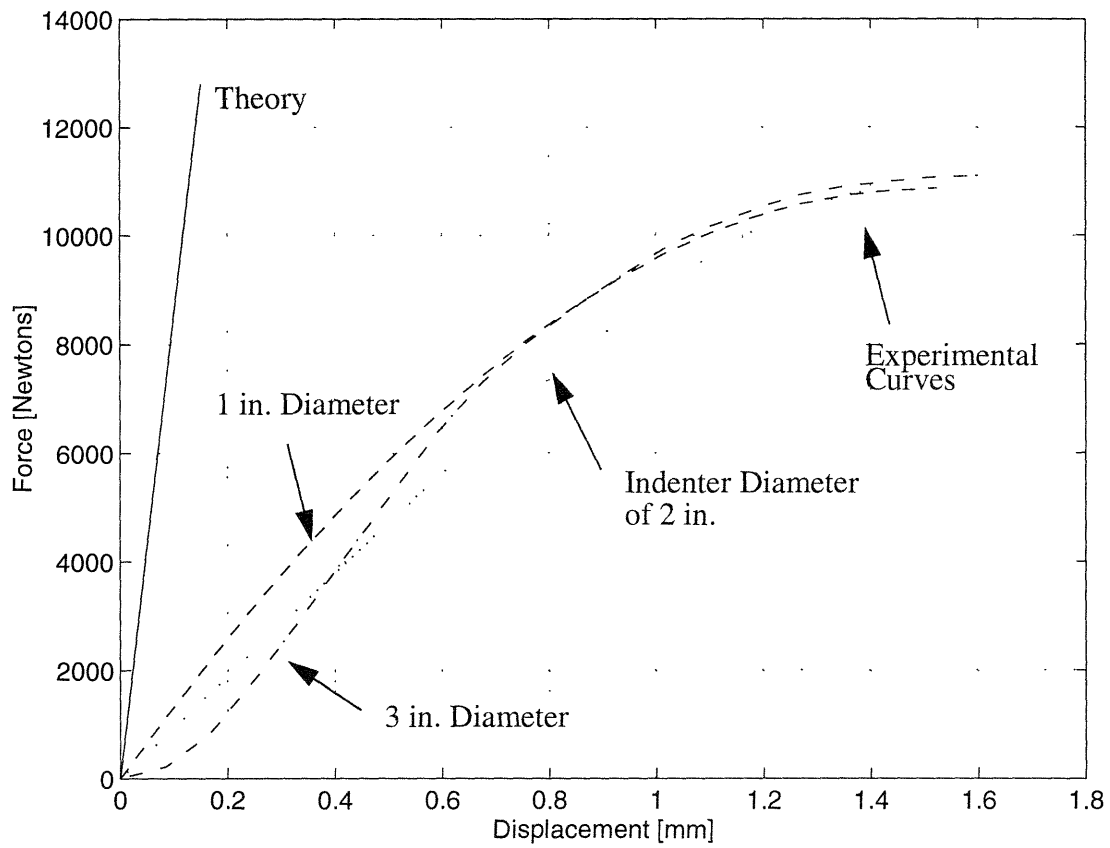
Figure 6.1: Experimental and Theoretical Pre-failure Curves
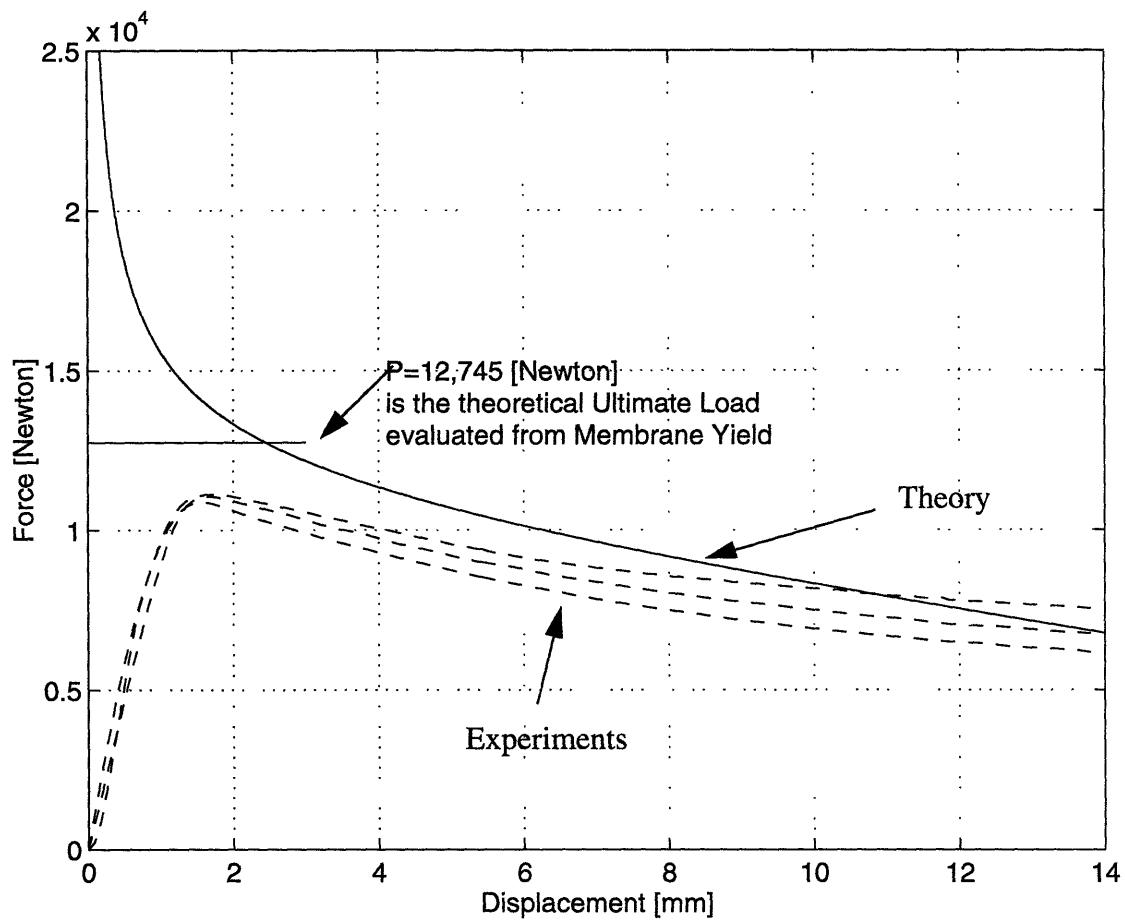
Figure 6.2: Experimental and Theoretical Post-failure Curves
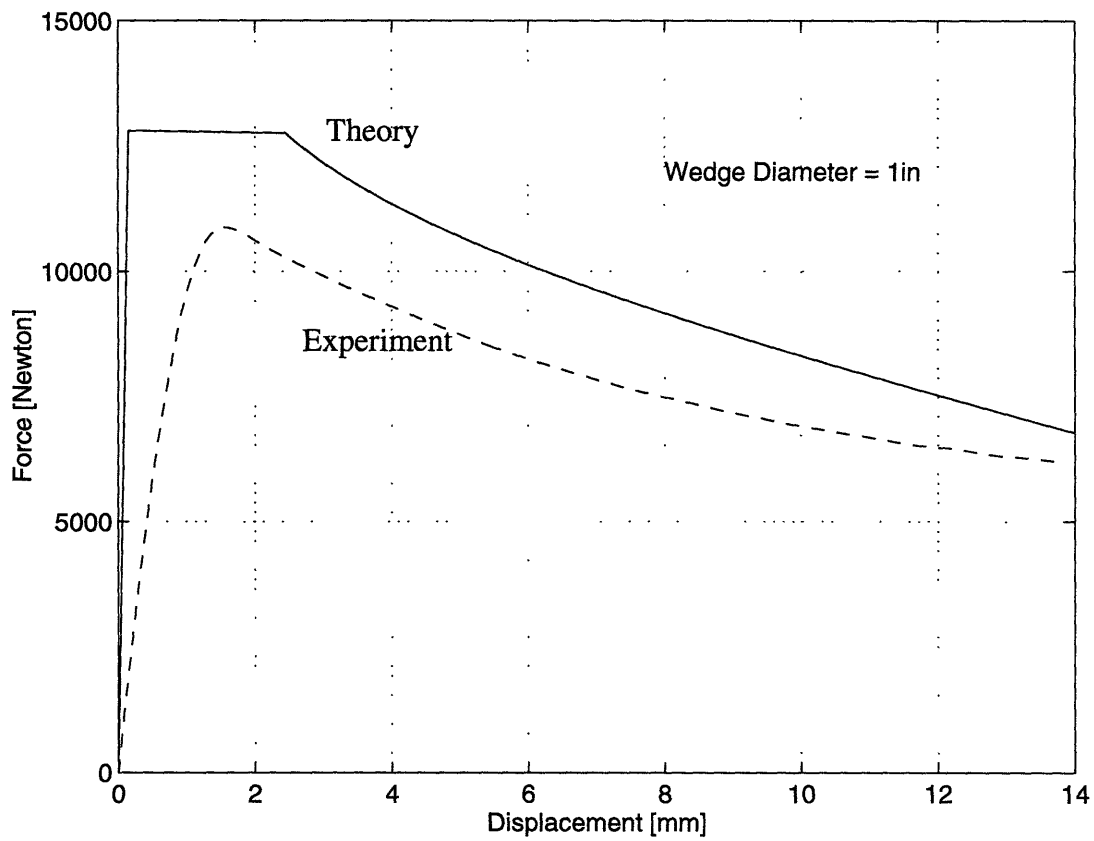
Figure 6.3: Global theoretical and Experimental Load-deflections for Test #1
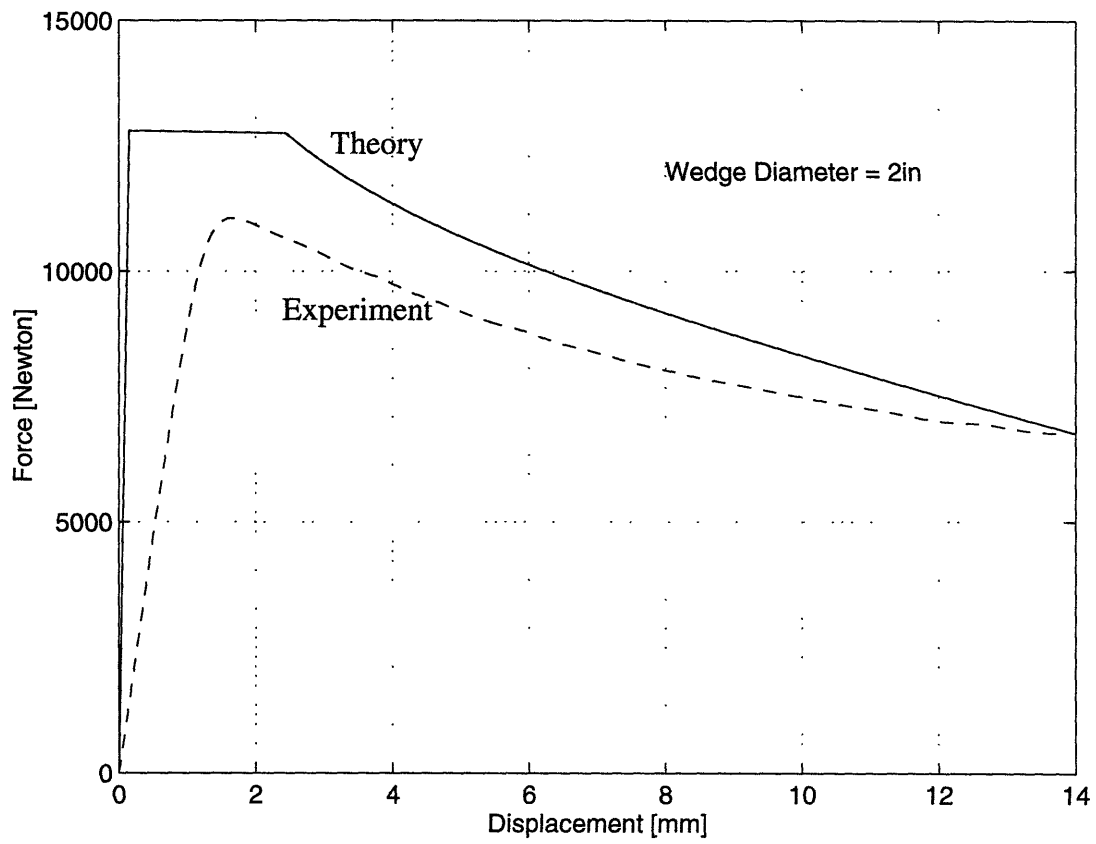
Figure 6.4: Global Theoretical and Experimental Load-deflection for Test #2
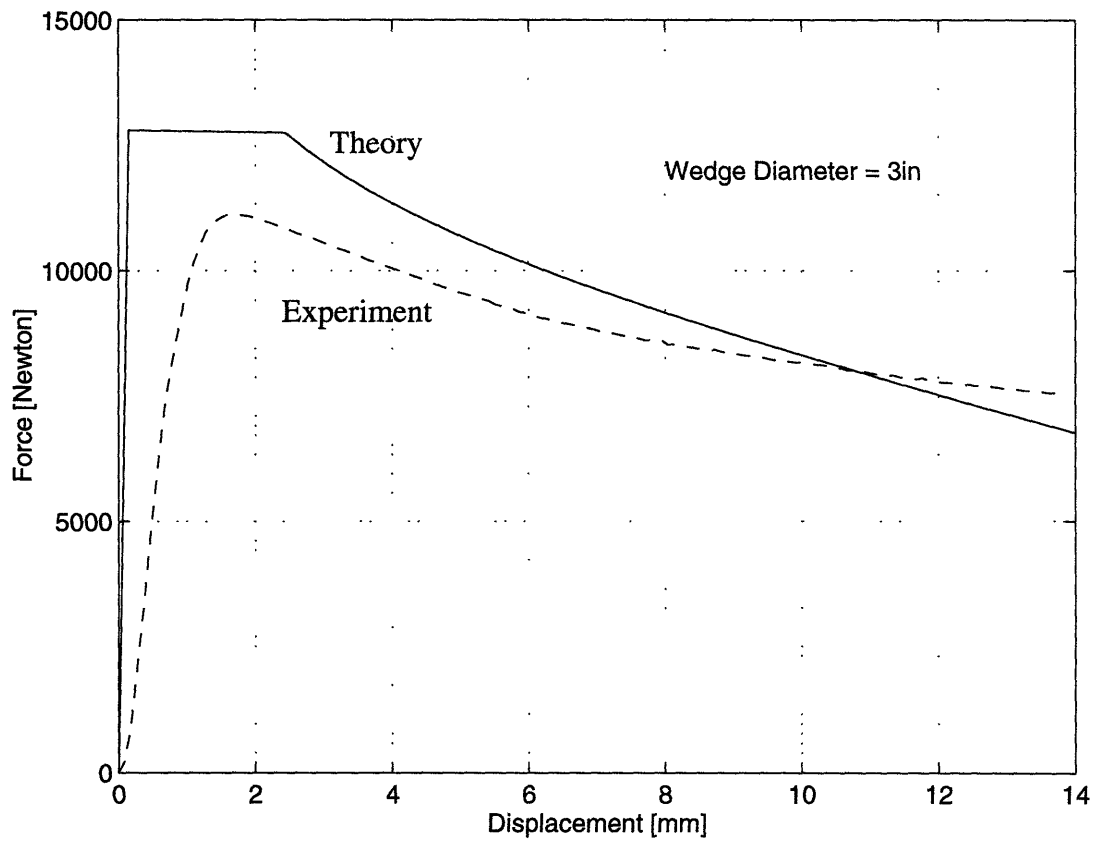
Figure 6.5: Global Theoretical and Experimental Load-deflection for Test #3
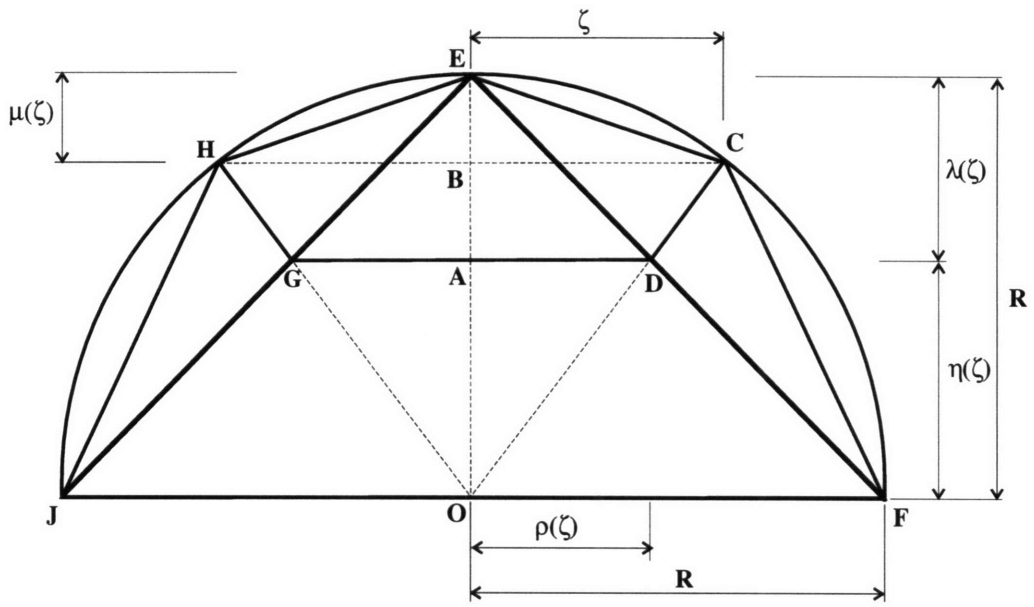
(a) Before Deformation
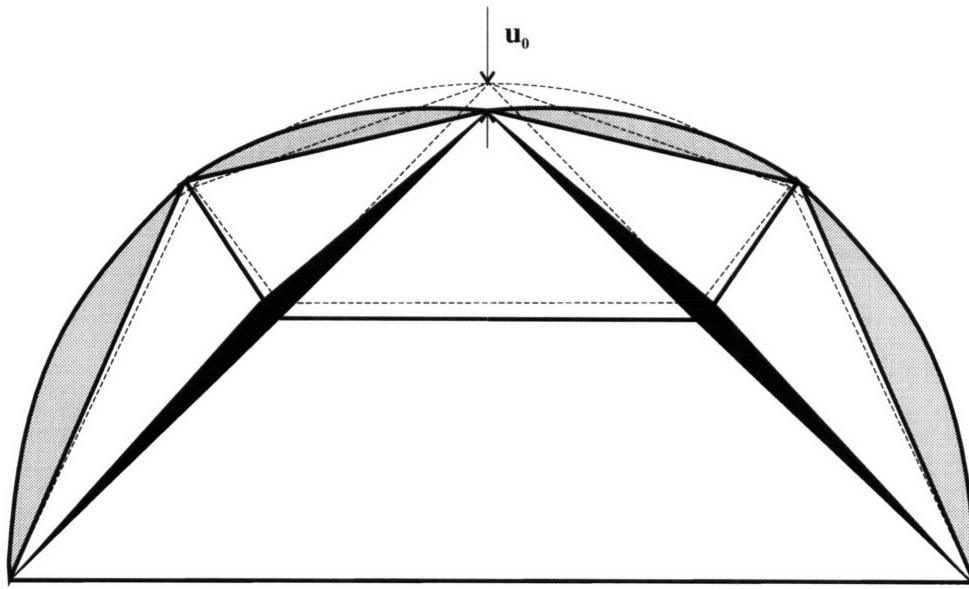
Relieving tension due to out-of-plane displacements

Remains in-plane

(b) After Deformation

Figure 6.6: Alternative Model Geometry
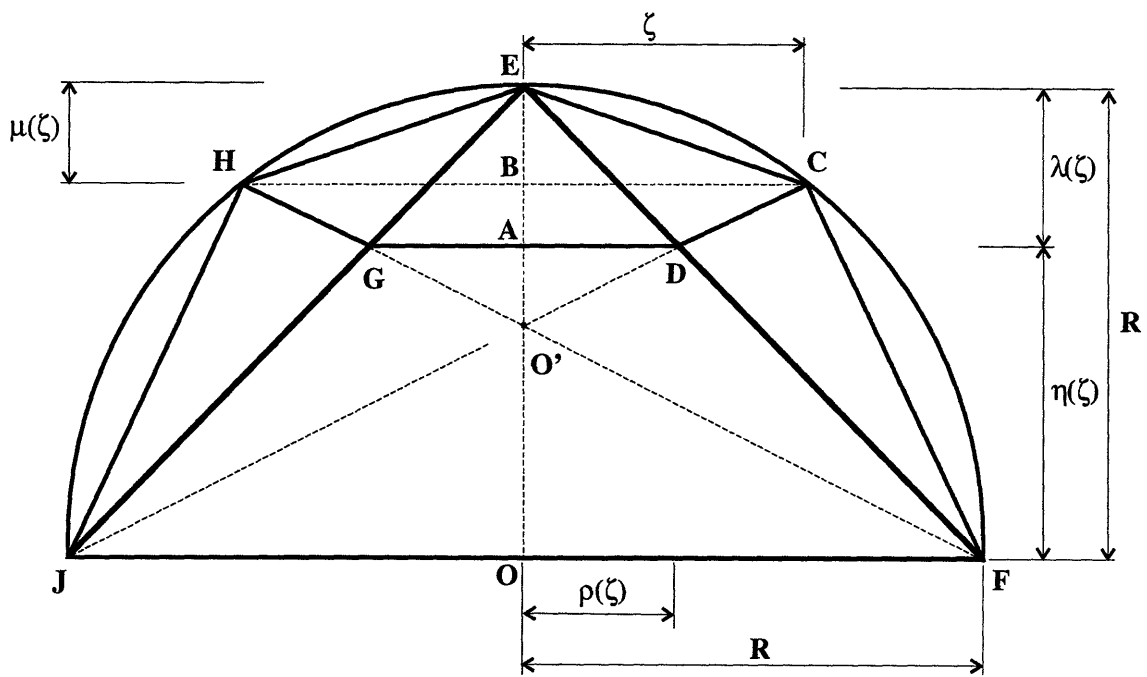
Figure 6.7: Modified Model
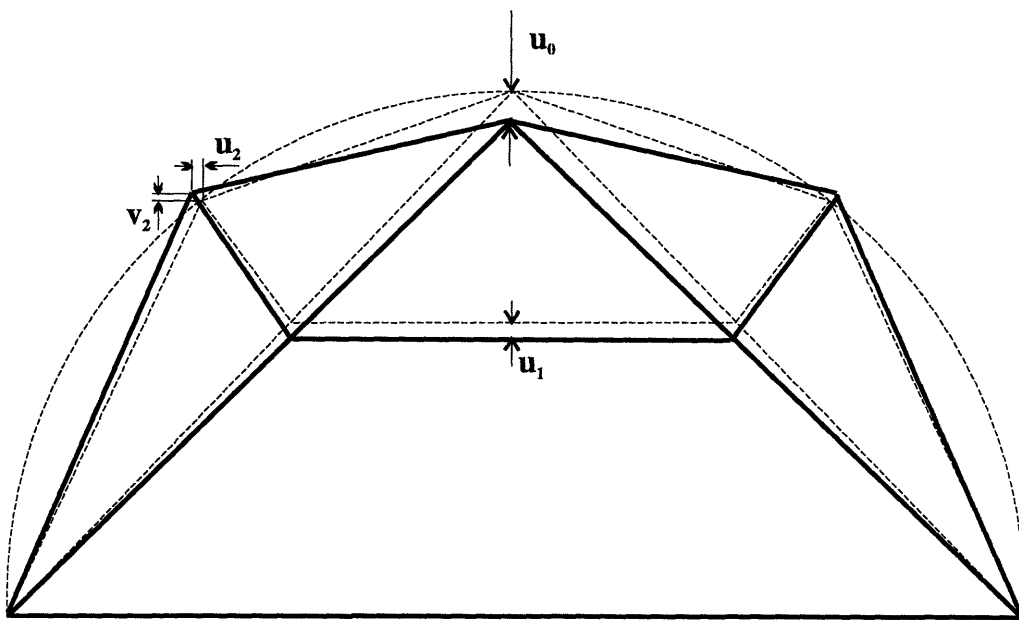
Figure 6.8: In-plane Displacement Field
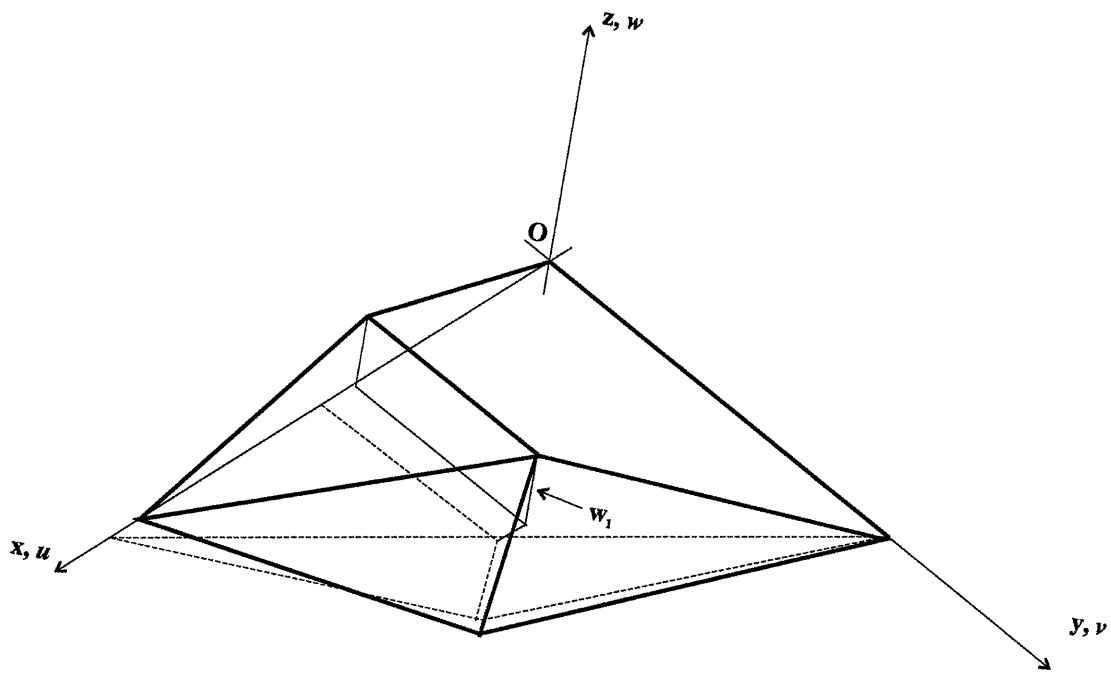
Figure 6.9: Out-of-plane Displacement Field
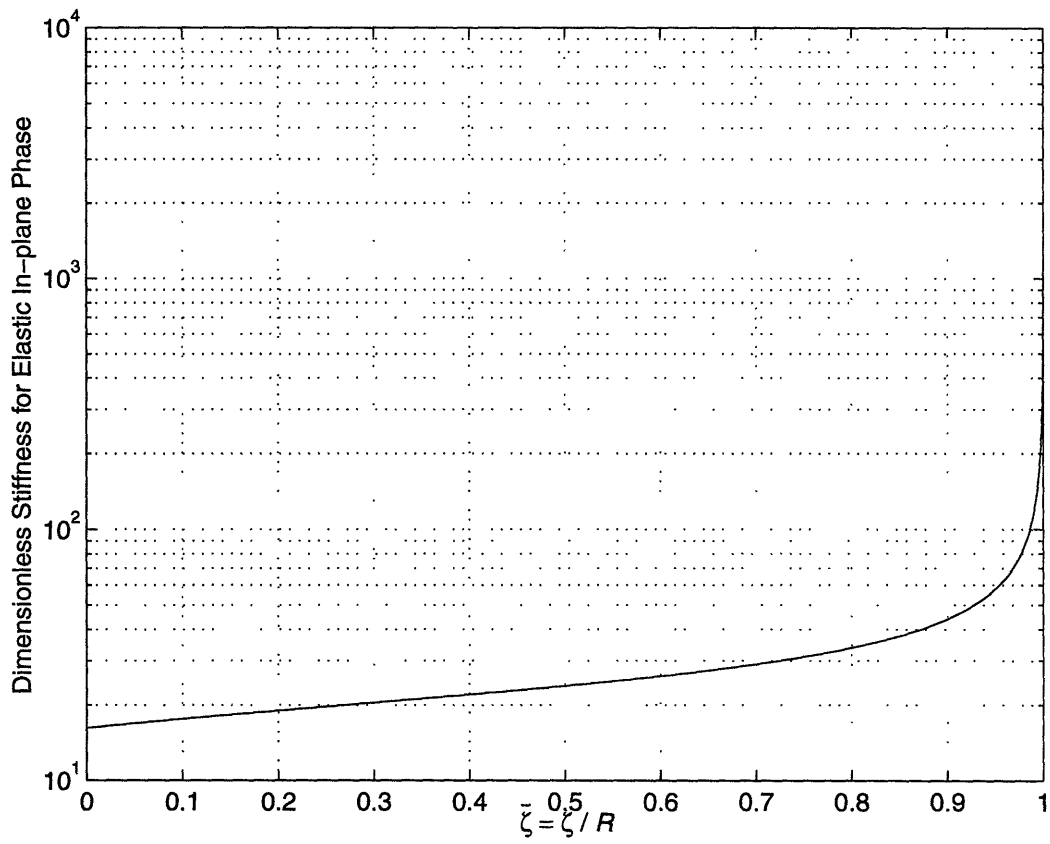
Figure 6.10: Dimensionless Elastic In-plane stiffness vs. Extent of Damage

Chapter 7

Rectangular Flanged Plates - An Experimental Investigation

Indentation tests of flanged rectangular plates are described in this chapter. The experiment was designed to simulate the response of the simplified model of constant girder depths developed by Choi *et al.* (1994).

The test equipment is identical to the one used for the flanged semi-circular plates and described in Chapter 5. In what follows, we restrict the description to the geometries of the specimen and indenters, and present the test results.

7.1 Specimen Geometry

Flanged rectangular plates (called here T-Stiffeners) were manufactured to verify the analytical model for crushing of web girders due to localized lateral loading. The analytical model was developed by Choi *et al.* (1994). The results of these tests were also used in the comparative study with numerical solutions performed by Goksoyr (1994).

The T-stiffeners are uniform thickness T-beams made of ASTM A366 steel with the height of the web equal to the width of the flange. The web and the flange were welded

using Electron Beam Welding (EBW). Fig. 7.1 shows the specimen along with its dimensions. Note that the effective length of he specimens is only L = 4H, not the total available L=6H length. The extra length H on each end of the structural unit is needed in achieving the required boundary conditions as explained in Section 7.3. Justification of the choice of EBW process for welding and selection of the value of B are explained in Yahiaoui *et al.* (1994).

7.2 Indenters

A very simple flat indenter was designed and fabricated out of aluminum stock for the T-stiffener crushing tests. The geometry is identical to that used in the numerical analysis performed by Goksoyr (1994) and is shown in Fig. 7.2. To simulate a more localized loading, a narrow indenter with a circular tip was also manufactured out of steel.

7.3 Tests and Results

In light of the observations made from the numerical analysis of the crushing of web girders studied by Goksoyr (1994), it was decided to run experiments simulating the local denting mode only. To analyze how this mode responds to increasing width of the wedge, two different wedges were used: one flat wide wedge identical to that used in the numerical analysis, and one narrow wedge with a circular tip, to simulate a more localized loading. Three experiments using the wide wedge and one experiment using the narrow wedge were conducted. Fig. 7.3 shows the experimental set-up used to simulate the local denting mode. The test specimens are taken to be the same in both the experimental and numerical approaches as discussed in Goksoyr (1994). The boundary conditions are also essentially the same as those used in the numerical analysis. The two ends of the structural unit and

the lower edge of the web girder are clamped. the flange is free with respect to in-plane movements along the longitudinal edges. Fig. 7.4 shows the apparatus used for conducting the crushing tests. The T-stiffener is clamped by the pressure provided by the vise via two fixture blocks. In all four crushing experiments, the cross-head speed was set to 0.2 inches per minute.

Test #1:

The wide flat indenter, was used for this test. We stopped the experiment when the indentation reached 28 mm to avoid contact between the deformed web and the flange because the numerical solution is only valid up to the point of contact (Goksoyr, 1994). Fig. 7.5 shows the force-displacement graph.

Test #2:

The narrow indenter, was used for this test. The same procedure as for test #1 was followed. Fig. 7.6 shows the force-displacement graph.

Tests#3 & #4:

As described in Yahiaoui *et al.* (1994) and Goksoyr (1994), the first two experiments showed that the lower edge of the web girder underwent global bending and a longitudinal displacement of the flange was observed. This was a deviation from the intended boundary conditions. In order to eliminate this problem, the testing fixture was modified. Fig. 7.7 shows the original and modified configurations. The steel step restrained the bottom of the web from global bending. The three pins, acting as draw beads, and the cap added on top prevented any lateral movement of the ends of the flange. This design modification

116

was proven to be successful after examination of deformed specimens of test #3 and #4. Note that these tests were a repeat of test #1, except that the tests were run longer, allowing contact of the deformed web with the flange. Fig. 7.8 documents test #3 while Fig. 7.9 documents test #4. Figs. 7.10, 7.11, and 7.12 show photographs of crushed specimen for tests # 1, 2 and 3 respectively.

These cleaner results provide a closer correlation to the numerical and analytical solutions as described by Choi *et al.* (1994). A comparison of the results, showed that the analytical model overestimates experimental loads by only 5-15%.
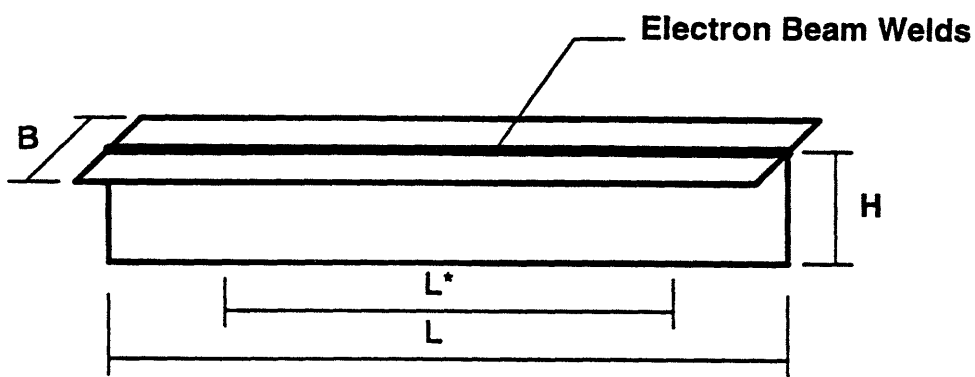
B (Web Height) = H (Flange width) = 1.64" (41.7 mm)

L (Total Length) = 6H = 9.84" (250.2 mm)

L* (effective) = 4H = 6.56" (166.8 mm)

t (thickness) = 0.0295" (0.749 mm)

Figure 7.1: Flanged Rectangular Plate Specimen
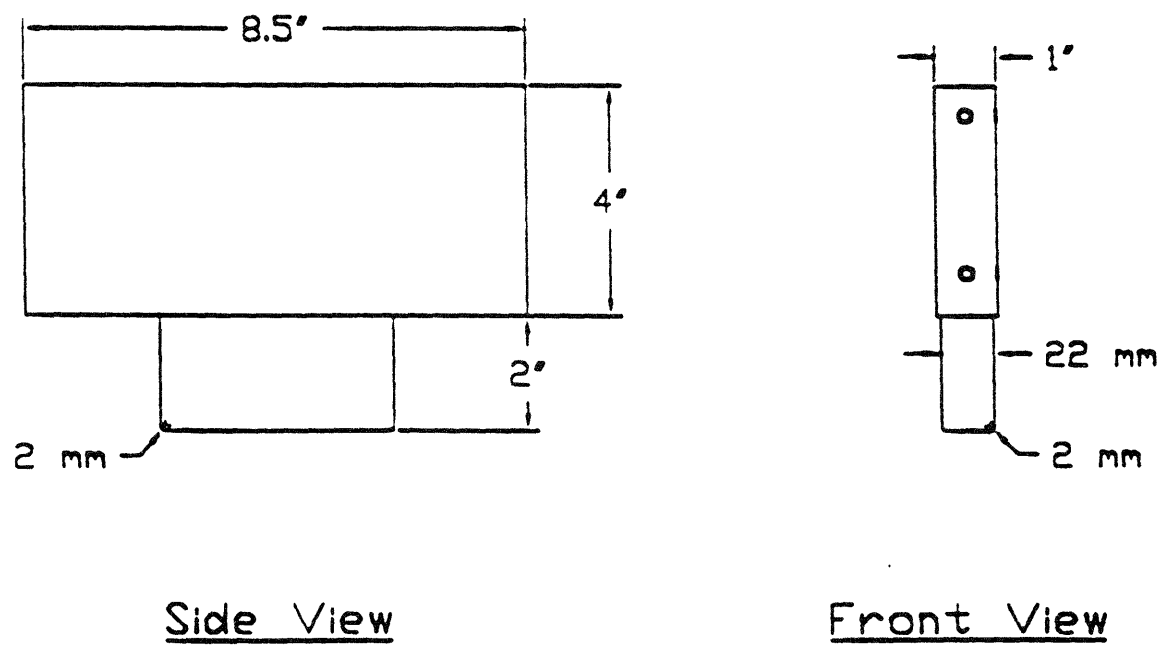
Figure 7.2: Indenter Geometry
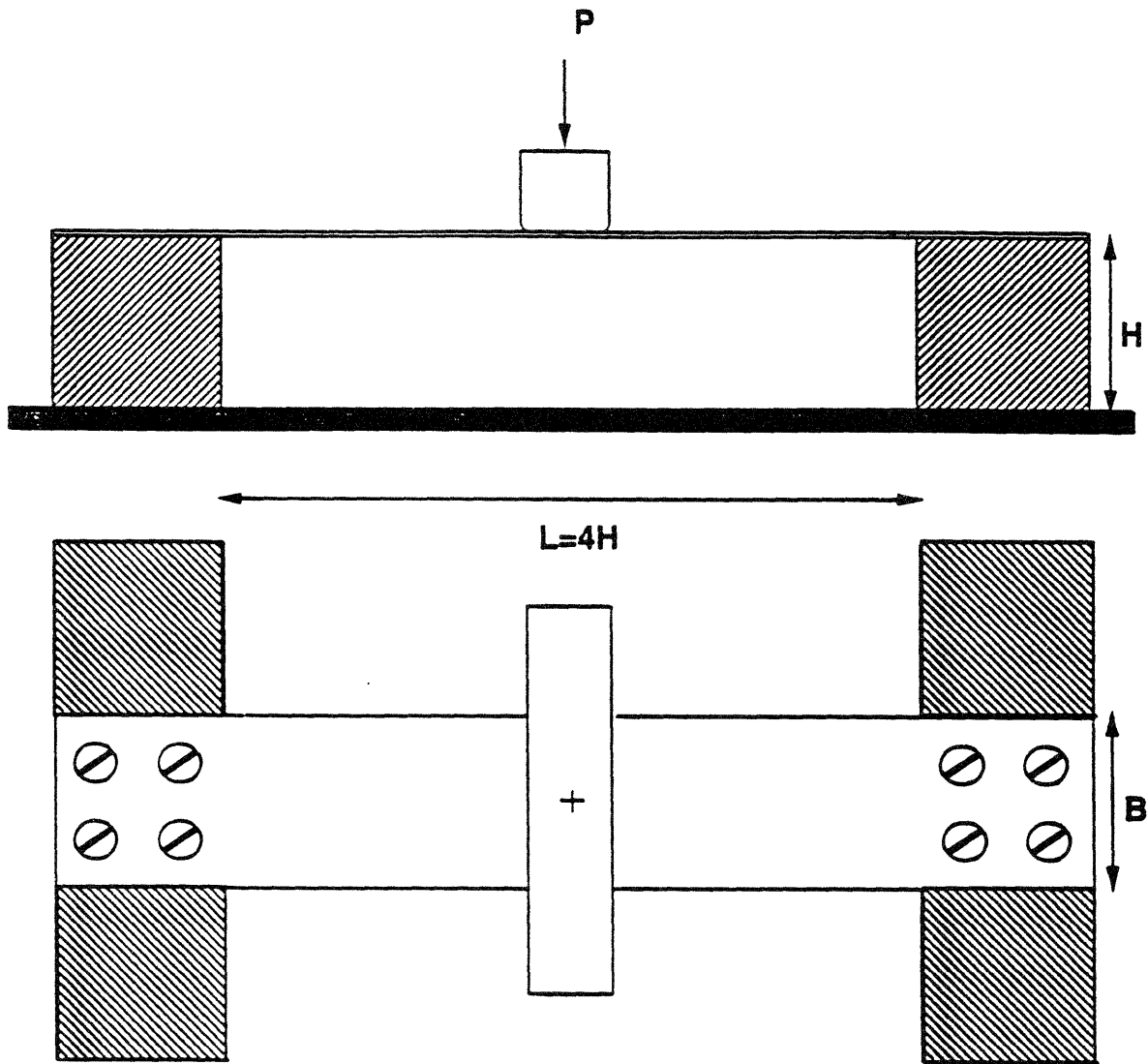
Figure 7.3: Experimental Set-up
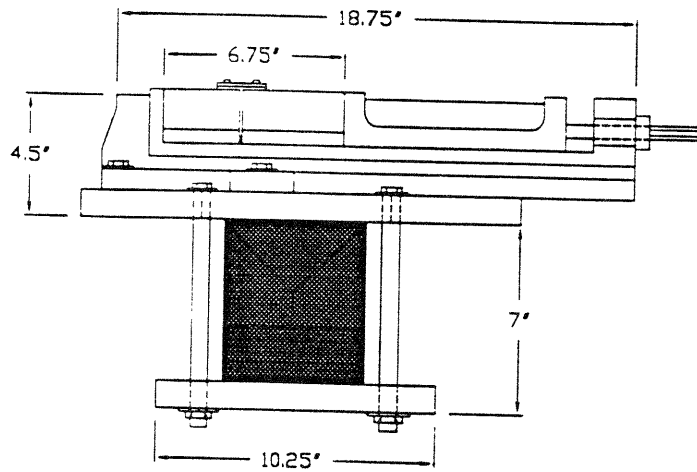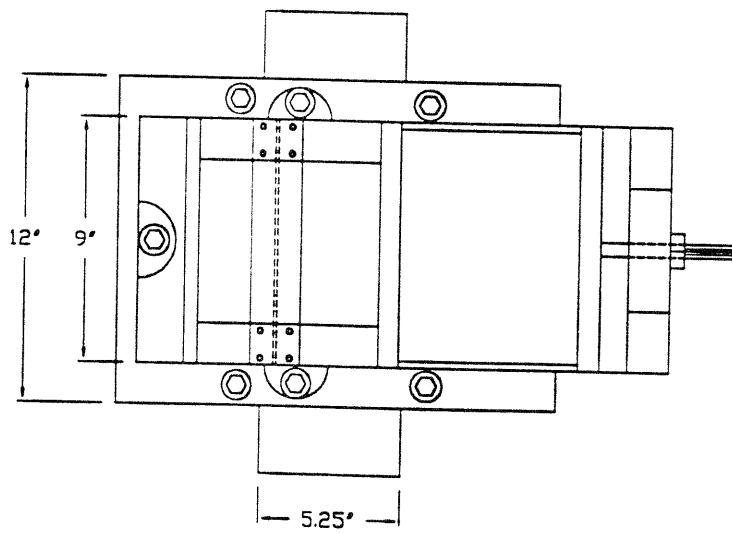
Figure 7.4: Experimental Apparatus
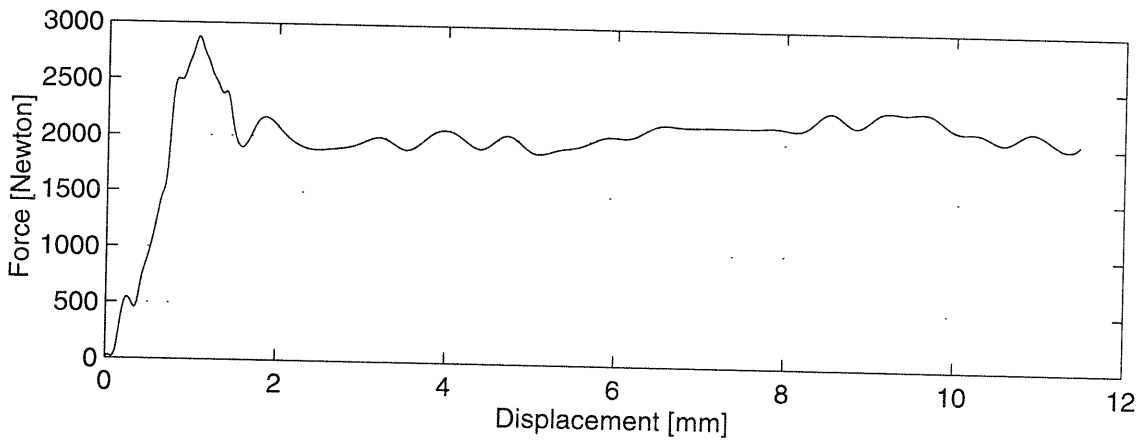
Figure 7.5: Experimental Results for Test #1
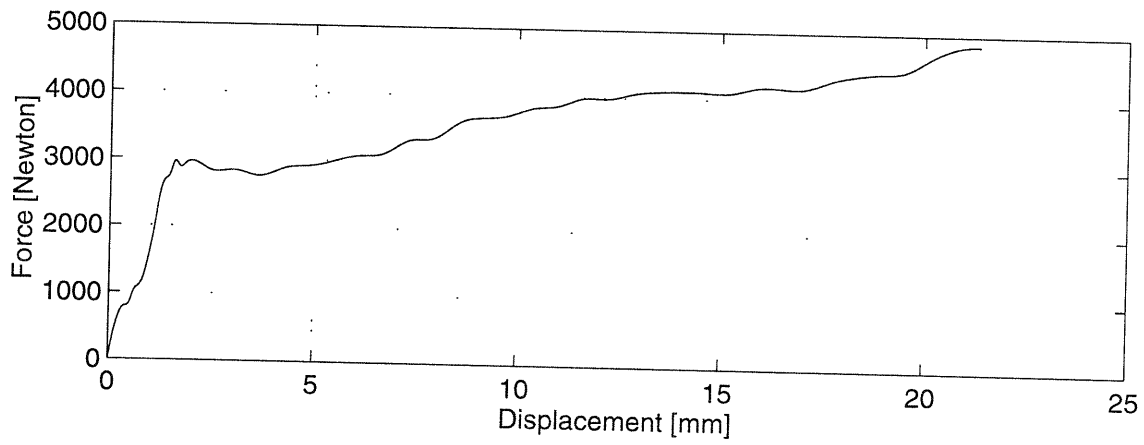
Figure 7.6: Experimental Results for Test #2
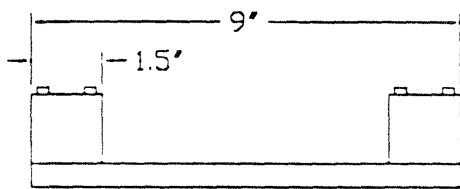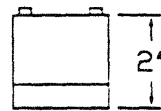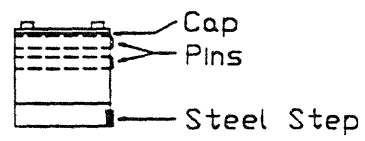
Figure 7.7: Original and Modified Testing Fixture
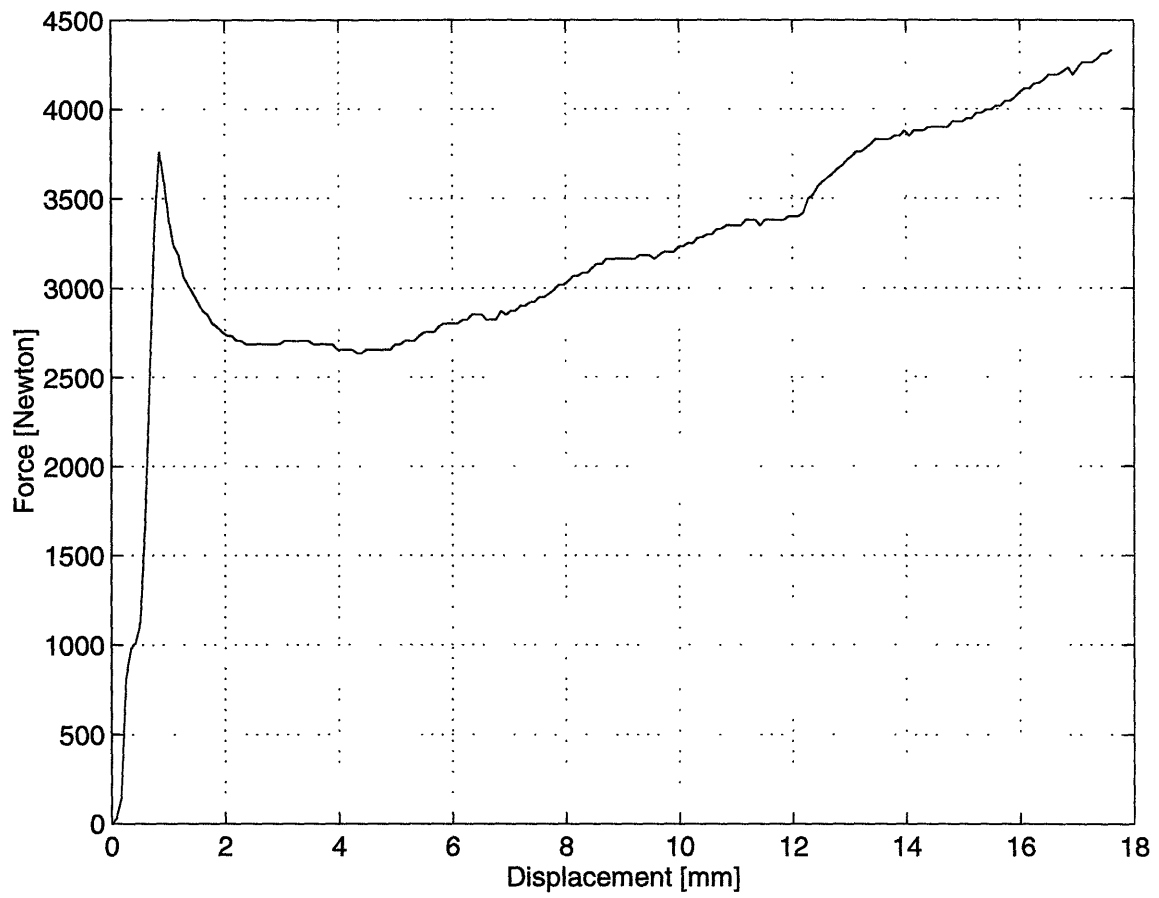
Figure 7.8: Experimental Results for Test #3
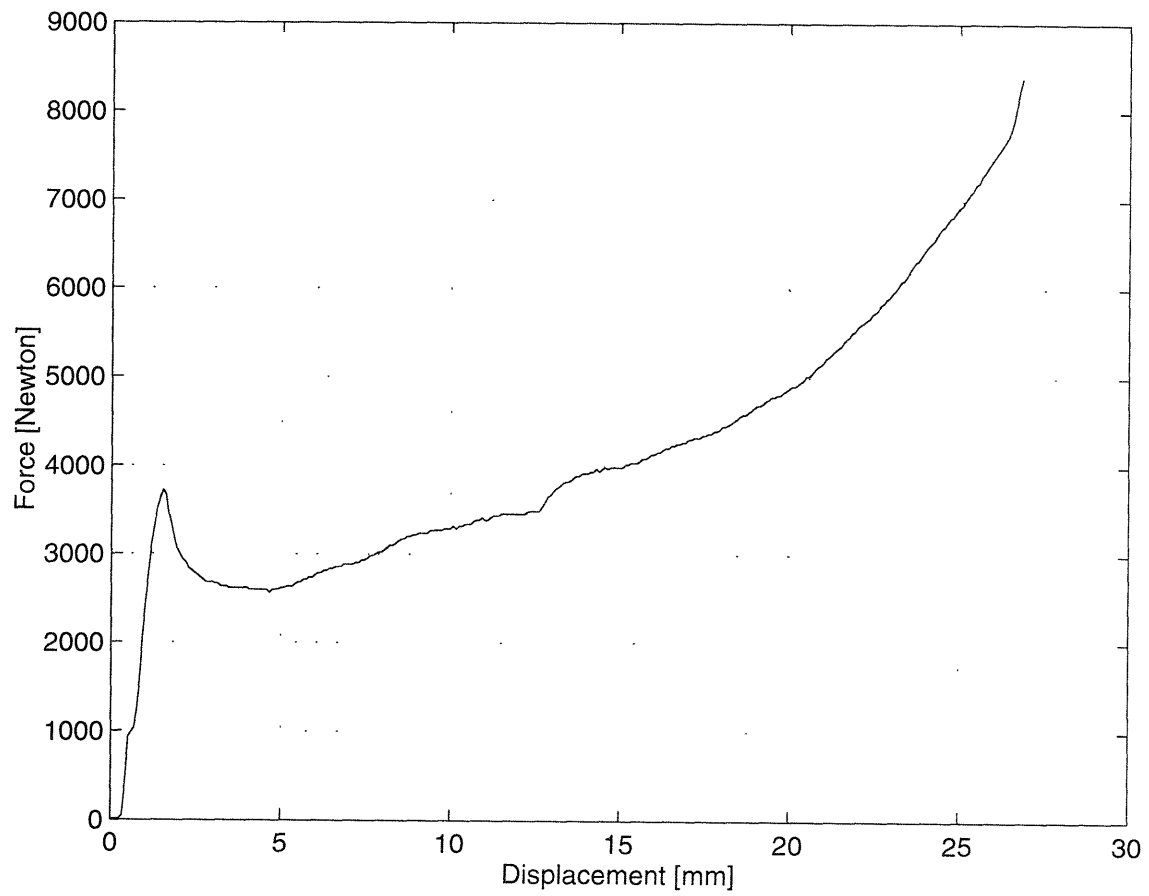
Figure 7.9: Experimental Results for Test #4
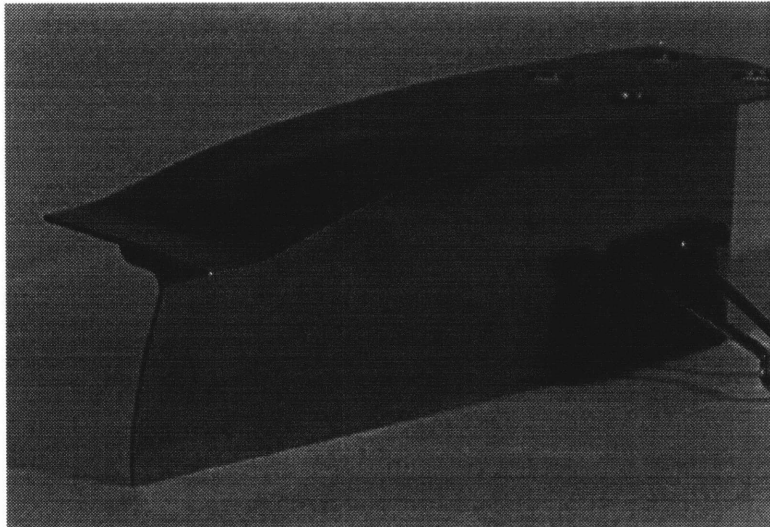
Figure 7.10: Crushed Specimen of Test #1
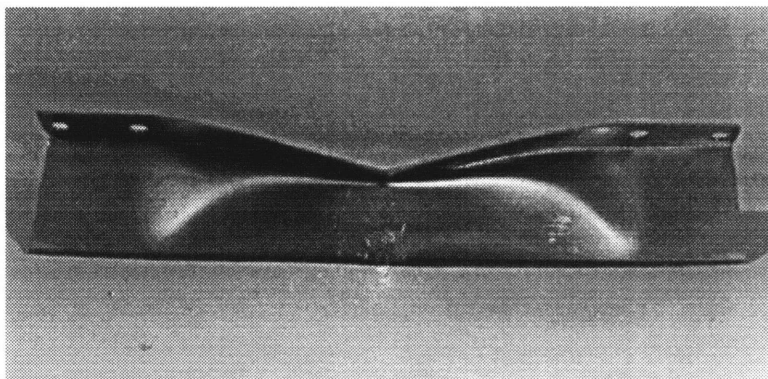
Figure 7.11: Crushed Specimen of Test #2
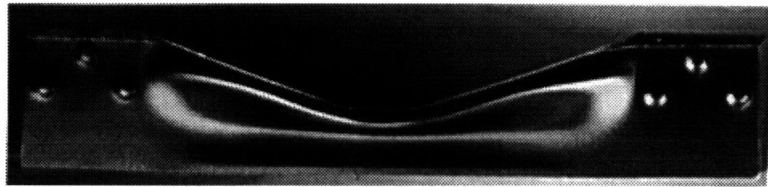
Figure 7.12: Crushed Specimen of Test #3

Chapter 8

Discussion and Conclusions

Understanding the overall ability of shell structures, such as ships, submarines, and aircraft, to withstand local damage during accidental loads is an important problem. Part of this problem is to assess the crushing behavior of flanged semi-circular and rectangular plates under localized in-plane loadings. The flanged rectangular plate model characterizes the behavior of the bulkheads in the flat bottom region of both conventional and unidirectionally stiffened double hull ships during grounding accidents. The flanged circular plate model describes the behavior in the bilge area and provides estimates of the strength of submarine bulkheads in collisions or aircraft fuselages subject to crash landings. The derived solutions constitute an evolutionary step in understanding this problem.

Analytical solutions are presented for the response of the structure from the in-plane elastic to the post-failure (plastic folding). Energy methods are used to analyze the elastic pre- and post-buckling response of the flanged plates. Ultimate strength is calculated using the membrane yield criterion. Limit analysis, applied incrementally up to large displacements and rotations, is employed in the post-failure range (in the sense of post-peak load).

Much understanding and insight can be gained from such analytical work. By identifying different terms of work rates, the relative significance of the various terms can be established. The two major modes of energy absorption have been found to be bending and membrane resistance. Also, the sequence of the deformation process is better understood than with numerical methods alone.

The analytical solutions were then compared to the experimental results conducted on small-scale specimens of geometries in proportions comparable to those of the ship bilge area. The theoretical results are shown to give good estimates of the ultimate strength or peak-load (at the onset of membrane yield). That is, they are only about 15% above experimental results.

A comparison of the crushing loads in the post-failure phase was also made. For the case of narrow flanges when the extent of the deformed zone is measured from the wide flange tests, the correlation is within -5% to +17% depending on the indenter radius. However, when the extent of the deformed zone is used from the peak load calculations the correlation is not adequate. Loads are overestimated in this case by more than 50%.

It can be concluded that the present computational model captures some of the features of the structural response. However, it fails to capture the tendency of the extent of the damaged zone to decrease between the end of the pre-failure and beginning of post-failure phases before locking (mode shape becoming constant). Indeed, the theory postulates that the extent of the damaged zone in the post-failure phase is solely dictated by the membrane yield analysis (end of pre-failure phase). In light of this work, this assumption needs to be revisited in any subsequent work.

As stated above, our model is useful for the case of narrow flanges because the inextensibility of the flange is not portrayed. For wider flanges, encountered in most service, an alternative model was discussed. From preliminary calculations of the extent of the

deformed zone in the in-plane elastic phase, one can infer that the structural unit fails first by plastic folding rather than elastic buckling. Future work should investigate this new type of failure and identify the mechanism(s) that govern the extent of lateral damage.

Beyond the above suggested theoretical extension, possible future work could include an investigation of the effect of the indenter diameter. As shown in Chapter 6, the alternative model predicts a theoretical extent of the damaged zone in the limit of zero while an estimate of the in-plane plastic zone from the experimental load and the yield strength suggests a value of 0.3 the plate radius. This was nearly independent of the indenter radius.

Better approximations of the displacement fields could also be used to improve the accuracy of the analytical results. One can use smooth surfaces described by trigonometric functions rather than the piece-wise flat plane approximations. However, in light of the mathematical complexity and the lengthy expressions encountered, this is not recommended.

From the experimental side, further tests should be conducted to investigate the effect of punch rather than line loads on wide flanges. In doing so, several modifications to the test apparatus should be implemented. The most pressing one is to monitor the displacements. A dial gauge should be installed between the load point of the test specimen and the machine cross-head. This allows direct measurement of the specimen deflections and avoids major corrections of the test data in the elastic region. Also, the use of electron beam welding rather than brazing in assembling the test specimens is recommended. Because of the local nature of electron beam welding, very small initial imperfections are induced. This will improve considerably the comparison with the theoretical model.

Finally, it is recommended that stiff bulkhead designs be avoided. They are commonly used in both conventional single and double hulls but present hard points which can help

initiate rupture. It is suggested to use less stiff bulkheads and supplement them with tapered brackets. This would delay fracture initiation. It would also spread out deflections and avoid hull rupture.

References

Akita, Y., Fujita, Y., and Kitamura, K., 1972, "Studies on Collision-Protective Structures in Nuclear-Powered Ships", *Nucl. Eng. Design 19*, 365, 1972.

Akita, Y. and Kitamura, K., 1972, "A Study on Collision by an Elastic Stem to a Side Structure of Ships", *J. Soc. Naval Architects of Japan 131*, 307, 1972.

Arita, K. and Aoki, G., 1985, "Strength of Ship Bottom in Grounding (1st Report) - An Investigation into the Case of a Ship Stranded on a Rock", *J. Soc. Naval Architects of Japan*, Vol. 158, 1985.

Caiafa, C. and Neri, L., 1986, "The Controlled Impact Demonstration (CID Structural Experiments, Philosophy and Results)", Symposium on Vehicle Crashworthiness Including Impact Biomechanics, ASME Winter Annual Meeting, 1986.

Choi, S., Wierzbicki, T., and Culbertson-Driscoll, J., 1994, "Crushing Strength of Web Girders", Technical Report No. 23, *Joint MIT-Industry Program on Tanker Safety*, January 1994.

Crandall, S. H. and Dahl, N. C., 1959, "An Intoduction to the Mechanics of Solids", McGraw-Hill Book Company, 1959.

Culbertson-Driscoll, J., 1992, "Crushing Characteristics of Web Girders in Unidirectionally Stiffened Double Hull Structures", Technical Report No. 10, *Joint MIT-Industry Program on Tanker Safety*, May 1992.

Geiger, W., 1989, "Post-buckling Failure of Box Columns", M.S. Thesis, Technical University, Munich, June 1989 (*In German*).

Goksoyr, O., 1994, "Crushing Resistance of Web Girders in Unidirectionally Stiffened Double Hulls", Technical Report No. 20, *Joint MIT-Industry Program on Tanker Safety*, January 1994.

Goktug, G., 1994, "Real-Time Non-Contact Measurement and Analysis for the Control Distortion during Welding", *Ph.D. thesis, Deot. of Ocean Eng., MIT*, June 1994.

Goldfinch, A. C., 1986, "Plate Tearing Energies", Part II Project, Engineering Department, Cambridge University, 1986.

Ito, H., Kondo, K., Yoshimura, N., Kawashima, M., and Yamamoto, S., 1984, "A Simplified Method to Analyze the Strength of Double Hulled Structures in Collisions - 1st Report", *J. Soc. Naval Architects of Japan*, Vol. 156, 1984.

Ito, H., Kondo, K., Yoshimura, N., Kawashima, M., and Yamamoto, S., 1985, "A Simplified Method to Analyze the Strength of Double Hulled Structures in Collisions - 2nd Report", *J. Soc. Naval Architects of Japan*, Vol. 158, 1985.

Ito, H., Kondo, K., Yoshimura, N., Kawashima, M., and Yamamoto, S., 1986, "A Simplified Method to Analyze the Strength of Double Hulled Structures in Collisions - 3rd Report", *J. Soc. Naval Architects of Japan*, 1986.

Jones, N. and Jouri, W. S., 1987, " A Study of Plate Tearing for Ship Collision and Grounding Damage", *J. Ship Research 31*, 253, 1987.

Lu, G. and Calladine, C. R., 1990, "On the Cutting of a Plate by a Wedge", *Int. J. Mechanical Sciences*, Vol. 32, No. 4, pp. 293-313, 1990.

Lusted, M., Orzalli, C., Thomas, G., and Fox, D., 1994, "Littoral Warfare Submarine", Project in New Construction Naval Ship Design, MIT, 27 April 1994.

Maxwell, L. M., 1993, "Effect of Rock Geometry on the Failure Mode of Plates and the Forces in Grounding Experiments", M.Sc. Thesis, Dept. of Ocean Eng., MIT, June 1993.

McClintock, F. A. and Argon, A. A., 1966, "Mechanical Behavior of Materials", Addison-Wesley Publishing Company, 1966, (*Reprinted 1993 by Tech Books, Fairfield, VA*)

Minorsky, V. U., 1959, "An Analysis of Ship Collisions with Reference to Protection of Nuclear Power Plants", *J. Ship Research 3*, 1, 1959.

Oil Pollution Act of 1990, Public Law 101-380, August 18, 1990.

Prager, W., 1959, "An Introduction to Plasticity", Addison-Wesley Publishing Company Inc., 1959.

Prentice, J., 1986, "Wedge Drop Tests to Investigate Plate Tearing Characteristics", Part II Project, Engineering Department, Cambridge University, 1986.

Rhodes, J., 1989, "Ultimate Strength of Thin-walled Components", Manual of Crashworthiness Engineering, Vol. 14, Feb. 198, Technical Report, Dept. of Ocean Eng., MIT, 1989.

Roark, R. and Young, W., 1975, "Formulas for Stress and Strain", McGraw-Hill Book Company, 1975

Timoshenko, S. and Woinowsky-Krieger, S., 1959, "Theory of Plates and Shells", McGraw-Hill Book Company, 1959.

Torenbeek, E., 1982, "Synthesis of Subsonic Airplane Design", Delft University Press, 1982.

Ueda, Y., Kitamura, K., Okamoto, Y., Yoshida, Y., and Katayama, M., 1978, "Ultimate Strength of the Double Bottom Stranding on a Rock", 1978.

Ugural, A., 1981, "Stresses in Plates and Shells", McGraw-Hill Book Company, 1981.

Vaughan, H., 1978, "Bending and Tearing of Plate with Applications to Ship-bottom Damage", *The Naval Architect 97*, May 1978.

Vaughan, H., 1979, "The Tearing and Cutting of Mild Steel Plate with Application to Ship Grounding Damage", *Proceedings 3rd Int. Conf. Mechanical Behaviour of Material*, (edited by K. J. Miller and R. F. Smith), Vol. 3, pp. 479-487, Pergamon Press, Oxford, 1979.

Vaughan, H., 1980, "The Tearing of Mild Steel Plate", *J. Ship Research 24*, 96, 1980.

von Karman, T., Sechler, E., and Donnel, H., 1932 "Strength of Thin Plates in Compression", *Trans. ASME, 53, 53-7*, (1932).

Wierzbicki, T. and Huang, J., 1991, "Initiation of Plastic Folding Mechanism in Crushed Box Columns", *Thin-Walled Structures 13*, pp. 115-143, 1991.

Wierzbicki, T., Yahiaoui, M., and Sinmao, M., 1994, "Research Activities Within the Joint MIT-Industry Project on Tanker Safety", *Advanced Double Hull Technical Symposium*, Gaithersburg, MD, October 1994.

Woisin, G., 1982, "Comments on Vaughan: The Tearing Strength of Mild Steel Plate", *J. Ship Research 26*, 50, 1982.

Yahiaoui, M., Bracco, M., Little, P., and Trauth, K., 1994, "Experimental Studies on Scale Models for Grounding", Technical Report No. 18, *Joint MIT-Industry Program on Tanker Safety*, January 1994.

Appendix A

Calculations Pertinent to Pre-Failure Analysis

A.1 Geometric Considerations

From geometry, using Fig. A.1, we can find λ, η, and ρ as function of ζ and R.

First, $\lambda(\zeta)$ is found from triangle AFO' as follows:

$$\lambda = BO' - FO' = R - \sqrt{AO'^2 - AF^2} = R - \sqrt{R^2 - \zeta^2}$$

Hence,

$$\lambda = R - \sqrt{R^2 - \zeta^2} \tag{A.1}$$

Next, $\eta(\zeta)$ and $\rho(\zeta)$ are found from triangles ODO' and CDG as follows:

We have

$$\frac{OO'}{CG} = \frac{DO'}{DG} \Rightarrow \frac{\rho}{\rho + \eta} = \frac{R}{R + \zeta}$$

Hence,

$$\rho(R + \zeta) = (\rho + \eta)R$$

Therefore, $\rho R + \rho \zeta = \rho R + R \eta$ which give, $\rho = \dfrac{R}{\zeta} \eta$

Also, $\lambda + \eta + \rho = R$

From the above two equations, we get:

$$\eta + \frac{R}{\zeta} \eta = R - \lambda$$

That is using Eq. (A.1)

$$\eta \left(1 + \frac{R}{\zeta} \right) = R - R + \sqrt{R^2 - \zeta^2}$$

which leads to:

$$\eta = \frac{\zeta \sqrt{R^2 - \zeta^2}}{R + \zeta}, \qquad \text{and} \qquad \rho = \frac{\zeta R \sqrt{R^2 - \zeta^2}}{\zeta R + \zeta}$$

Finally,

$$\eta = \frac{\zeta \sqrt{R^2 - \zeta^2}}{R + \zeta} \tag{A.2}$$

$$\rho = \frac{R \sqrt{R^2 - \zeta^2}}{R + \zeta} \tag{A.3}$$

A.2 Displacement Fields

As discussed in Section 2.1.2 on page page 17, the postulated displacement field is as shown in Fig. 2.6 on page 39. Using the nodal displacements in the 3-nodes elements with constant strain, expressions for $u\,(x, y)$, $v\,(x, y)$, and $w\,(x, y)$ can be found as follows:

i) For $0 \leq x \leq \eta$:

Assume

136

$$u(x, y) = \alpha_1 x + \alpha_2 y + \alpha_3$$
$$v(x, y) = \alpha_4 x + \alpha_5 y + \alpha_6$$
$$w(x, y) = \alpha_7 x + \alpha_8 y + \alpha_9$$

and use the nine nodal displacements to find the nine unknown coefficients α_i. The nodal displacements are:

$$
\begin{array}{lll}
u(0, 0) = 0 & v(0, 0) = 0 & w(0, 0) = 0 \\
u(\eta, \zeta) = 0 & v(\eta, \zeta) = 0 & w(\eta, \zeta) = 0 \\
u(\eta, 0) = -u^* & v(\eta, 0) = 0 & w(\eta, 0) = w_0
\end{array}
$$

ii) For $\eta \leq x \leq \eta + \lambda$:

Use the same procedure as for the case where $0 \leq x \leq \eta$ with the following nodal displacements:

$$
\begin{array}{lll}
u(\eta, 0) = -u^* & v(\eta, 0) = 0 & w(\eta, 0) = w_0 \\
u(\eta, \zeta) = 0 & v(\eta, \zeta) = 0 & w(\eta, \zeta) = 0 \\
u(\eta + \lambda, 0) = -u_0 & v(\eta + \lambda, 0) = 0 & w(\eta + \lambda, 0) = 0
\end{array}
$$

The final result is given by:

$$
u(x, y) =
\begin{cases}
u^*\left(-\dfrac{x}{\eta} + \dfrac{y}{\zeta}\right) & ; \text{for } 0 \leq x \leq \eta \\[2mm]
u_0\left(-\dfrac{x}{\lambda} + \dfrac{\eta}{\lambda}\right) + u^*\left(\dfrac{x}{\lambda} + \dfrac{y}{\zeta} - \dfrac{\eta + \lambda}{\lambda}\right) & ; \text{for } \eta \leq x \leq \eta + \lambda
\end{cases}
\tag{A.4}
$$

$$v(x, y) = 0 \qquad ; \text{everywhere} \tag{A.5}$$

$$
w(x, y) =
\begin{cases}
w_0\left(\dfrac{x}{\eta} - \dfrac{y}{\zeta}\right) & ; \text{for } 0 \leq x \leq \eta \\[2mm]
w_0\left(-\dfrac{x}{\lambda} - \dfrac{y}{\zeta} + \dfrac{\lambda + \eta}{\lambda}\right) & ; \text{for } \eta \leq x \leq \eta + \lambda
\end{cases}
\tag{A.6}
$$

A.3 Strain Field

The strain field is calculated from:

$$\varepsilon_{\alpha\beta} = \frac{1}{2}\left(u_{\alpha,\beta} + u_{\beta,\alpha}\right) + \frac{1}{2}w_{,\alpha}w_{,\beta} \qquad (A.7)$$

which, in the x-direction reduces to

$$\varepsilon_x = \frac{\partial u}{\partial x} + \frac{1}{2}\left(\frac{\partial w}{\partial x}\right)^2$$

That is making use of Eqs. (A.4) and (A.6), we get:

$$\varepsilon_x = \begin{cases} -\dfrac{1}{\eta}u^* + \dfrac{1}{2\eta^2}w_0^2 & ;\text{ for } 0 \leq x \leq \eta \\[3mm] -\dfrac{1}{\lambda}u_0 + \dfrac{1}{\lambda}u^* + \dfrac{1}{2\lambda^2}w_0^2 & ;\text{ for } \eta \leq x \leq \eta + \lambda \end{cases} \qquad (A.8)$$

Also from Eq. (A.7) one gets:

$$\varepsilon_y = \frac{\partial v}{\partial y} + \frac{1}{2}\left(\frac{\partial w}{\partial y}\right)^2$$

That is making use of Eqs. (A.5) and (A.6), we get:

138

$$\varepsilon_y = \frac{1}{2\zeta^2}w_0^2 \qquad ; \text{ everywhere}$$

In the same manner from Eq. (A.7) one gets:

$$\varepsilon_{xy} = \frac{1}{2}\left(\frac{\partial u}{\partial y}+\frac{\partial v}{\partial x}\right)+\frac{1}{2}\frac{\partial w}{\partial x}\frac{\partial w}{\partial y}$$

and making use of Eqs. (A.4), (A.5), and (A.6) we get:

$$\varepsilon_{xy} = \begin{cases} \dfrac{1}{2\zeta}u^* - \dfrac{1}{2\eta\zeta}w_0^2 & ; \text{for } 0 \le x \le \eta \\[3mm] \dfrac{1}{2\zeta}u^* + \dfrac{1}{2\lambda\zeta}w_0^2 & ; \text{for } \eta \le x \le \eta + \lambda \end{cases}$$

In conclusion, the entire strain field has been found to be as follows:

i) For $0 \le x \le \eta$:

$$\varepsilon_{\alpha\beta} = \begin{bmatrix} -\dfrac{1}{\eta}u^* + \dfrac{1}{2\eta^2}w_0^2 & \dfrac{1}{2\zeta}u^* - \dfrac{1}{2\eta\zeta}w_0^2 \\[3mm] \dfrac{1}{2\zeta}u^* - \dfrac{1}{2\eta\zeta}w_0^2 & \dfrac{1}{2\zeta^2}w_0^2 \end{bmatrix} \qquad (A.9)$$

ii) For $\eta \le x \le \eta + \lambda$:

$$\varepsilon_{\alpha\beta} = \begin{bmatrix} -\dfrac{1}{\lambda}u_0 + \dfrac{1}{\lambda}u^* + \dfrac{1}{2\lambda^2}w_0^2 & \dfrac{1}{2\zeta}u^* + \dfrac{1}{2\lambda\zeta}w_0^2 \\[3mm] \dfrac{1}{2\zeta}u^* + \dfrac{1}{2\lambda\zeta}w_0^2 & \dfrac{1}{2\zeta^2}w_0^2 \end{bmatrix} \qquad (A.10)$$

A.4 Calculation of the Membrane and Bending Energies

In what follows, because of symmetry, only half of the plate is considered in the derivation of the membrane and bending energies.

A.4.1 Membrane Energy

Timoshenko and Woinowsky-Krieger (1959) showed that the membrane energy U_m is expressed by

$$U_m = \frac{Et}{2(1-v^2)} \int_S [\varepsilon_x^2 + \varepsilon_y^2 + 2v\varepsilon_x\varepsilon_y + 2(1-v)\varepsilon_{xy}^2]\, dS$$

That is, using the two surfaces S_I and S_{II} shown in Fig. A.2, we get

$$U_m = \frac{Et}{2(1-v^2)} \left\{ \int_{S_I} \left[\varepsilon_{x_I}^2 + \varepsilon_{y_I}^2 + 2v\varepsilon_{x_I}\varepsilon_{y_I} + 2(1-v)\varepsilon_{xy_I}^2\right] dS_I \right. \tag{A.11}$$

$$\left. + \int_{S_{II}} \left[\varepsilon_{x_{II}}^2 + \varepsilon_{y_{II}}^2 + 2v\varepsilon_{x_{II}}\varepsilon_{y_{II}} + 2(1-v)\varepsilon_{xy_{II}}^2\right] dS_{II} \right\}$$

Now, set:

$$A = \int_{S_I} \left[\varepsilon_{x_I}^2 + \varepsilon_{y_I}^2 + 2v\varepsilon_{x_I}\varepsilon_{y_I} + 2(1-v)\varepsilon_{xy_I}^2\right] dS_I \tag{A.12}$$

and

$$B = \int_{S_{II}} \left[\varepsilon_{x_{II}}^2 + \varepsilon_{y_{II}}^2 + 2v\varepsilon_{x_{II}}\varepsilon_{y_{II}} + 2(1-v)\varepsilon_{xy_{II}}^2\right] dS_{II} \tag{A.13}$$

Using Eqs. (A.9) and (A.10) for the axial and shear strains along with the fact that

$$\int_{S_I} dS_I = \frac{1}{2}\zeta\eta \qquad \text{and} \qquad \int_{S_{II}} dS_{II} = \frac{1}{2}\zeta\lambda$$

in Eqs. (A.12) and (A.13), we get:

$$A = \left(\left[-\frac{1}{\eta}u^* + \frac{1}{2\eta^2}w_0^2 \right]^2 + \left[\frac{1}{2\zeta^2}w_0^2 \right]^2 + 2v \left[-\frac{1}{\eta}u^* + \frac{1}{2\eta^2}w_0^2 \right] \left[\frac{1}{2\zeta^2}w_0^2 \right] \right.$$

$$\left. + 2(1-v) \left[\frac{1}{2\zeta}u^* - \frac{1}{2\eta\zeta}w_0^2 \right]^2 \right) \frac{1}{2}\zeta\eta$$

(A.14)

and

$$B = \left(\left[-\frac{1}{\lambda}u_0 + \frac{1}{\lambda}u^* + \frac{1}{2\lambda^2}w_0^2 \right]^2 + \left[\frac{1}{2\zeta^2}w_0^2 \right]^2 + 2v \left[-\frac{1}{\lambda}u_0 + \frac{1}{\lambda}u^* + \frac{1}{2\lambda^2}w_0^2 \right] \left[\frac{1}{2\zeta^2}w_0^2 \right] \right.$$

$$\left. + 2(1-v) \left[\frac{1}{2\zeta}u^* + \frac{1}{2\lambda\zeta}w_0^2 \right]^2 \right) \frac{1}{2}\zeta\lambda$$

(A.15)

Finally Eqs. (A.14) and (A.15) in (A.11) give after simplification the following final expression for the membrane energy

$$U_m = \frac{Et}{2(1-v^2)} \left[C_1 w_0^4 + C_2 u_0 w_0^2 + C_3 u^* w_0^2 + C_4 u^* u_0 + C_5 u^{*2} + C_6 u_0^2 \right]$$

where

$$C_1 = \frac{1}{8}\frac{\zeta}{\eta^3} + \frac{1}{8}\frac{\eta}{\zeta^3} + \frac{1}{4}\frac{1}{\eta\zeta} + \frac{1}{8}\frac{\zeta}{\lambda^3} + \frac{1}{8}\frac{\lambda}{\zeta^3} + \frac{1}{4}\frac{1}{\lambda\zeta}$$

$$C_2 = -\frac{1}{2}\frac{\zeta}{\lambda^2} - \frac{1}{2}\frac{v}{\zeta}$$

$$C_3 = -\frac{1}{2}\frac{\zeta}{\eta^2} - \frac{1}{2}\frac{\zeta}{\lambda^2}$$

141

$$C_4 = -\frac{\zeta}{\lambda}$$

$$C_5 = \frac{1}{2}\frac{\zeta}{\eta} + \frac{1}{4}\frac{\eta}{\zeta} - \frac{1}{4}\frac{\nu\eta}{\zeta} + \frac{1}{2}\frac{\zeta}{\lambda} + \frac{1}{4}\frac{\lambda}{\zeta} - \frac{1}{4}\frac{\nu\lambda}{\zeta}$$

$$C_6 = \frac{1}{2}\frac{\zeta}{\lambda}$$

A.4.2 Bending Energy

The bending energy U_b is defined by (Geiger, 1989)

$$U_b = \frac{Et^3}{24(1-\nu^2)} \int_S (\kappa_x + \kappa_y)^2 dS \qquad (A.16)$$

where S is the surface area, and κ_x and κ_y are the bending curvatures, defined by

$$\kappa_x = \frac{\partial^2 w}{\partial x^2} \qquad \text{and} \qquad \kappa_y = \frac{\partial^2 w}{\partial y^2}$$

Because slope discontinuity are not admissible in elastic structures, we need to smooth-out the edges of the two-degree-of-freedom model developed in Section 2.1.2 on page 18. The smoothening process is achieved through the use average curvatures $(\kappa_x)_{avg}$ and $(\kappa_y)_{avg}$ in the calculation.

In general, the average curvature is found as follows:

From geometry,
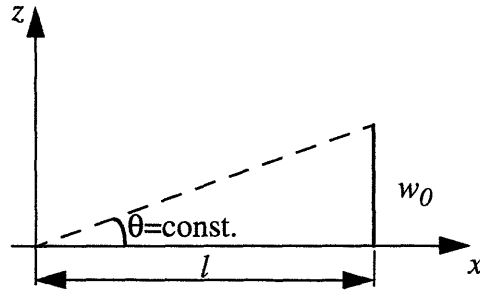
the average curvature is

$$\kappa_{avg} \equiv \frac{d\theta}{dS} = \frac{\theta}{\dfrac{l}{\cos\theta}} \qquad (A.17)$$

where

$$\sin\theta = \frac{w_0}{\dfrac{l}{\cos\theta}} \qquad (A.18)$$

For small angle θ, we have $\cos\theta \approx 1$ and $\sin\theta \approx \theta$. And Eqs. (A.17) and (A.18) reduce respectively to

$$\kappa_{avg} = \frac{\theta}{l} \qquad (A.19)$$

and

$$\theta \approx \frac{w_0}{l} \qquad (A.20)$$

Finally, combining Eqs. (A.19) and (A.20) gives the general expression for the average curvature

$$\kappa_{avg} = \frac{w_0}{l^2}$$

Using this result, one can write

$$(\kappa_x)_{avg} = \begin{cases} (\kappa_{x_I})_{avg} = \dfrac{w_0}{\eta^2} \; ; \text{for } 0 \le x \le \eta \\[2mm] (\kappa_{x_{II}})_{avg} = \dfrac{w_0}{\lambda^2} \; ; \text{for } \eta \le x \le \eta + \lambda \end{cases} \tag{A.21}$$

$$(\kappa_y)_{avg} = \frac{w_0}{\zeta^2} \tag{A.22}$$

Now, Eqs. (A.21) and (A.22) in Eq. (A.16) (the expression for the bending energy) give

$$U_b = \frac{Et^3}{24(1-v^2)} \left\{ \int_{S_I} [\,(\kappa_{x_I})_{avg} + (\kappa_y)_{avg}\,]^2 dS_I + \int_{S_{II}} [\,(\kappa_{x_{II}})_{avg} + (\kappa_y)_{avg}\,]^2 dS_{II} \right\}$$

or

$$U_b = \frac{Et^3}{12(1-v^2)} \left\{ \left[\frac{w_0}{\eta^2} + \frac{w_0}{\zeta^2}\right]^2 \frac{1}{2}\zeta\eta + \left[\frac{w_0}{\lambda^2} + \frac{w_0}{\zeta^2}\right]^2 \frac{1}{2}\zeta\lambda \right\}$$

The areas S_I and S_{II} are shown in Fig. A.2 and were used earlier in the calculation of the membrane energy.

Finally, the bending energy takes the following form:

144

$$U_b = \frac{Et^3}{24(1-v^2)} C_7 w_0{}^2$$

where

$$C_7 = \frac{\zeta}{\eta^3} + \frac{\eta}{\zeta^3} + \frac{2}{\zeta\eta} + \frac{\zeta}{\lambda^3} + \frac{\lambda}{\zeta^3} + \frac{2}{\lambda\zeta}$$

A.5 Non-dimensionalization

Starting from the dimensionless parameters defined in Section 2.3 on page 21, that is

$$\bar\zeta = \frac{\zeta}{R}; \qquad \bar P = \frac{PR}{D}; \qquad \bar u = \frac{uR}{t^2}$$

where

$$D = \frac{Et^3}{12(1-v^2)}$$

one can derive all of the following dimensionless parameters

$$\bar\lambda = \frac{\lambda}{R} = \frac{R - \sqrt{R^2 - \zeta^2}}{R} = 1 - \sqrt{1 - \left(\frac{\zeta}{R}\right)^2} = 1 - \sqrt{1 - \bar\zeta^2}$$

$$\bar\eta = \frac{\eta}{R} = \frac{\zeta\sqrt{R^2 - \zeta^2}}{R(R+\zeta)} = \frac{\frac{\zeta}{R}\sqrt{1 - \left(\frac{\zeta}{R}\right)^2}}{1 + \frac{\zeta}{R}} = \frac{\bar\zeta\sqrt{1 - \bar\zeta^2}}{1 + \bar\zeta}$$

and

$$\bar{C_1} = C_1 R^2 ; \qquad \bar{C_2} = C_2 R ; \qquad \bar{C_3} = C_3 R ;$$

$$\bar{C_4} = C_4 ; \qquad \bar{C_5} = C_5 ; \qquad \bar{C_6} = C_6 ;$$

$$\bar{C_7} = C_7 R^2 ;$$

145

That is

$$\overline{C}_1 = \frac{1}{8}\frac{\overline{\zeta}}{\overline{\eta}^3} + \frac{1}{8}\frac{\overline{\eta}}{\overline{\zeta}^3} + \frac{1}{4}\frac{1}{\overline{\eta}\overline{\zeta}} + \frac{1}{8}\frac{\overline{\zeta}}{\overline{\lambda}^3} + \frac{1}{8}\frac{\overline{\lambda}}{\overline{\zeta}^3} + \frac{1}{4}\frac{1}{\overline{\lambda}\overline{\zeta}}$$

$$\overline{C}_2 = -\frac{1}{2}\frac{\overline{\zeta}}{\overline{\lambda}^2} - \frac{1}{2}\frac{\nu}{\overline{\zeta}}$$

$$\overline{C}_3 = -\frac{1}{2}\frac{\overline{\zeta}}{\overline{\eta}^2} - \frac{1}{2}\frac{\overline{\zeta}}{\overline{\lambda}^2}$$

$$\overline{C}_4 = -\frac{\overline{\zeta}}{\overline{\lambda}}$$

$$\overline{C}_5 = \frac{1}{2}\frac{\overline{\zeta}}{\overline{\eta}} + \frac{1}{4}\frac{\overline{\eta}}{\overline{\zeta}} - \frac{1}{4}\frac{\nu\overline{\eta}}{\overline{\zeta}} + \frac{1}{2}\frac{\overline{\zeta}}{\overline{\lambda}} + \frac{1}{4}\frac{\overline{\lambda}}{\overline{\zeta}} - \frac{1}{4}\frac{\nu\overline{\lambda}}{\overline{\zeta}}$$

$$\overline{C}_6 = \frac{1}{2}\frac{\overline{\zeta}}{\overline{\lambda}}$$

$$\overline{C}_7 = \frac{\overline{\zeta}}{\overline{\eta}^3} + \frac{\overline{\eta}}{\overline{\zeta}^3} + \frac{2}{\overline{\zeta}\overline{\eta}} + \frac{\overline{\zeta}}{\overline{\lambda}^3} + \frac{\overline{\lambda}}{\overline{\zeta}^3} + \frac{2}{\overline{\lambda}\overline{\zeta}}$$

Using all above dimensionless parameters, the primary equilibrium path load P_I and the secondary equilibrium path load P_{II} defined by Eqs. (2.19) and (2.20) on page 25 can be

146

written in a non-dimensional form as follows:

$$\bar{P}_I = \frac{Et}{(1-v^2)}\left(2\bar{C}_6 - \frac{\bar{C}_4^2}{2\bar{C}_5}\right)\frac{\bar{u}_0 t^2}{R}\ \frac{R}{\dfrac{Et^3}{12(1-v^2)}}$$

$$= 12\left(2\bar{C}_6 - \frac{\bar{C}_4^2}{2\bar{C}_5}\right)\bar{u}_0$$

$$\bar{P}_{II} = \frac{Et}{(1-v^2)}\left\{\left[2\bar{C}_6 - \frac{\bar{C}_4^2}{2\bar{C}_5} - 2\frac{\left(\dfrac{\bar{C}_2}{R} - \dfrac{\bar{C}_3\bar{C}_4}{2R\bar{C}_5}\right)^2}{\left(4\dfrac{\bar{C}_1}{R^2} - \dfrac{\bar{C}_3^2}{\bar{C}_5 R^2}\right)}\right]\frac{\bar{u}_0 t^2}{R} - \frac{t^2 R^2}{6}\frac{\dfrac{\bar{C}_7}{R^2}\left(\dfrac{\bar{C}_2}{R} - \dfrac{\bar{C}_3\bar{C}_4}{2R\bar{C}_5}\right)}{\left(4\dfrac{\bar{C}_1}{R^2} - \dfrac{\bar{C}_3^2}{\bar{C}_5 R^2}\right)}\right\}\frac{R}{\dfrac{Et^3}{12(1-v^2)}}$$

$$= 12\left[2\bar{C}_6 - \frac{\bar{C}_4^2}{2\bar{C}_5} - 2\frac{\left(\bar{C}_2 - \dfrac{\bar{C}_3\bar{C}_4}{2\bar{C}_5}\right)^2}{\left(4\bar{C}_1 - \dfrac{\bar{C}_3^2}{\bar{C}_5}\right)}\right]\bar{u}_0 - \frac{2\bar{C}_7\left(\bar{C}_2 - \dfrac{\bar{C}_3\bar{C}_4}{2\bar{C}_5}\right)}{\left(4\bar{C}_1 - \dfrac{\bar{C}_3^2}{\bar{C}_5}\right)}$$

A.6 Calculation of Membrane Yield

First, one needs to write the components of the strain tensor in terms of u_0 only. This is done by making use of the expressions of u^* and w_0 as function of u_0 (Eqs. (2.14) and (2.18) of Section 2.7 on page 30).

The axial and shear strains reduce to the following:

$$\varepsilon_x = \begin{cases} D_1 u_0 + D_2 & ;\ \text{for}\ \ 0 \le x \le \eta \\ (D_1{}^*)\, u_0 + D_2{}^* & ;\ \text{for}\ \ \eta \le x \le \eta + \lambda \end{cases}$$

$$\varepsilon_y = D_3 u_0 + D_4 = D_3{}^* u_0 + D_4{}^* \qquad ;\ \text{everywhere}$$

$$\varepsilon_{xy} = \begin{cases} D_5 u_0 + D_6 & ;\ \text{for}\ \ 0 \le x \le \eta \\ (D_5{}^*)\, u_0 + D_6{}^* & ;\ \text{for}\ \ \eta \le x \le \eta + \lambda \end{cases}$$

where

$$D_1 = \frac{1}{2\eta}\frac{C_4}{C_5} - \left(\frac{1}{2\eta}\frac{C_3}{C_5} + \frac{1}{2\eta^2}\right)\frac{\left(2C_2 - \frac{C_3 C_4}{C_5}\right)}{\left(4C_1 - \frac{C_3^2}{C_5}\right)}$$

$$D_2 = -\left(\frac{1}{2\eta}\frac{C_3}{C_5} + \frac{1}{2\eta^2}\right)\frac{t^2 C_7}{6\left(4C_1 - \frac{C_3^2}{C_5}\right)}$$

$$D_3 = -\frac{1}{2\zeta^2}\frac{\left(2C_2 - \frac{C_3 C_4}{C_5}\right)}{\left(4C_1 - \frac{C_3^2}{C_5}\right)}$$

$$D_4 = -\frac{1}{2\zeta^2}\frac{t^2 C_7}{6\left(4C_1 - \frac{C_3^2}{C_5}\right)}$$

$$D_5 = -\frac{1}{4\zeta}\frac{C_4}{C_5} + \left(\frac{1}{4\zeta}\frac{C_3}{C_5} + \frac{1}{2\eta\zeta}\right)\frac{\left(2C_2 - \frac{C_3 C_4}{C_5}\right)}{\left(4C_1 - \frac{C_3^2}{C_5}\right)}$$

$$D_6 = \left(\frac{1}{4\zeta}\frac{C_3}{C_5} + \frac{1}{2\eta\zeta}\right)\frac{t^2 C_7}{6\left(4C_1 - \frac{C_3^2}{C_5}\right)}$$

$$D_1^* = -\frac{1}{\lambda} - \frac{1}{2\lambda}\frac{C_4}{C_5} - \left(\frac{1}{2\lambda^2} - \frac{1}{2\lambda}\frac{C_3}{C_5}\right)\frac{\left(2C_2 - \frac{C_3 C_4}{C_5}\right)}{\left(4C_1 - \frac{C_3^2}{C_5}\right)}$$

$$D_2^* = -\left(\frac{1}{2\lambda^2} - \frac{1}{2\lambda}\frac{C_3}{C_5}\right)\frac{t^2 C_7}{6\left(4C_1 - \frac{C_3^2}{C_5}\right)}$$

$$D_3^* = D_3$$

148

$$D_4{}^* = D_4$$

$$D_5{}^* = -\frac{1}{4\zeta}\frac{C_4}{C_5} + \left(\frac{1}{4\zeta}\frac{C_3}{C_5} - \frac{1}{2\lambda\zeta}\right)\frac{\left(2C_2 - \dfrac{C_3 C_4}{C_5}\right)}{\left(4C_1 - \dfrac{C_3{}^2}{C_5}\right)}$$

$$D_6{}^* = \left(\frac{1}{4\zeta}\frac{C_3}{C_5} - \frac{1}{2\lambda\zeta}\right)\frac{t^2 C_7}{6\left(4C_1 - \dfrac{C_3{}^2}{C_5}\right)}$$

Therefore, the yield condition in Section 2.7 on page 30 given by Eq. (2.32) becomes for the case where $0 \le x \le \eta$ as follows:

$$a_1 [(D_1 u_0 + D_2)^2 + (D_3 u_0 + D_4)^2] - a_2 (D_1 u_0 + D_2)(D_3 u_0 + D_4)$$

$$+ a_3 (D_5 u_0 + D_6)^2 = \left(\frac{\sigma_0}{E}\right)^2$$

and reduces further to:

$$A u_0{}^2 + B u_0 + \left[C - \left(\frac{\sigma_0}{E}\right)^2\right] = 0 \qquad\qquad \text{(A.23)}$$

where

$$A = a_1 (D_1{}^2 + D_3{}^2) - a_2 D_1 D_3 + a_3 D_5{}^2$$

$$B = 2a_1 (D_1 D_2 + D_3 D_4) - a_2 (D_1 D_4 + D_2 D_3) + 2a_3 D_5 D_6$$

$$C = a_1 (D_2{}^2 + D_4{}^2) - a_2 D_2 D_4 + a_3 D_6{}^2$$

Eq. (A.23) is also valid for the case where $\eta \le x \le \eta + \lambda$. One need only to replace the parameters $D_i(\zeta)$; $(i = 1, ..., 6)$ by their counterpart $D_i{}^*(\zeta)$; $(i = 1, ..., 6)$.

In what follows, we derive a dimensionless form of Eq. (A.23). Using all previously defined nondimensional parameters and for the case where $0 \le x \le \eta$, one gets:

$$\overline{a_1} = a_1 = \frac{v^2 - v + 1}{(1 - v^2)^2}$$

$$\overline{a_2} = a_2 = \frac{v^2 - 4v + 1}{(1 - v^2)^2}$$

$$\overline{a_3} = a_3 = \frac{3}{(1 + v)^2}$$

$$\overline{D_1} = D_1 R \; ; \qquad \overline{D_2} = D_2 \frac{R^2}{t^2} \; ; \qquad \overline{D_3} = D_3 R \; ;$$

$$\overline{D_4} = D_4 \frac{R^2}{t^2} \; ; \qquad \overline{D_5} = D_5 R \; ; \qquad \overline{D_6} = D_6 \frac{R^2}{t^2} \; ;$$

$$\overline{A} = AR^2 = \overline{a_1} (\overline{D_1}^2 + \overline{D_3}^2) - \overline{a_2}\overline{D_1}\overline{D_3} + \overline{a_3}\overline{D_5}^2$$

$$\overline{B} = B\frac{R^3}{t^2} = 2\overline{a_1} (\overline{D_1}\overline{D_2} + \overline{D_3}\overline{D_4}) - \overline{a_2} (\overline{D_1}\overline{D_4} + \overline{D_2}\overline{D_3}) + 2\overline{a_3}\overline{D_5}\overline{D_6}$$

$$\overline{C} = C\frac{R^4}{t^4} = \overline{a_1} (\overline{D_2}^2 + \overline{D_4}^2) - \overline{a_2}\overline{D_2}\overline{D_4} + \overline{a_3}\overline{D_6}^2$$

Finally Eq. (A.23) can be rewritten as:

$$\frac{\bar{A}}{R^2}u_0{}^2 + \frac{t^2}{R^3}\bar{B}u_0 + \frac{t^4}{R^4}\bar{C} - \left(\frac{\sigma_0}{E}\right)^2 = 0$$

multiplying both sides of the above equation by $\left(\dfrac{R}{t}\right)^4$ leads to

$$\bar{A}\left(\frac{Ru_0}{t^2}\right)^2 + \bar{B}\left(\frac{Ru_0}{t^2}\right) + \bar{C} - \left(\frac{R}{t}\sqrt{\frac{\sigma_0}{E}}\right)^4 = 0$$

or

$$\bar{A}\bar{u}_0{}^2 + \bar{B}\bar{u}_0 + \left(\bar{C} - \frac{1}{\beta^4}\right) = 0 \qquad\qquad\qquad (A.24)$$

where $\beta = \dfrac{t}{R}\sqrt{\dfrac{E}{\sigma_0}}$ is the slenderness ratio parameter.

Again, Eq. (A.24) is also valid for the case where $\eta \le x \le \eta + \lambda$. One need only to replace the parameters $\bar{D}_i(\zeta)$; $(i = 1, ..., 6)$ by their following counterparts:

$$\bar{D}_1{}^* = D_1 {}^* R ; \qquad \bar{D}_2{}^* = D_2 {}^* \frac{R^2}{t^2} ; \qquad \bar{D}_3{}^* = D_3 {}^* R ;$$

$$\bar{D}_4{}^* = D_4 {}^* \frac{R^2}{t^2} ; \qquad \bar{D}_5{}^* = D_5 {}^* R ; \qquad \bar{D}_6{}^* = D_6 {}^* \frac{R^2}{t^2} ;$$
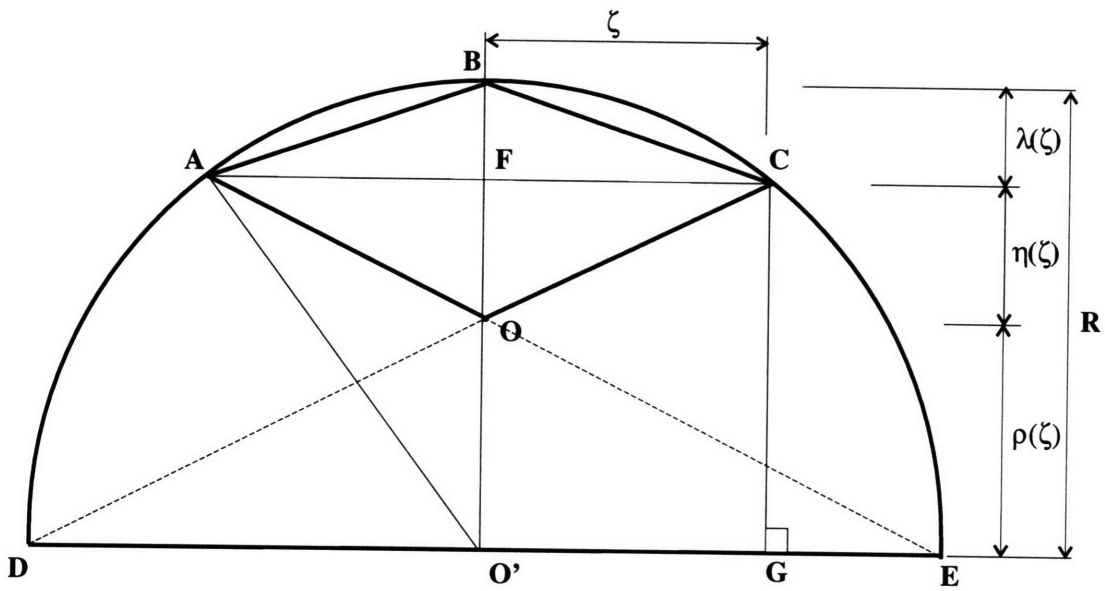
Figure A.1: Geometric Considerations
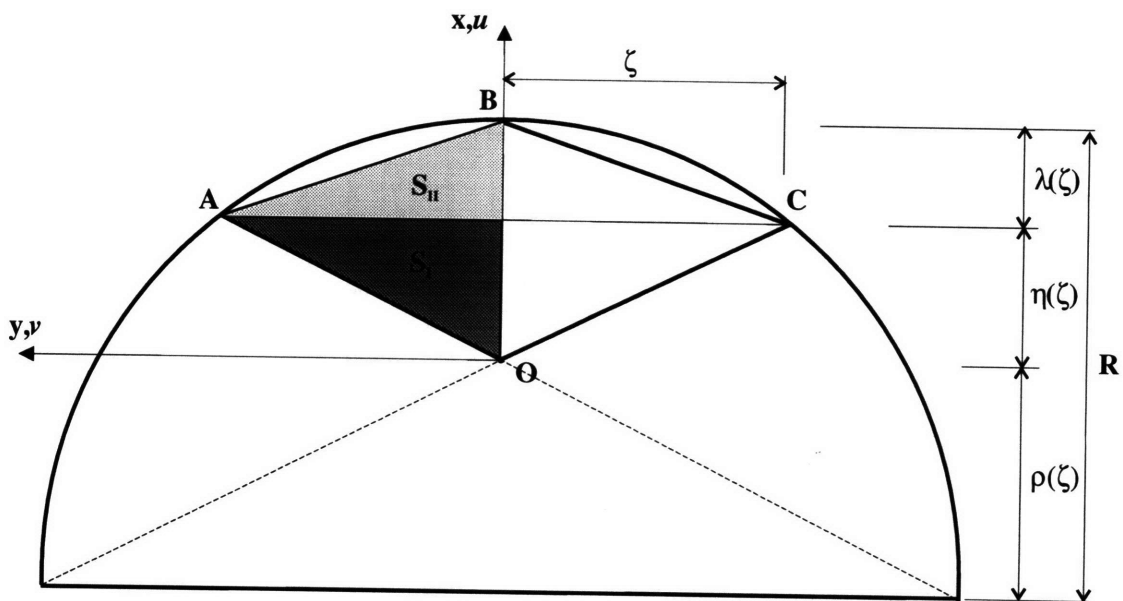
Figure A.2: Definition of Areas used in Bending and Membrane Calculations

Appendix B

Calculations Pertinent to Effect of Initial Imperfections

B.1 Displacement and Strain Fields

In Section 3.1 on page 48, the postulated displacement field was described by the following expressions,

$$u(x, y) = \begin{cases} u^*\left(-\dfrac{x}{\eta} + \dfrac{y}{\zeta}\right) & ; \text{for } 0 \le x \le \eta \\[2ex] u_0\left(-\dfrac{x}{\lambda} + \dfrac{\eta}{\lambda}\right) + u^*\left(\dfrac{x}{\lambda} + \dfrac{y}{\zeta} - \dfrac{\eta + \lambda}{\lambda}\right) & ; \text{for } \eta \le x \le \eta + \lambda \end{cases}$$

$$v(x, y) = 0 \qquad ; \text{everywhere}$$

$$w(x, y) = \begin{cases} w_0\left(\dfrac{x}{\eta} - \dfrac{y}{\zeta}\right) & ; \text{for } 0 \le x \le \eta \\[2ex] w_0\left(-\dfrac{x}{\lambda} - \dfrac{y}{\zeta} + \dfrac{\lambda + \eta}{\lambda}\right) & ; \text{for } \eta \le x \le \eta + \lambda \end{cases}$$

$$\tilde{w}(x, y) = \begin{cases} \tilde{w}_0\left(\dfrac{x}{\eta} - \dfrac{y}{\zeta}\right) & ; \text{for } 0 \le x \le \eta \\[2ex] \tilde{w}_0\left(-\dfrac{x}{\lambda} - \dfrac{y}{\zeta} + \dfrac{\lambda + \eta}{\lambda}\right) & ; \text{for } \eta \le x \le \eta + \lambda \end{cases}$$

153

From the theory of moderately large displacement of plates,

$$\varepsilon_{\alpha\beta} = \frac{1}{2}(u_{\alpha,\beta} + u_{\beta,\alpha}) + \frac{1}{2}(w_{,\alpha}\, w_{,\beta} - \tilde{w}_{,\alpha}\, \tilde{w}_{,\beta}) \qquad (B.1)$$

and using the above postulated displacement field, one finds the axial and shear strains ε_x, ε_y, and ε_{xy}.

B.1.1 Strain ε_x

Setting $\alpha = \beta = x$ in Eq. (B.1), one gets

$$\varepsilon_x = \frac{\partial u}{\partial x} + \frac{1}{2}\left[\left(\frac{\partial w}{\partial x}\right)^2 - \left(\frac{\partial \tilde{w}}{\partial x}\right)^2\right]$$

that is

$$\varepsilon_x = \begin{cases} -\dfrac{u^*}{\eta} + \dfrac{1}{2}\left[\left(\dfrac{w_0}{\eta}\right)^2 - \left(\dfrac{\tilde{w}_0}{\eta}\right)^2\right] & ; \text{for } 0 \le x \le \eta \\[3mm] -\dfrac{u_0}{\lambda} + \dfrac{u^*}{\lambda} + \dfrac{1}{2}\left[\left(-\dfrac{w_0}{\lambda}\right)^2 - \left(-\dfrac{\tilde{w}_0}{\lambda}\right)^2\right] & ; \text{for } \eta \le x \le \eta + \lambda \end{cases}$$

hence,

$$\varepsilon_x = \begin{cases} -\dfrac{u^*}{\eta} + \dfrac{1}{2\eta^2}\left(w_0{}^2 - \tilde{w}_0{}^2\right) & ; \text{for } 0 \le x \le \eta \\[3mm] -\dfrac{u_0}{\lambda} + \dfrac{u^*}{\lambda} + \dfrac{1}{2\lambda^2}\left(w_0{}^2 - \tilde{w}_0{}^2\right) & ; \text{for } \eta \le x \le \eta + \lambda \end{cases} \qquad (B.2)$$

B.1.2 Strain ε_y

Setting $\alpha = \beta = y$ in Eq. (B.1), one gets

154

$$\varepsilon_y = \frac{\partial v}{\partial y} + \frac{1}{2}\left[\left(\frac{\partial w}{\partial y}\right)^2 - \left(\frac{\partial \tilde{w}}{\partial y}\right)^2\right]$$

that is

$$\varepsilon_y = \frac{1}{2}\left[\left(-\frac{w_0}{\zeta}\right)^2 - \left(-\frac{\tilde{w}_0}{\zeta}\right)^2\right] \qquad ; \text{everywhere}$$

hence,

$$\varepsilon_y = \frac{1}{2\zeta^2}\left(w_0{}^2 - \tilde{w}_0{}^2\right) \qquad ; \text{everywhere} \qquad (B.3)$$

B.1.3 Strain ε_{xy}

Setting $\alpha = x$ and $\beta = y$ in Eq. (B.1), one gets

$$\varepsilon_{xy} = \frac{1}{2}\left(\frac{\partial u}{\partial y} + \frac{\partial v}{\partial x}\right) + \frac{1}{2}\left(\frac{\partial w}{\partial x}\frac{\partial w}{\partial y} - \frac{\partial \tilde{w}}{\partial x}\frac{\partial \tilde{w}}{\partial y}\right)$$

that is

$$\varepsilon_{xy} = \begin{cases} \dfrac{1}{2}\left(\dfrac{u^*}{\zeta}\right) + \dfrac{1}{2}\left[\left(\dfrac{w_0}{\eta}\right)\left(-\dfrac{w_0}{\zeta}\right) - \left(\dfrac{\tilde{w}_0}{\eta}\right)\left(-\dfrac{\tilde{w}_0}{\zeta}\right)\right] & ; \text{for } 0 \leq x \leq \eta \\[4mm] \dfrac{1}{2}\left(\dfrac{u^*}{\zeta}\right) + \dfrac{1}{2}\left[\left(-\dfrac{w_0}{\lambda}\right)\left(-\dfrac{w_0}{\zeta}\right) - \left(-\dfrac{\tilde{w}_0}{\lambda}\right)\left(-\dfrac{\tilde{w}_0}{\zeta}\right)\right] & ; \text{for } \eta \leq x \leq \eta + \lambda \end{cases}$$

hence,

$$\varepsilon_{xy} = \begin{cases} \dfrac{1}{2\zeta}u^* - \dfrac{1}{2\eta\zeta}\left(w_0{}^2 - \tilde{w}_0{}^2\right) & ; \text{for } 0 \leq x \leq \eta \\[4mm] \dfrac{1}{2\zeta}u^* + \dfrac{1}{2\lambda\zeta}\left(w_0{}^2 - \tilde{w}_0{}^2\right) & ; \text{for } \eta \leq x \leq \eta + \lambda \end{cases} \qquad (B.4)$$

155

B.2 Calculation of Membrane and Bending Energies

Because of symmetry, only half of the plate is considered in the derivation of the membrane and bending energies. The following procedure is identical to the one used in Appendix A.4 on page 140 for the case of no initial imperfections.

B.2.1 Membrane Energy

Starting from the expressions for the strain field, Eqs. (B.2), (B.3), and (B.4), and the following definition for the membrane energy,

$$U_m = \frac{Et}{2(1-v^2)} \int_S [\varepsilon_x^2 + \varepsilon_y^2 + 2v\varepsilon_x\varepsilon_y + 2(1-v)\varepsilon_{xy}^2]\, dS$$

one finds:

$$U_m = \frac{Et}{2(1-v^2)} \left[C_1\left(w_0^2 - \tilde{w}_0^2\right)^2 + C_2 u_0\left(w_0^2 - \tilde{w}_0^2\right) \right.$$
$$\left. + C_3 u^*\left(w_0^2 - \tilde{w}_0^2\right) + C_4 u^* u_0 + C_5 u^{*2} + C_6 u_0^2 \right]$$

(B.5)

As stated earlier, in this derivation we have followed the exact same steps as in Appendix A.4. Therefore here, for simplicity, the details of the derivation are omitted.

In Eq. (B.5), the parameters $C_i(\zeta)$; $(i = 1, ..., 6)$ are as follows:

$$C_1 = \frac{1}{8}\frac{\zeta}{\eta^3} + \frac{1}{8}\frac{\eta}{\zeta^3} + \frac{1}{4}\frac{1}{\eta\zeta} + \frac{1}{8}\frac{\zeta}{\lambda^3} + \frac{1}{8}\frac{\lambda}{\zeta^3} + \frac{1}{4}\frac{1}{\lambda\zeta}$$

$$C_2 = -\frac{1}{2}\frac{\zeta}{\lambda^2} - \frac{1}{2}\frac{v}{\zeta}$$

$$C_3 = -\frac{1}{2}\frac{\zeta}{\eta^2} - \frac{1}{2}\frac{\zeta}{\lambda^2}$$

$$C_4 = -\frac{\zeta}{\lambda}$$

$$C_5 = \frac{1}{2}\frac{\zeta}{\eta} + \frac{1}{4}\frac{\eta}{\zeta} - \frac{1}{4}\frac{\nu\eta}{\zeta} + \frac{1}{2}\frac{\zeta}{\lambda} + \frac{1}{4}\frac{\lambda}{\zeta} - \frac{1}{4}\frac{\nu\lambda}{\zeta}$$

$$C_6 = \frac{1}{2}\frac{\zeta}{\lambda}$$

B.2.2 Bending Energy

From the definition of the bending energy,

$$U_b = \frac{Et^3}{24(1-\nu^2)}\int_S (\kappa_x + \kappa_y)^2 dS$$

where one replaces the bending curvatures κ_x and κ_y by the following average curvatures

$$(\kappa_x)_{avg} = \begin{cases} (\kappa_{x_I})_{avg} = \dfrac{w_0 - \tilde{w}_0}{\eta^2} & ;\text{for } 0 \le x \le \eta \\[2ex] (\kappa_{x_{II}})_{avg} = \dfrac{w_0 - \tilde{w}_0}{\lambda^2} & ;\text{for } \eta \le x \le \eta + \lambda \end{cases}$$

$$(\kappa_y)_{avg} = \frac{w_0 - \tilde{w}_0}{\zeta^2}$$

the bending energy is found to be

157

$$U_b = \frac{Et^3}{24(1-v^2)} C_7 (w_0 - \tilde{w}_0)^2 \tag{B.6}$$

Here also, the details of the derivation are omitted as the procedure is similar to the one with no imperfections as described in Appendix A.4.

In Eq. (B.6), the parameter C_7 is as follows:

$$C_7 = \frac{\zeta}{\eta^3} + \frac{\eta}{\zeta^3} + \frac{2}{\zeta\eta} + \frac{\zeta}{\lambda^3} + \frac{\lambda}{\zeta^3} + \frac{2}{\lambda\zeta}$$

B.3 Load-deflection Curve

Making use of Eqs. (B.5) and (B.6), the total potential energy defined by

$$\Pi(u_0, w_0) = U_m(u_0, w_0) + U_b(u_0, w_0) - \left(\frac{P}{2}\right)u_0$$

reduces to the following expression

$$\Pi(u_0, w_0) = \frac{Et}{2(1-v^2)} \left[C_1 \left(w_0^2 - \tilde{w}_0^2 \right)^2 + C_2 u_0 \left(w_0^2 - \tilde{w}_0^2 \right) + C_3 u^* \left(w_0^2 - \tilde{w}_0^2 \right) \right.$$
$$\left. + C_4 u^* u_0 + C_5 u^{*2} + C_6 u_0^2 \right] + \frac{Et^3}{24(1-v^2)} C_7 (w_0 - \tilde{w}_0)^2 - \frac{1}{2}Pu_0$$

The stationary potential energy criteria $\delta\Pi = \frac{\partial\Pi}{\partial u_0}\delta u_0 + \frac{\partial\Pi}{\partial u^*}\delta u^* + \frac{\partial\Pi}{\partial w_0}\delta w_0 = 0$ applied to the above expression, gives rise to the following system of three nonlinear algebraic equations relating P, u_0, u^*, and w_0:

$$\frac{\partial\Pi}{\partial u_0} = 0 \Rightarrow P = \frac{Et}{1-v^2} \left[C_2 \left(w_0^2 - \tilde{w}_0^2 \right) + C_4 u^* + 2C_6 u_0 \right] \tag{B.7}$$

158

$$\frac{\partial \Pi}{\partial u^*} = 0 \Rightarrow u^* = -\frac{C_3}{2C_5}\left(w_0^{\ 2} - \tilde{w}_0^{\ 2}\right) - \frac{C_4}{2C_5}u_0 \tag{B.8}$$

and

$$\frac{\partial \Pi}{\partial w_0} = 0 \Rightarrow 4C_1 w_0\left(w_0^{\ 2} - \tilde{w}_0^{\ 2}\right) + 2C_2 u_0 w_0 + 2C_3 u^* w_0 + \frac{t^2 C_7}{6}\left(w_0 - \tilde{w}_0\right) = 0 \tag{B.9}$$

Eq. (B.8) in (B.9), and since $\tilde{w}_0 \neq 0$ and $w_0 \neq 0$ gives

$$w_0^{\ 2} - \tilde{w}_0^{\ 2} = -\frac{\left(2C_2 - \dfrac{C_3 C_4}{C_5}\right)}{\left(4C_1 - \dfrac{C_3^{\ 2}}{C_5}\right)}u_0 - \frac{t^2 C_7}{6\left(4C_1 - \dfrac{C_3^{\ 2}}{C_5}\right)}\left(1 - \frac{\tilde{w}_0}{w_0}\right) \tag{B.10}$$

which finally leads to

$$u_0 = -\frac{\left(4C_1 - \dfrac{C_3^{\ 2}}{C_5}\right)}{\left(2C_2 - \dfrac{C_3 C_4}{C_5}\right)}\left(w_0^{\ 2} - \tilde{w}_0^{\ 2}\right) - \frac{t^2}{6}\frac{C_7}{\left(2C_2 - \dfrac{C_3 C_4}{C_5}\right)}\left(1 - \frac{\tilde{w}_0}{w_0}\right) \tag{B.11}$$

Also, Eqs. (B.8) and (B.10) in expression (B.7) gives

$$P_{II} = \frac{Et}{1-v^2}\left\{\left[2C_6 - \frac{C_4^{\ 2}}{2C_5} - 2\frac{\left(C_2 - \dfrac{C_3 C_4}{2C_5}\right)^2}{\left(4C_1 - \dfrac{C_3^{\ 2}}{C_5}\right)}\right]u_0 - \frac{t^2}{6}\frac{C_7\left(C_2 - \dfrac{C_3 C_4}{2C_5}\right)}{\left(4C_1 - \dfrac{C_3^{\ 2}}{C_5}\right)}\left(1 - \frac{\tilde{w}_0}{w_0}\right)\right\} \tag{B.12}$$

From the above two expressions, the load-deflection curve with initial imperfections effect is constructed.

B.4 Non-dimensionalization of Membrane Yield Condition

In what follows, we derive a dimensionless form of the following expression (Eq. (3.10) on page 56):

$$Au_0^2 + B\left(1 - \frac{\tilde{w}_0}{w_0}\right)u_0 + \left[C\left(1 - \frac{\tilde{w}_0}{w_0}\right)^2 - \left(\frac{\sigma_0}{E}\right)^2\right] = 0 \qquad (B.13)$$

where

$$A = \begin{cases} a_1(D_1^2 + D_3^2) - a_2 D_1 D_3 + a_3 D_5^2 & ; \text{for } 0 \le x \le \eta \\ a_1(D_1^{*2} + D_3^{*2}) - a_2 D_1^* D_3^* + a_3 D_5^{*2} & ; \text{for } \eta \le x \le \eta + \lambda \end{cases}$$

$$B = \begin{cases} 2a_1(D_1 D_2 + D_3 D_4) - a_2(D_1 D_4 + D_2 D_3) + 2a_3 D_5 D_6 & ; \text{for } 0 \le x \le \eta \\ 2a_1(D_1^* D_2^* + D_3^* D_4^*) - a_2(D_1^* D_4^* + D_2^* D_3^*) \\ \quad + 2a_3 D_5^* D_6^* & ; \text{for } \eta \le x \le \eta + \lambda \end{cases}$$

$$C = \begin{cases} a_1(D_2^2 + D_4^2) - a_2 D_2 D_4 + a_3 D_6^2 & ; \text{for } 0 \le x \le \eta \\ a_1(D_2^{*2} + D_4^{*2}) - a_2 D_2^* D_4^* + a_3 D_6^{*2} & ; \text{for } \eta \le x \le \eta + \lambda \end{cases}$$

and

$$a_1 = \frac{v^2 - v + 1}{(1 - v^2)^2}$$

$$a_2 = \frac{v^2 - 4v + 1}{(1 - v^2)^2}$$

$$a_3 = \frac{3}{(1 + v)^2}$$

160

The parameters $D_i(\zeta)$; $(i = 1, ..., 6)$ and $D_i{}^*(\zeta)$; $(i = 1, ..., 6)$ are given in Appendix A.6 on page 147.

Using nondimensional parameters defined in Appendix A.5 on page 145, one gets:

$$\overline{a_1} = a_1 = \frac{v^2 - v + 1}{(1 - v^2)^2}$$

$$\overline{a_2} = a_2 = \frac{v^2 - 4v + 1}{(1 - v^2)^2}$$

$$\overline{a_3} = a_3 = \frac{3}{(1 + v)^2}$$

$$\overline{D_1} = D_1 R ; \qquad \overline{D_2} = D_2 \frac{R^2}{t^2} ; \qquad \overline{D_3} = D_3 R ;$$

$$\overline{D_4} = D_4 \frac{R^2}{t^2} ; \qquad \overline{D_5} = D_5 R ; \qquad \overline{D_6} = D_6 \frac{R^2}{t^2} ;$$

$$\overline{A} = A R^2 ; \qquad \overline{B} = B \frac{R^3}{t^2} ; \qquad \overline{C} = C \frac{R^4}{t^4} ;$$

Finally Eq. (B.13) can be rewritten as:

$$\frac{\overline{A}}{R^2} u_0{}^2 + \frac{t^2}{R^3} \overline{B} \left(1 - \frac{\tilde{w}_0}{w_0} \right) u_0 + \frac{t^4}{R^4} \overline{C} \left(1 - \frac{\tilde{w}_0}{w_0} \right)^2 - \left(\frac{\sigma_0}{E} \right)^2 = 0$$

161

multiplying both sides of the above equation by $\left(\dfrac{R}{t}\right)^4$ leads to

$$\overline{A}\left(\frac{Ru_0}{t^2}\right)^2 + \overline{B}\left(1 - \frac{\tilde{w}_0}{w_0}\right)\left(\frac{Ru_0}{t^2}\right) + \overline{C}\left(1 - \frac{\tilde{w}_0}{w_0}\right)^2 - \left(\frac{R}{t}\sqrt{\frac{\sigma_0}{E}}\right)^4 = 0$$

or

$$\overline{A}\,\overline{u}_0^{\,2} + \overline{B}\left(1 - \frac{r}{\overline{w}_0}\right)\overline{u}_0 + \left[\overline{C}\left(1 - \frac{r}{\overline{w}_0}\right)^2 - \frac{1}{\beta^4}\right] = 0 \qquad\qquad \text{(B.14)}$$

where $\beta = \dfrac{t}{R}\sqrt{\dfrac{E}{\sigma_0}}$ is the slenderness ratio parameter, $r = \dfrac{\tilde{w}_0}{t}$, and $\overline{w}_0 = \dfrac{w_0}{t}$.

162

Appendix C

Calculations Pertinent to Post-Failure Analysis

C.1 Geometric Considerations

From geometry, using Fig. C.1, we find

$$\delta = \frac{\pi}{2} \tag{C.1}$$

$$\gamma = \alpha \tag{C.2}$$

$$\beta = \frac{\pi}{2} - 2\alpha$$

$$\alpha = \frac{\rho}{R} \tag{C.3}$$

and using the expression for ρ from Appendix A.1 on page 135 into Eq. (C.3), we get:

$$\alpha\,(\zeta) = \mathrm{atan}\left(\frac{\sqrt{R^2 - \zeta^2}}{R + \zeta} \right)$$

C.2 Determination of Angles of Rotation

Referring to Fig. C.2, any section A-A, reveals a tetrahedron ABCD with characteristic angles α, β, ϕ_1, and θ_2. This tetrahedron is shown in Fig. C.3. If we make a cut in order to reveal the surface DEF in which the lines DE and EF make an angle θ_2 between each other, we end up with the tetrahedron shown in Fig. C.4. It is from this tetrahedron that the angles of rotation are determined.

From the geometry, we have:

$$x^2 = \left(\frac{a}{\cos\alpha}\right)^2 + \left(\frac{a}{\cos\beta}\right)^2 - 2\frac{a^2}{\cos\alpha\cos\beta}\cos\phi_1 \tag{C.4}$$

and

$$x^2 = (a\,\tan\alpha)^2 + (a\,\tan\beta)^2 - 2a^2\,\tan\alpha\tan\beta\cos\theta_2 \tag{C.5}$$

Combining Eqs. (C.4) and (C.5) to eliminate x^2 gives:

$$2\tan\alpha\tan\beta\cos\theta_2 = (\tan\alpha)^2 - \frac{1}{(\cos\alpha)^2} + (\tan\beta)^2 - \frac{1}{(\cos\beta)^2} + \frac{2\cos\phi_1}{\cos\alpha\cos\beta}$$

that is

$$2\tan\alpha\tan\beta\cos\theta_2 = -2 + 2\frac{\cos\phi_1}{\cos\alpha\cos\beta}$$

or

$$\sin\alpha\sin\beta\cos\theta_2 = -\cos\alpha\cos\beta + \cos\phi_1$$

and finally

$$\cos\theta_2 = \frac{\cos\phi_1 - \cos\alpha\cos\beta}{\sin\alpha\sin\beta} \tag{C.6}$$

Rotating the tetrahedron ABCD, such that the area ACD lies on the plane of the paper and performing a similar analysis, we get:

$$\cos\theta_1 = \frac{\cos\beta - \cos\phi_1\cos\alpha}{\sin\phi_1\sin\alpha} \tag{C.7}$$

Similarly, rotating the tetrahedron ABCD such that the surface ABC lies on the plane of the paper, we get:

$$\cos\theta_5 = \frac{\cos\alpha - \cos\beta\cos\phi_1}{\sin\beta\sin\phi_1} \tag{C.8}$$

Performing a similar analysis to the tetrahedron revealed by section B-B as shown in Fig. C.5 gives:

$$\cos\theta_3 = \frac{\cos\phi_2 - \cos\delta\cos\gamma}{\sin\delta\sin\gamma} \tag{C.9}$$

$$\cos\theta_4 = \frac{\cos\delta - \cos\gamma\cos\phi_2}{\sin\gamma\sin\phi_2} \tag{C.10}$$

and

$$\cos\theta_5 = \frac{\cos\gamma - \cos\phi_2\cos\delta}{\sin\phi_2\sin\delta} \tag{C.11}$$

Finally using Eqs. (C.1) and (C.2) in Eqs. (C.9) to (C.11) we get the following final result for the angles of rotation:

$$\cos\theta_1 = \frac{\cos\beta - \cos\alpha\cos\phi_1}{\sin\alpha\sin\phi_1} \tag{C.12}$$

$$\cos\theta_2 = \frac{\cos\phi_1 - \cos\alpha\cos\beta}{\sin\alpha\sin\beta} \tag{C.13}$$

$$\cos\theta_3 = \frac{\cos\phi_2}{\sin\alpha} \tag{C.14}$$

$$\cos\theta_4 = -\frac{\cos\alpha\cos\phi_2}{\sin\alpha\sin\phi_2} \tag{C.15}$$

$$\cos\theta_5 = \frac{\cos\alpha - \cos\beta\cos\phi_1}{\sin\beta\sin\phi_1} \tag{C.16}$$

and

$$\cos\theta_5 = \frac{\cos\alpha}{\sin\phi_2} \tag{C.17}$$

C.3 Membrane Work Rate

C.3.1 Flange Contribution

As seen in Fig. C.6, the flange of width H compresses a distance u_f, therefore Eq. (4.35) on page 71 becomes

$$\dot{W}_{M_{flange}} = 2N_0\int_0^H \dot{u}_f ds \tag{C.18}$$

Let us now determine $\dot{u}_f$ from geometry.

$$x_B = l_5\cos\phi_1 + l_4\cos\psi \tag{C.19}$$

$$y_B = l_5\sin\phi_1 - l_4\sin\psi \tag{C.20}$$

$$x_C = l_5\cos\phi_1 + l_4\cos\psi + \lambda\cos\left(\frac{\pi}{2} - \psi\right) \tag{C.21}$$

$$y_C = l_5\sin\phi_1 - l_4\sin\psi + \lambda\sin\left(\frac{\pi}{2} - \psi\right) \tag{C.22}$$

Also from geometry,

166

$$\psi = \pi - (\phi_1 + \phi_2) \tag{C.23}$$

Eq. (C.23) in Eqs. (C.19) through (C.22) give:

$$x_B = l_5 \cos\phi_1 - l_4 \cos(\phi_1 + \phi_2) \tag{C.24}$$

$$y_B = l_5 \sin\phi_1 - l_4 \sin(\phi_1 + \phi_2) \tag{C.25}$$

$$x_C = l_5 \cos\phi_1 - l_4 \cos(\phi_1 + \phi_2) + \lambda \sin(\phi_1 + \phi_2) \tag{C.26}$$

$$y_C = l_5 \sin\phi_1 - l_4 \sin(\phi_1 + \phi_2) - \lambda \cos(\phi_1 + \phi_2) \tag{C.27}$$

But

$$u_f = x_C - R$$

Using Eq. (C.26), we get

$$u_f = l_5 \cos\phi_1 - l_4 \cos(\phi_1 + \phi_2) + \lambda \sin(\phi_1 + \phi_2) - R$$

and differentiation with respect to time gives

$$\dot{u}_f = -l_5 \dot{\phi}_1 \sin\phi_1 + l_4 (\dot{\phi}_1 + \dot{\phi}_2) \sin(\phi_1 + \phi_2) + \lambda (\dot{\phi}_1 + \dot{\phi}_2) \cos(\phi_1 + \phi_2)$$

That is,

$$\dot{u}_f = \dot{\phi}_1 [-l_5 \sin\phi_1 + l_4 \sin(\phi_1 + \phi_2) + \lambda \cos(\phi_1 + \phi_2)]$$
$$+ \dot{\phi}_2 [l_4 \sin(\phi_1 + \phi_2) + \lambda \cos(\phi_1 + \phi_2)]$$

Now, to eliminate $\dot{\phi}_2$, one makes use of Eq. (4.26) on page 69 in the above expression. After reduction, we get

$$\dot{u}_f = \dot{\phi}_1 [-l_5\sin\phi_1 + l_4\sin(\phi_1 + \phi_2) + \lambda\cos(\phi_1 + \phi_2)] +$$

$$\dot{\phi}_1 [l_4\sin(\phi_1 + \phi_2) + \lambda\cos(\phi_1 + \phi_2)]$$

$$\left[\frac{\sin\phi_2(\cos\alpha\cos\phi_1 - \cos\beta)\sqrt{(\sin\alpha)^2 - (\cos\phi_2)^2}}{\cos\alpha\cos\phi_2\sin\phi_1\sqrt{(\sin\alpha)^2 - (\cos\beta)^2 + 2\cos\alpha\cos\beta\cos\phi_1 - (\cos\phi_1)^2}}\right]$$

That is,

$$\dot{u}_f = \dot{\phi}_1 f(\phi_1, \phi_2) \tag{C.28}$$

where

$$f(\phi_1, \phi_2) = -l_5\sin\phi_1 + l_4\sin(\phi_1 + \phi_2) + \lambda\cos(\phi_1 + \phi_2) \tag{C.29}$$

$$+ [l_4\sin(\phi_1 + \phi_2) + \lambda\cos(\phi_1 + \phi_2)]$$

$$\left[\frac{\sin\phi_2(\cos\alpha\cos\phi_1 - \cos\beta)\sqrt{(\sin\alpha)^2 - (\cos\phi_2)^2}}{\cos\alpha\cos\phi_2\sin\phi_1\sqrt{(\sin\alpha)^2 - (\cos\beta)^2 + 2\cos\alpha\cos\beta\cos\phi_1 - (\cos\phi_1)^2}}\right]$$

Finally Eq. (C.28) in (C.18) gives after integration, the following final result for the flange contribution to the membrane work rate:

$$\dot{W}_{M_{flange}} = 2N_0 H\dot{\phi}_1 f(\phi_1, \phi_2) \tag{C.30}$$

where $f(\phi_1, \phi_2)$ is given by Eq. (C.29).

C.3.2 Web Contribution

We assume that the velocity strain is distributed uniformly in the region illustrated by the shaded area in Fig. C.6, were compression occurs.

Based on this assumption, Eq. (4.35) on page 71 becomes:

$$\dot{W}_{M_{web}} = 2N_0 \int_0^s \dot{u}_{avg} ds \qquad (C.31)$$

From geometry,

$$u_{avg} = \frac{1}{2}\left(u_x + \frac{\lambda}{\lambda + \eta} u_f \right)$$

that is:

$$\dot{u}_{avg} = \frac{1}{2}\left(\dot{u}_x + \frac{\lambda}{\lambda + \eta} \dot{u}_f \right) \qquad (C.32)$$

Also, from geometry we have;

$$u_x = x_B - R = l_5 \cos\phi_1 - l_4 \cos(\phi_1 + \phi_2) - R$$

hence

$$\dot{u}_x = -l_5 \dot{\phi}_1 \sin\phi_1 + l_4 (\dot{\phi}_1 + \dot{\phi}_2) \sin(\phi_1 + \phi_2)$$

that is:

$$\dot{u}_x = \dot{\phi}_1 [-l_5 \sin\phi_1 + l_4 \sin(\phi_1 + \phi_2)] + \dot{\phi}_2 [l_4 \sin(\phi_1 + \phi_2)] \qquad (C.33)$$

Eliminating $\dot{\phi}_2$ in the same manner as done for the flange, one gets:

169

$$\dot{u}_x = \dot{\phi}_1 \left[-l_5 \sin\phi_1 + l_4 \sin(\phi_1 + \phi_2) \right] +$$

$$\dot{\phi}_1 \frac{l_4 \sin(\phi_1 + \phi_2) \sin\phi_2 (\cos\alpha\cos\phi_1 - \cos\beta) \sqrt{(\sin\alpha)^2 - (\cos\phi_2)^2}}{\cos\alpha\cos\phi_2\sin\phi_1\sqrt{(\sin\alpha)^2 - (\cos\beta)^2} + 2\cos\alpha\cos\beta\cos\phi_1 - (\cos\phi_1)^2}$$

That is,

$$\dot{u}_x = \dot{\phi}_1 \; g(\phi_1, \phi_2) \qquad\qquad\qquad (C.34)$$

where

$$g(\phi_1, \phi_2) = -l_5\sin\phi_1 + l_4\sin(\phi_1 + \phi_2) + \qquad\qquad (C.35)$$

$$\frac{l_4 \sin(\phi_1 + \phi_2) \sin\phi_2 (\cos\alpha\cos\phi_1 - \cos\beta) \sqrt{(\sin\alpha)^2 - (\cos\phi_2)^2}}{\cos\alpha\cos\phi_2\sin\phi_1\sqrt{(\sin\alpha)^2 - (\cos\beta)^2} + 2\cos\alpha\cos\beta\cos\phi_1 - (\cos\phi_1)^2}$$

Eq. (C.28) and (C.34) in Eq. (C.32) give:

$$\dot{u}_{avg} = \frac{1}{2}\left[\dot{\phi}_1 \; g(\phi_1, \phi_2) + \frac{\lambda}{\lambda + \eta}\dot{\phi}_1 f(\phi_1, \phi_2) \right]$$

That is,

$$\dot{u}_{avg} = \frac{1}{2}\dot{\phi}_1\left[g(\phi_1, \phi_2) + \frac{\lambda}{\lambda + \eta}f(\phi_1, \phi_2) \right] \qquad (C.36)$$

Finally, Eq. (C.36) in (C.31) give:

$$\dot{W}_{M_{web}} = 2N_0 \int_0^{(\lambda + \eta)} \frac{1}{2}\dot{\phi}_1 \left[g\,(\phi_1, \phi_2) + \frac{\lambda}{\lambda + \eta} f\,(\phi_1, \phi_2) \right] ds$$

and after integration leads to the following final result for the web contribution to the membrane work rate

$$\dot{W}_{M_{web}} = N_0 \dot{\phi}_1 \left[(\lambda + \eta)\,g\,(\phi_1, \phi_2) + \lambda f\,(\phi_1, \phi_2) \right] \qquad \text{(C.37)}$$

where $f(\phi_1, \phi_2)$ is given by Eq. (C.29), and $g\,(\phi_1, \phi_2)$ by Eq. (C.35).

C.4 Rate of External Work

The rate of external work is given by

$$\dot{W}_{ext} = P\dot{\Delta} \qquad \text{(C.38)}$$

From geometry, see Fig. C.6, we get

$$\Delta = R - y_C$$

Making use of Eq. (C.27), we get:

$$\Delta = R - l_5 \sin\phi_1 + l_4 \sin(\phi_1 + \phi_2) + \lambda \cos(\phi_1 + \phi_2) \qquad \text{(C.39)}$$

which after differentiation with respect to time gives,

$$\dot{\Delta} = -l_5 \dot{\phi}_1 \cos\phi_1 + l_4 (\dot{\phi}_1 + \dot{\phi}_2) \cos(\phi_1 + \phi_2) - \lambda (\dot{\phi}_1 + \dot{\phi}_2) \sin(\phi_1 + \phi_2)$$

or,

$$\dot{\Delta} = \dot{\phi}_1 \left[-l_5\cos\phi_1 + l_4\cos(\phi_1 + \phi_2) - \lambda\sin(\phi_1 + \phi_2) \right] + \dot{\phi}_2 \left[l_4\cos(\phi_1 + \phi_2) - \lambda\sin(\phi_1 + \phi_2) \right]$$

Again, eliminating $\dot{\phi}_2$ in the same manner as done in the previous section, one gets:

$$\dot{\Delta} = \dot{\phi}_1 \left[-l_5\cos\phi_1 + l_4\cos(\phi_1 + \phi_2) - \lambda\sin(\phi_1 + \phi_2) \right]$$

$$+ \dot{\phi}_1 \left[l_4\cos(\phi_1 + \phi_2) - \lambda\sin(\phi_1 + \phi_2) \right]$$

$$\left[\frac{\sin\phi_2 (\cos\alpha\cos\phi_1 - \cos\beta)\sqrt{(\sin\alpha)^2 - (\cos\phi_2)^2}}{\cos\alpha\cos\phi_2\sin\phi_1\sqrt{(\sin\alpha)^2 - (\cos\beta)^2} + 2\cos\alpha\cos\beta\cos\phi_1 - (\cos\phi_1)^2} \right]$$

That is,

$$\dot{\Delta} = \dot{\phi}_1\, h(\phi_1, \phi_2) \tag{C.40}$$

where

$$h(\phi_1, \phi_2) = -l_5\cos\phi_1 + l_4\cos(\phi_1 + \phi_2) - \lambda\sin(\phi_1 + \phi_2)$$

$$+ \left[l_4\cos(\phi_1 + \phi_2) - \lambda\sin(\phi_1 + \phi_2) \right]$$

$$\left[\frac{\sin\phi_2 (\cos\alpha\cos\phi_1 - \cos\beta)\sqrt{(\sin\alpha)^2 - (\cos\phi_2)^2}}{\cos\alpha\cos\phi_2\sin\phi_1\sqrt{(\sin\alpha)^2 - (\cos\beta)^2} + 2\cos\alpha\cos\beta\cos\phi_1 - (\cos\phi_1)^2} \right]$$

172

C.5 Crushing Force

The crushing force P is derived by equating the internal work rate to the rate of external work.

$$\dot{W}_{ext} = \dot{W}_{in} = \dot{W}_B + \dot{W}_{M_{flange}} + \dot{W}_{M_{web}} \qquad (C.41)$$

To get using Eqs. (4.27) on page 69, (C.30), and (C.37), in Eq. (C.41) the following expression

$$
\begin{aligned}
P\dot{\phi}_1 h\left(\phi_1, \phi_2\right) = {} & \frac{2M_0\dot{\phi}_1}{\sin\phi_1\sqrt{\left(\sin\alpha\right)^2 - \left(\cos\beta\right)^2 + 2\cos\alpha\cos\beta\cos\phi_1 - \left(\cos\phi_1\right)^2}} \\
& \left[\, l_1\left(\cos\beta\cos\phi_1 - \cos\alpha\right) - l_2\left(\sin\phi_1\right)^2 \right. \\
& - l_3\frac{\left(\sin\phi_2\right)^2\left(\cos\alpha\cos\phi_1 - \cos\beta\right)}{\cos\alpha\cos\phi_2} - l_4\frac{\cos\alpha\cos\phi_1 - \cos\beta}{\cos\phi_2} \\
& \left. + l_5\left(\cos\alpha\cos\phi_1 - \cos\beta\right) \right] + 2N_0 H\dot{\phi}_1 f\left(\phi_1, \phi_2\right) + \\
& N_0\dot{\phi}_1\left[\left(\lambda + \eta\right) g\left(\phi_1, \phi_2\right) + \lambda f\left(\phi_1, \phi_2\right)\right]
\end{aligned}
$$

Denoting

$$k(\phi_1, \phi_2) = \cfrac{1}{\sin\phi_1\sqrt{(\sin\alpha)^2 - (\cos\beta)^2 + 2\cos\alpha\cos\beta\cos\phi_1 - (\cos\phi_1)^2}}$$

$$\left[l_1(\cos\beta\cos\phi_1 - \cos\alpha) - l_2(\sin\phi_1)^2 \right.$$

$$- l_3\frac{(\sin\phi_2)^2(\cos\alpha\cos\phi_1 - \cos\beta)}{\cos\alpha\cos\phi_2} - l_4\frac{\cos\alpha\cos\phi_1 - \cos\beta}{\cos\phi_2}$$

$$\left. + l_5(\cos\alpha\cos\phi_1 - \cos\beta) \right]$$

(C.42)

the above expression reduces to:

$$Ph(\phi_1, \phi_2) = 2M_0 k(\phi_1, \phi_2) + 2N_0 Hf(\phi_1, \phi_2) + N_0(\lambda + \eta) g(\phi_1, \phi_2) + N_0\lambda f(\phi_1, \phi_2)$$

That is

$$P = 2M_0\frac{k(\phi_1, \phi_2)}{h(\phi_1, \phi_2)} + N_0(2H + \lambda)\frac{f(\phi_1, \phi_2)}{h(\phi_1, \phi_2)} + N_0(\lambda + \eta)\frac{g(\phi_1, \phi_2)}{h(\phi_1, \phi_2)} \qquad (C.43)$$

C.6 Non-dimensionalization

In what follows we derive a dimensionless form of Eq. (C.43).

Staring from the dimensionless parameters defined in Section 2.3 on page 21, that is:

$$\bar{\zeta} = \frac{\zeta}{R}; \qquad \bar{P} = \frac{PR}{D}; \qquad \bar{\Delta} = \frac{\Delta R}{t^2};$$

where

$$D = \frac{Et^3}{12(1 - v^2)}$$

174

To get

$$\tan \alpha = \frac{\sqrt{R^2 - \zeta^2}}{R + \zeta} = \frac{\sqrt{1 - \bar{\zeta}^2}}{1 + \bar{\zeta}} \qquad (C.44)$$

$$\beta = \frac{\pi}{2} - 2\alpha \qquad (C.45)$$

$$\bar{l}_1 = \frac{l_1}{R} = \frac{R}{R} = 1 \quad ; \qquad \bar{l}_1 = 1 \qquad (C.46)$$

$$\bar{l}_2 = \frac{l_2}{R} = \frac{R\sqrt{\dfrac{2R}{R+\zeta}}}{R} = \sqrt{\frac{2}{1+\bar{\zeta}}} \quad ; \qquad \bar{l}_2 = \sqrt{\frac{2}{1+\bar{\zeta}}} \qquad (C.47)$$

$$\bar{l}_3 = \frac{l_3}{R} = \frac{\zeta\sqrt{\dfrac{2R}{R+\zeta}}}{R} = \bar{\zeta}\sqrt{\frac{2}{1+\bar{\zeta}}} \quad ; \qquad \bar{l}_3 = \bar{\zeta}\sqrt{\frac{2}{1+\bar{\zeta}}} \qquad (C.48)$$

$$\bar{l}_4 = \frac{l_4}{R} = \frac{\zeta}{R} = \bar{\zeta} \quad ; \qquad \bar{l}_4 = \bar{\zeta} \qquad (C.49)$$

$$\bar{l}_5 = \frac{l_5}{R} = \frac{\sqrt{2R(R-\zeta)}}{R} = \sqrt{2(1-\bar{\zeta})} \quad ; \qquad \bar{l}_5 = \sqrt{2(1-\bar{\zeta})} \qquad (C.50)$$

$$\bar{\lambda} = \frac{\lambda}{R} = \frac{R - \sqrt{R^2 - \zeta^2}}{R} = 1 - \sqrt{1 - \bar{\zeta}^2} \quad ; \qquad \bar{\lambda} = 1 - \sqrt{1 - \bar{\zeta}^2} \qquad (C.51)$$

$$\bar{\eta} = \frac{\eta}{R} = \frac{\dfrac{\zeta\sqrt{R^2 - \zeta^2}}{R+\zeta}}{R} = \frac{\bar{\zeta}\sqrt{1 - \bar{\zeta}^2}}{1+\bar{\zeta}} \quad ; \qquad \bar{\eta} = \frac{\bar{\zeta}\sqrt{1 - \bar{\zeta}^2}}{1+\bar{\zeta}} \qquad (C.52)$$

$$\bar{\Delta} = \left(\frac{R}{t}\right)^2 [1 - \bar{l}_5 \sin\phi_1 + \bar{l}_4 \sin(\phi_1 + \phi_2) + \bar{\lambda}\cos(\phi_1 + \phi_2)]$$

Define:

$$\bar{R} = \frac{R}{t} \qquad (C.53)$$

hence

175

$$\overline{\Delta} = \overline{R}^2 \left[1 - \overline{l}_5 \sin\phi_1 + \overline{l}_4 \sin(\phi_1 + \phi_2) + \overline{\lambda}\cos(\phi_1 + \phi_2) \right] \qquad \text{(C.54)}$$

$$\tan\phi_2 = \frac{\left(\dfrac{\cos\alpha \sin\beta \sin\phi_1}{\cos\alpha - \cos\beta \cos\phi_1} \right)}{\sqrt{1 - \left(\dfrac{\cos\alpha \sin\beta \sin\phi_1}{\cos\alpha - \cos\beta \cos\phi_1} \right)^2}} \qquad \text{(C.55)}$$

$$\overline{f(\phi_1, \phi_2)} = \frac{f(\phi_1, \phi_2)}{R}$$

Therefore,

$$\overline{f(\phi_1, \phi_2)} = -\overline{l}_5 \sin\phi_1 + \overline{l}_4 \sin(\phi_1 + \phi_2) + \overline{\lambda}\cos(\phi_1 + \phi_2) \qquad \text{(C.56)}$$

$$+ \left[\overline{l}_4 \sin(\phi_1 + \phi_2) + \overline{\lambda}\cos(\phi_1 + \phi_2) \right]$$

$$\left[\frac{\sin\phi_2 (\cos\alpha \cos\phi_1 - \cos\beta) \sqrt{(\sin\alpha)^2 - (\cos\phi_2)^2}}{\cos\alpha \cos\phi_2 \sin\phi_1 \sqrt{(\sin\alpha)^2 - (\cos\beta)^2 + 2\cos\alpha \cos\beta \cos\phi_1 - (\cos\phi_1)^2}} \right]$$

$$\overline{g(\phi_1, \phi_2)} = \frac{g(\phi_1, \phi_2)}{R}$$

Therefore,

$$\overline{g(\phi_1, \phi_2)} = -\overline{l}_5 \sin\phi_1 + \overline{l}_4 \sin(\phi_1 + \phi_2) + \qquad \text{(C.57)}$$

$$\frac{\overline{l}_4 \sin(\phi_1 + \phi_2) \sin\phi_2 (\cos\alpha \cos\phi_1 - \cos\beta) \sqrt{(\sin\alpha)^2 - (\cos\phi_2)^2}}{\cos\alpha \cos\phi_2 \sin\phi_1 \sqrt{(\sin\alpha)^2 - (\cos\beta)^2 + 2\cos\alpha \cos\beta \cos\phi_1 - (\cos\phi_1)^2}}$$

$$\overline{h(\phi_1, \phi_2)} = \frac{h(\phi_1, \phi_2)}{R}$$

Therefore,

$$\overline{h(\phi_1, \phi_2)} = -\overline{l_5}\cos\phi_1 + \overline{l_4}\cos(\phi_1 + \phi_2) - \overline{\lambda}\sin(\phi_1 + \phi_2) \tag{C.58}$$

$$+ \left[\overline{l_4}\cos(\phi_1 + \phi_2) - \overline{\lambda}\sin(\phi_1 + \phi_2)\right]$$

$$\left[\frac{\sin\phi_2\,(\cos\alpha\cos\phi_1 - \cos\beta)\sqrt{(\sin\alpha)^2 - (\cos\phi_2)^2}}{\cos\alpha\cos\phi_2\sin\phi_1\sqrt{(\sin\alpha)^2 - (\cos\beta)^2 + 2\cos\alpha\cos\beta\cos\phi_1 - (\cos\phi_1)^2}}\right]$$

$$\overline{k(\phi_1, \phi_2)} = \frac{k(\phi_1, \phi_2)}{R}$$

Therefore,

$$\overline{k(\phi_1, \phi_2)} = \frac{1}{\sin\phi_1\sqrt{(\sin\alpha)^2 - (\cos\beta)^2 + 2\cos\alpha\cos\beta\cos\phi_1 - (\cos\phi_1)^2}} \tag{C.59}$$

$$\left[\overline{l_1}(\cos\beta\cos\phi_1 - \cos\alpha) - \overline{l_2}(\sin\phi_1)^2\right.$$

$$-\overline{l_3}\frac{(\sin\phi_2)^2(\cos\alpha\cos\phi_1 - \cos\beta)}{\cos\alpha\cos\phi_2} - \overline{l_4}\frac{\cos\alpha\cos\phi_1 - \cos\beta}{\cos\phi_2}$$

$$\left. + \overline{l_5}(\cos\alpha\cos\phi_1 - \cos\beta)\right]$$

$$\overline{P} = \frac{PR}{D} = \frac{12(1 - \nu^2)R}{Et^3}\,P$$

And making use of Eq. (C.43), we get

$$\overline{P} = \frac{12(1 - \nu^2)R}{Et^3}\left[2M_0\frac{\overline{k(\phi_1, \phi_2)}}{\overline{h(\phi_1, \phi_2)}} + N_0(2H + \overline{\lambda})\frac{\overline{f(\phi_1, \phi_2)}}{\overline{h(\phi_1, \phi_2)}} + N_0R(\overline{\lambda} + \overline{\eta})\frac{\overline{g(\phi_1, \phi_2)}}{\overline{h(\phi_1, \phi_2)}}\right]$$

177

Define,

$$\bar{H} = \frac{H}{R} \tag{C.60}$$

and use:

$$M_0 = \frac{\sigma_0 t^2}{4} \qquad \text{and} \qquad N_0 = \sigma_0 t$$

where σ_0 is the material flow stress, to get

$$\bar{P} = \frac{12(1-v^2)R}{Et^3}\left[2\frac{\sigma_0 t^2}{4}\frac{\overline{k(\phi_1,\phi_2)}}{h(\phi_1,\phi_2)} + \sigma_0 tR(2\bar{H}+\bar{\lambda})\frac{\overline{f(\phi_1,\phi_2)}}{h(\phi_1,\phi_2)}\right.$$
$$\left. + \sigma_0 tR(\bar{\lambda}+\bar{\eta})\frac{\overline{g(\phi_1,\phi_2)}}{h(\phi_1,\phi_2)}\right]$$

that is

$$\bar{P} = 12(1-v^2)\left[\frac{1}{2}\frac{\sigma_0 R}{Et}\frac{\overline{k(\phi_1,\phi_2)}}{h(\phi_1,\phi_2)} + \frac{\sigma_0 R^2}{Et^2}(2\bar{H}+\bar{\lambda})\frac{\overline{f(\phi_1,\phi_2)}}{h(\phi_1,\phi_2)}\right. \tag{C.61}$$
$$\left. + \frac{\sigma_0 R^2}{Et^2}(\bar{\lambda}+\bar{\eta})\frac{\overline{g(\phi_1,\phi_2)}}{h(\phi_1,\phi_2)}\right]$$

Multiply and divide the right hand side of the above equation by σ_Y (material yield strength) and use Eq. (C.53) along with the following new dimensionless parameter

$$\bar{\sigma} = \frac{\sigma_0}{\sigma_Y} \tag{C.62}$$

to finally get:

178

$$\bar{P} = \frac{12\bar{\sigma}(1-v^2)}{\beta^2\overline{h(\phi_1,\phi_2)}}\left[\frac{1}{2R}\overline{k(\phi_1,\phi_2)} + (2\bar{H}+\bar{\lambda})\overline{f(\phi_1,\phi_2)} + (\bar{\lambda}+\bar{\eta})\overline{g(\phi_1,\phi_2)}\right] \quad \text{(C.63)}$$

where $\beta = \dfrac{t}{R}\sqrt{\dfrac{E}{\sigma_Y}}$ is the slenderness ratio parameter as introduced in Section 2.7 on page 30.

C.7 Geometric Limitations

A geometric limitation should be imposed on the crushing process. The degree of free-dom for the process is exhausted when hinge line four is about to move out-of-plane. Our model is valid up to that point. This limit occurs when the fourth hinge line rotation angle θ_4 reaches $\dfrac{\pi}{2}$.

From Eq. (C.15), one gets

$$\phi_{2min} = \frac{\pi}{2}$$

which in turn using Eq. (4.28) on page 69 gives

$$(\cos\alpha\sin\beta)\,\sin\phi_{1min} + (\cos\beta)\,\cos\phi_{1min} - \cos\alpha = 0 \quad \text{(C.64)}$$

Set:

$A = \cos\alpha\sin\beta$

$B = \cos\beta$

$C = -\cos\alpha$

and define:

$t = \tan\left(\dfrac{\phi_{1min}}{2}\right)$; which implies that $\cos\phi_{1min} = \dfrac{1-t^2}{1+t^2}$ and $\sin\phi_{1min} = \dfrac{2t}{1+t^2}$

to reduce Eq. (C.64) to the following quadratic equation

$$(C - B) t^2 + 2At + (C + B) = 0$$

The root of the above expression that ensures, $\phi_{1min} < \dfrac{\pi}{2}$, $\alpha < \dfrac{\pi}{2}$, and $\beta < \dfrac{\pi}{2}$ is

$$t = \frac{\cos\alpha\sin\beta + \cos\beta\sin\alpha}{\cos\alpha + \cos\beta}$$

from which ϕ_{1min} is found as follows:

$$\phi_{1min} = 2\operatorname{atan}\left(\frac{\cos\alpha\sin\beta + \cos\beta\sin\alpha}{\cos\alpha + \cos\beta}\right) \tag{C.65}$$

The other geometrical limit ϕ_{1max} is found at the instant when the second and third hinge lines are just about to move out-of-plane. That is

$$\phi_{1max} = \alpha + \beta \tag{C.66}$$
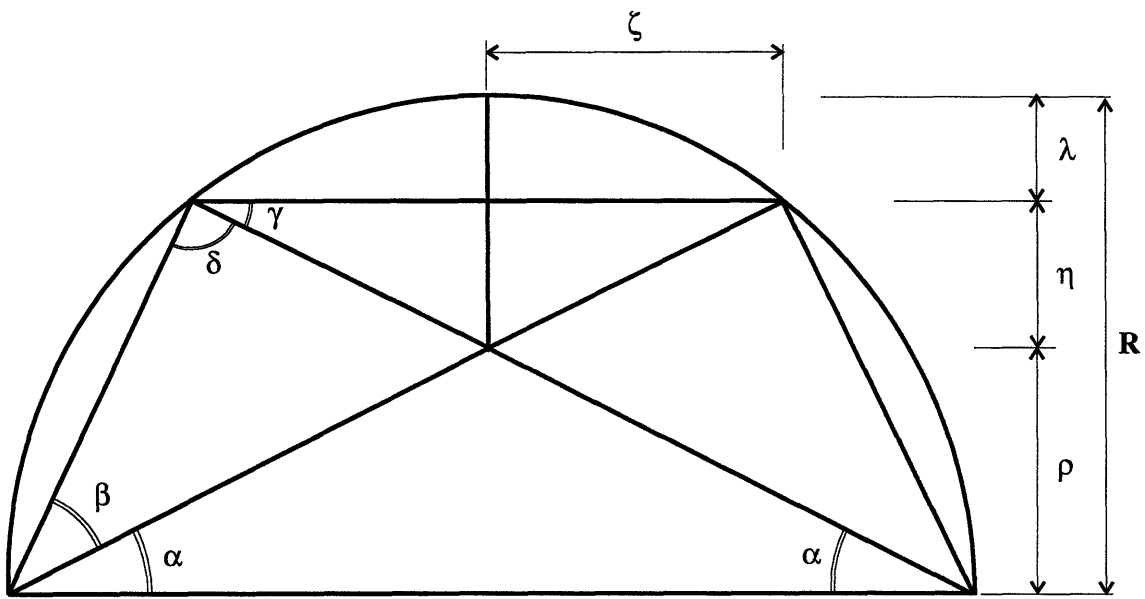
Figure C.1: Geometric Considerations
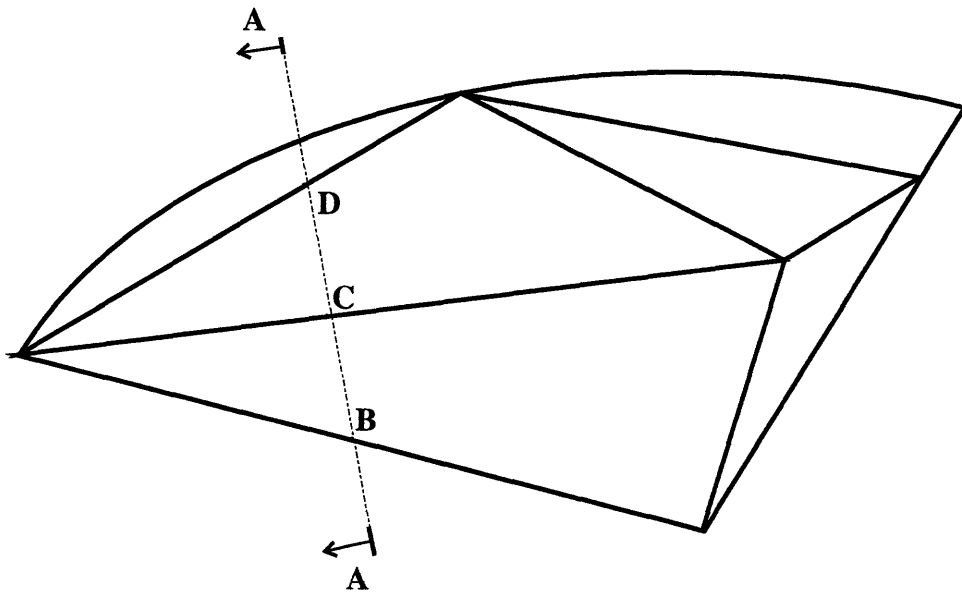
Figure C.2: Tetrahedron Used in the Bending Calculation

181
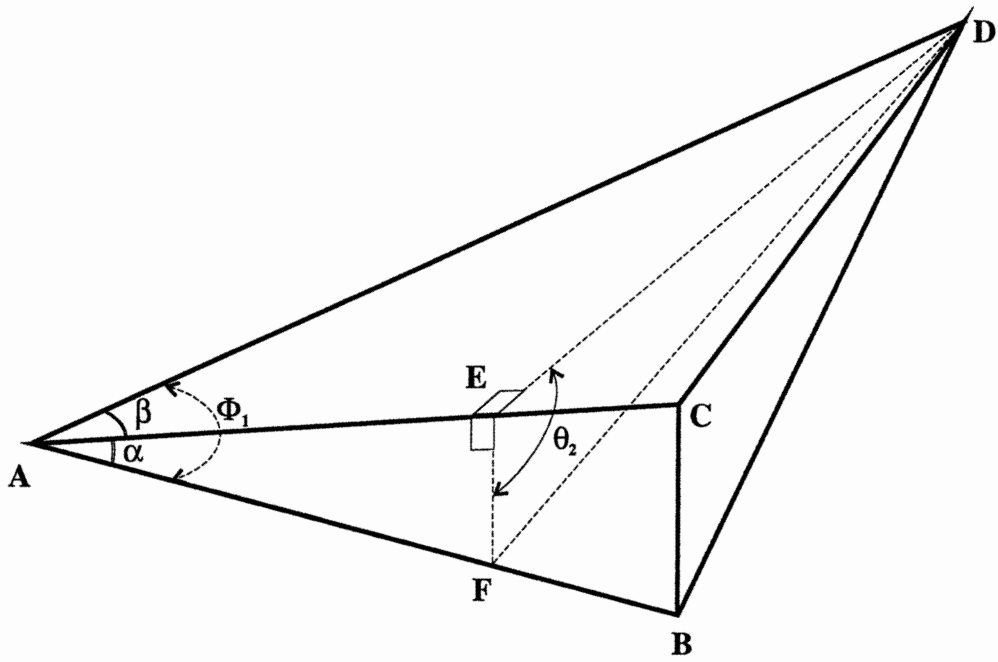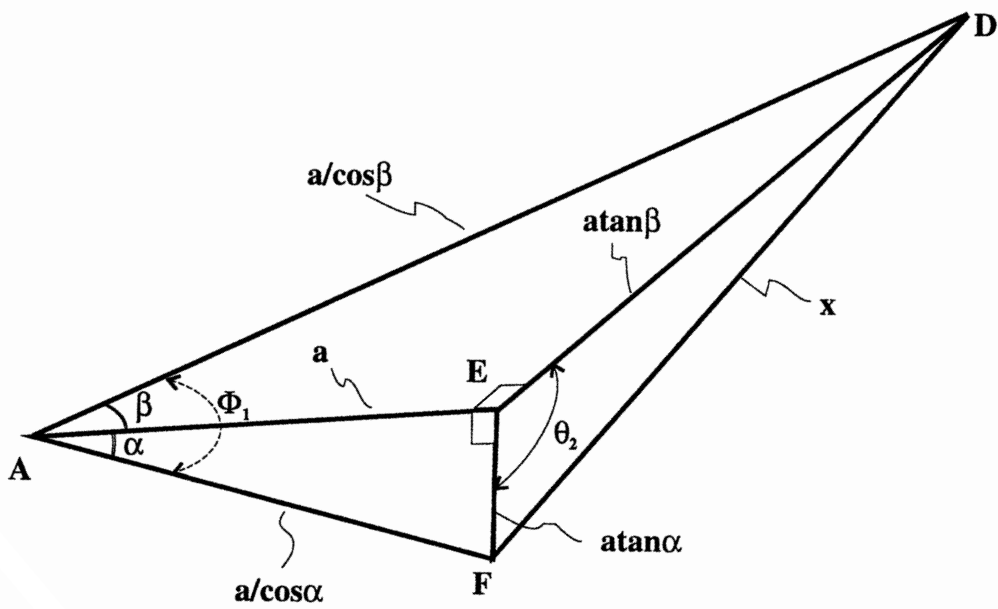
Figure C.3: Close-up of the Tetrahedron

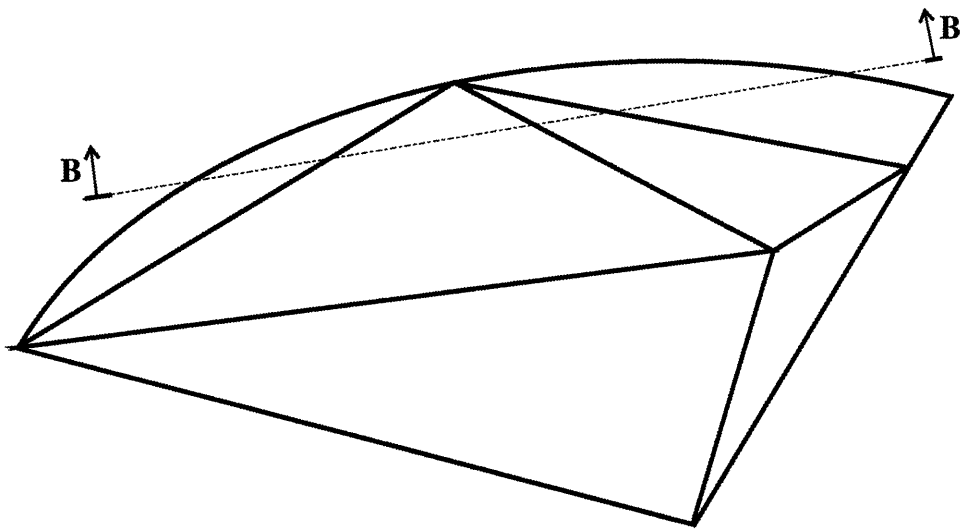**Figure C.4:** Left Side of the Tetrahedron

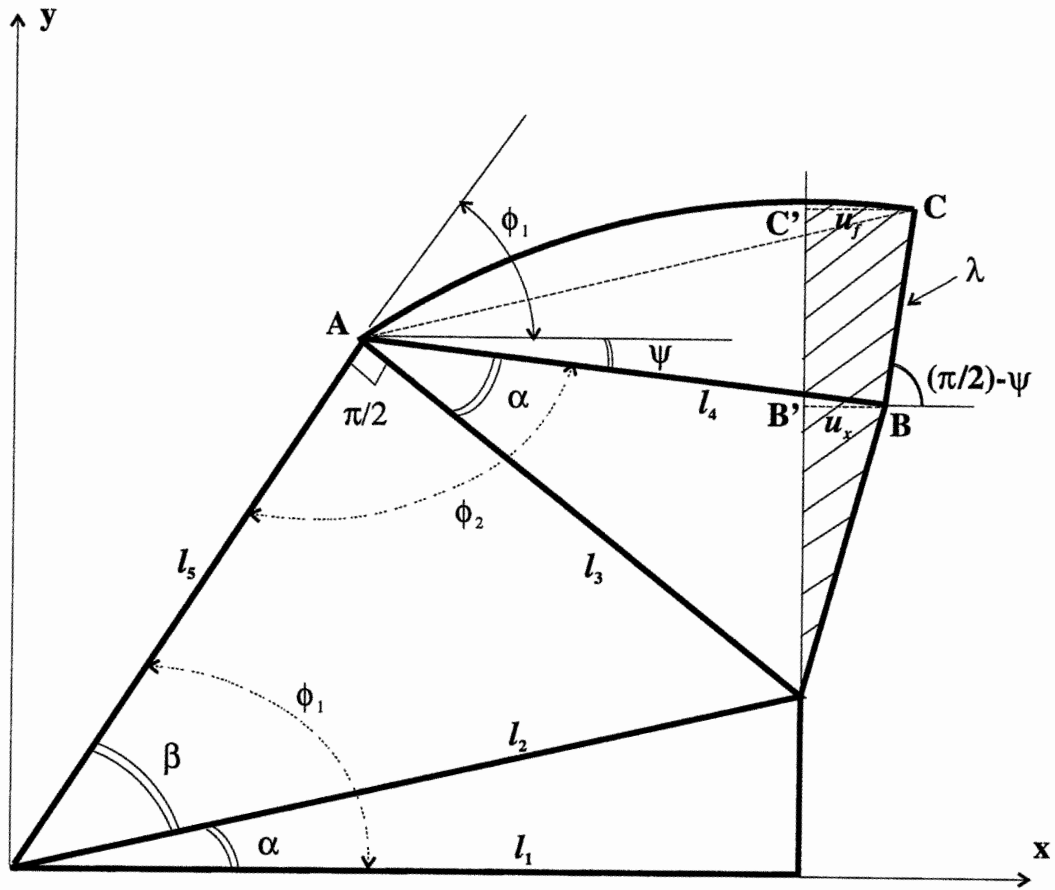**Figure C.5:** Another Tetrahedron Used in the Bending Calculation

Figure C.6: Geometry of the Problem

Appendix D

Calculations Pertinent to Experimental Study

D.1 Determination of Radius-to-thickness Ratio

The purpose is to find a practical range of radius to thickness ratio R/t. For this we use the average ratio of three typical ships.

1) San Clemente (class of ships):

89,700 DWT, Longitudinally framed double bottom only (Not double sided).

From Fig. D.1, we have bilge area radius R=8'-3", plating thickness t_p=0.875", and transverse frame thickness t_{TF}=0.52".

Average frame/plating thickness:

$$t = \frac{t_p + t_{TF}}{2} = \frac{0.875 + 0.52}{2} = 0.6975"$$

And,

$$\frac{R}{t} = \frac{99}{0.6975} = 141.93 \Rightarrow \frac{R}{t} \approx 142$$

185

2) Chevron Oregon (Actual ship name):

At typical transverse oil tight bulkhead (see Figs. D.2 and D.3), we have the average thickness of the plate (this is done because the plate thickness is missing from the drawing) to be

$$tp = \frac{0.82 + 0.88}{2} = 0.85$$

And the average bulkhead/plating thickness is:

$$t = \frac{t_p + t_{BHD}}{2} = \frac{0.85 + 0.46}{2} = 0.655"$$

Hence,

$$\frac{R}{t} = \frac{84}{0.655} = 128.2 \Rightarrow \frac{R}{t} \approx 128$$

3) Paul Buck (Class of ships, T5 tankers):

41,584 DWT. Conventional Double Hull

From Fig. D.4, we have:

Average frame/plating thickness:

$$t = \frac{t_p + t_{TF}}{2} = \frac{0.58 + 0.47}{2} = 0.525"$$

And,

$$\frac{R}{t} = \frac{72.5}{0.525} = 138.09 \Rightarrow \frac{R}{t} \approx 138$$

186

Table D.1 summarizes the radii-to-thickness ratios for the bilge areas of the three ships.

Table D.1: Radius-to-thickness Ratios

Vessel	R/t	Average R/t
San Clemente	142	
Chevron Oregon	128	136
Paul Buck	138	

In designing the specimen the target radius-to-thickness ratio is the calculated average:

$$\frac{R}{t} = 136$$

D.2 Aircraft Fuselage and Submarines R/t Ratios

A typical aircraft or submarine bulkhead is very complex and contains numerous details. Although many items, such as brackets, are primarily for local effects they still contribute to the overall crushing strength. However, for the target scale ratio of the specimen, many of theses details were not practical. The issue was resolved by smearing (area-wise) all the details and including their effect via an equivalent thickness. This leads an order of magnitude of the radius-to-thickness ratio, $\frac{R}{t}$, in submarines and aircraft as follows:

$$\frac{R}{t} \approx 198 \text{, for submarines.}$$

$$\frac{R}{t} \approx 210 \text{, for aircraft.}$$

These results are based on rough estimates made from data found in Lusted *et al.* (1994) for submarines, and in Torenbeek (1982) for aircraft.

D.3 Operation of the Test Equipment

D.3.1 Instron Test Machine Preparation

All experiments were performed on a 20,000 lb capacity (model TTDL), screw-driven, universal test machine. The test machine lacks documentation and calibration procedures was required prior to conducting any experiments. A major concern was the validity of the different test ranges offered by the Instron machine. Test ranges available were: 500, 1000, 2000, 4000, 10000, and 20000 lbs. Connecting a voltmeter to the output jack, the various calibration and offset values at each of the different load scales were observed and the system was tested to assure linearity of output data.

Another issue of concern was the calibration procedures used to set the zero and full load voltages at each load scale. In the past, the Instron has been calibrated using a chart recorder and eye judgment. the chart recorder, however, has been previously damaged and repaired. since the machine is no longer supported by the manufacturer, the chart recorders accuracy is suspect. to avoid using the chart recorder as the calibration method, the Instron output required validation against a known load cell. This would allow validation of a calibration using output voltages and the ZERO and CALIBRATION features of the machine.

The accuracy of the crosshead speed was also important. The Instron machine does not monitor displacement with time. Maxwell (1993) performed a check on the crosshead displacement with a dial indicator and found the accuracy within ±4%. A repeat test was performed that correlated well and considered adequate for this set of experiments.

To test the linearity of the load cell output and the accuracy of the test machine and calibration technique, a 1,000 lb load cell was secured to the crosshead and Instron load cell for a tension test. The calibration of the 1,000 lb load cell was known from previous calibration tests. The load scale selected was 500 lbs. Using the ZERO button, the no load output voltage of the Instron was set at 0.0V. By depressing the CALIBRATION button and adjusting the adjoinnig knob, the full load (500 lb) voltage was set at 2.0V. The load cells were connected to separate voltmeters and data was taken manually. Testing consisted of applying a small crosshead displacement and recording the Instron and attached load cell output voltages. No gain or signal conditioning was conducted on either output with the exception of the 1 Hz filter on the Instron output. The test range was 0 to 1,000 lbs (or 0 to 4V) on the Instron to allow verification of linear output at twice the set load scale. Values were recorded in both the ascending (increasing tension) and descending operations. An analysis of the obtained data, showed linearity was well established with errors in both the ascending and descending operations of less than 0.5%.

Also, the error between the expected value of 2.0 V at 500 lbs on the Instron and that actually measured is less than 1%. This is acceptable for the experiment and the Instron was calibrated based on this test in all subsequent experiments. Specific calibration procedures are detailed in the next section.

D.3.2 Instron Test Machine Operation

The Instron machine requires at least 30 minute warm-up period. Both the AMPLI-DYNE and MAIN POWER switches must be energized to begin this period. The machine settings were arranged as outlined in Yahiaoui *et al.* (1994). It is recommended that the test machine be set up in the proper configuration before energizing the machine.

To initially calibrate the universal testing machine, connect the 1 Hz output line to a voltmeter set to receive at least 2V DC. Set the load scale to 500 lbs and adjust the ZERO control knob until the output is 0V. Depress the CALIBRATION button to see what the output voltage value is for 500 lbs. Holding the CALIBRATION button depressed, adjust the CALIBRATION control knob until the voltmeter reads 2.0V. Recheck the zero setting and repeat the above steps until there is no change in the two settings. Increase the load scale to 1,000 lbs and re-zero the machine as above. Depressing the CALIBRATION button should now read 1.0V. Therefore, 1V is equal to a 500 lb force. Repeat this procedure until the appropriate load scale is reached. For example, at the 10,000 lb scale, the calibration with a zero offset should read 0.1V indicating 0.1V equals 500 lbs and 2V equals a 10,000 lb load. This terminates the calibration procedure.

D.4 Determination of the Stiffness of the Instron Machine

In order to determine the influence of the Instron machine stiffness on the recorded data, a test has been conducted. The test was configured in the same manner as the three crush tests. However, instead of the specimen, we lied on the machine cross-head a steel cylindrical rod of 3 in. diameter. The rod was oriented such that its axis and the axis of the indenter were at right angles (see Fig. D.5). As shown in the figure, we denote the diameter of the indenter by D2 and the displacement of its center by y_{D2}. The rod's diameter is denoted by D1 and the displacement of its center by y_{D1}. Finally, the displacement of the point of contact is referred to as $y_{contact}$. Fig. D.6 is the experimental data from the indenter's radius of 2 in.

In what follows, we show how we use this information to correct the experimental results of the bulkhead tests. We do this for the case where the indenter's radius is 2 in. and only for the point of peak load in the second bulkhead test.

At the Peak load, $P=10,983$ Newtons, the recorded screw motion for the bulkhead test was 1.735 mm. From this value, to get the real specimen displacement, one needs to subtract the deflection of the Instron machine. This deflection, at the load P=10,983 Newtons, is found from the stiffness test.

From Fig. D.6, one gets the recorded screw motion during the stiffness test at the operating load P=10,983 Newtons. The value is 1.695 mm. From this value we subtract the theoretical deflection $(y_{contact} - y_{D1})$ = $0.035mm$, found as described in Raymond and Young (1975). In the formula given in the reference, the young modulus of the indenter is assumed to be infinite in order to have a theoretical magnitude of the real displacement of the rod.

In summary, the displacement of the Instron machine is 1.66 mm which when subtracted from the screw motion for the bulkhead test leads the following value for the real displacement of the specimen:

$$Specimen\ Displacement\ =\ 0.075mm$$

D.5 Determination of Initial Imperfections magnitude

A non-contact laser displacement sensor was used to measure the magnitude of the specimen initial imperfections caused by welding distortions. The main features of the laser displacement sensor used in this experiment are shown in Table D.2.

Table D.2: Main Features of the Laser Displacement Sensor

Maker	KEYENCE Corporation
Sensor Head Model	LB-081
Controller Model	LB-1101
Light Source	Semi-conductor Laser Wave Length: 780 nm
Reference Distance	80 mm
Measuring Range	$\pm 15mm$
Linearity	0.25% of F.S.
Resolution	8 μm
Response Frequency	36 Hz

The KEYENCE laser displacement sensor, model LB-081, is a high accuracy measurement device which operates under fuzzy logic control.

A 486 PC compatible microcomputer was used to collect the data from the laser displacement sensor via an analog to digital converter. Measurements of out-of-plane initial imperfections were made at several locations. As shown in Fig. D.7, initial imperfections of the order of 4 mm (about 3.5 the thickness of the specimen) were detected. For the interested reader, Goktug (1994) gives a good description of the principles of the non-contact laser displacement used in this investigation.

This experiment was conducted in order to establish a reasonable estimate of the initial imperfections magnitude of the tests specimen. This estimate is used when comparing the theoretical findings with the experimental results.

D.6 Tensile Test Results

Tensile tests results are reported here for the two material thickness used in fabrication of the flanged semi-circular and rectangular specimens (Yahiaoui *et. al.*, 1994).

A total of eight specimens were tested: four for each thickness with two each in the transverse and longitudinal direction to the roll axis. The tests were conducted in accordance with ASTM specifications A370. The test specimen dimensions are shown in Fig. D.8. The reported results include yield strength (YS), tensile strength (TS), percent elongation, and the accompanying engineering stress-strain curves, as shown in Table D.3 and Figs. D.9 to D.16.

Table D.3: Tensile Test Specimen Properties

Specimen No.	Thickness (mm)	Orientation (from roll axis)	0.2% YS (N/mm^2)	TS (N/mm^2)	% Elongation
1	0.749	0°	244.8	328.9	41.3
2	0.749	0°	180.0	329.6	41.0
3	0.749	90°	175.8	319.9	41.3
4	0.749	90°	176.5	319.2	39.4
5	1.130	90°	211.7	332.3	38.5
6	1.130	90°	213.1	334.4	37.3
7	1.130	0°	229.6	338.5	38.0
8	1.130	0°	207.5	333.7	38.5

Conversion Factor: $0.006895 \ (N/mm^2) = 1 psi$

The results of Table D.3 can be averaged for each thickness as shown in Table D.4.

Table D.4: Tensile Test Specimen Averaged Properties

Thickness (mm)	Average 0.2% YS (N/mm^2)	Average TS (N/mm^2)	Average % Elongation
0.749	194.3	324.4	40.8
1.130	215.5	334.8	38.1

Figure D.1: San Clemente

Figure D.2: Chevron Oregon I

Figure D.3: Chevron Oregon II

197

Figure D.4: Paul Buck
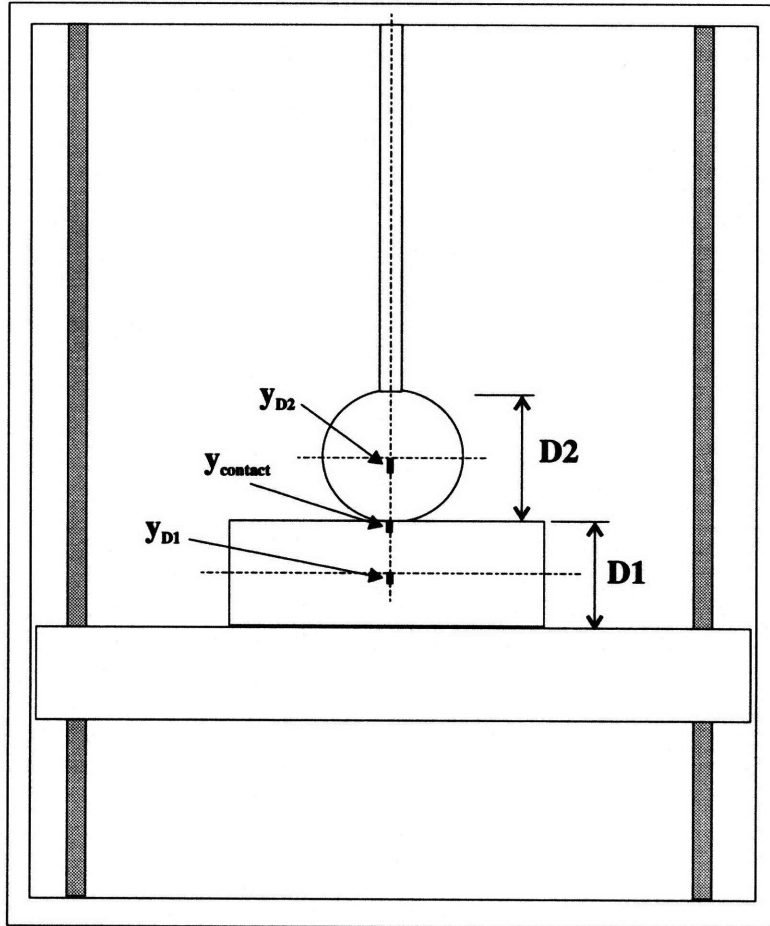
Figure D.5: Experimental Set-up
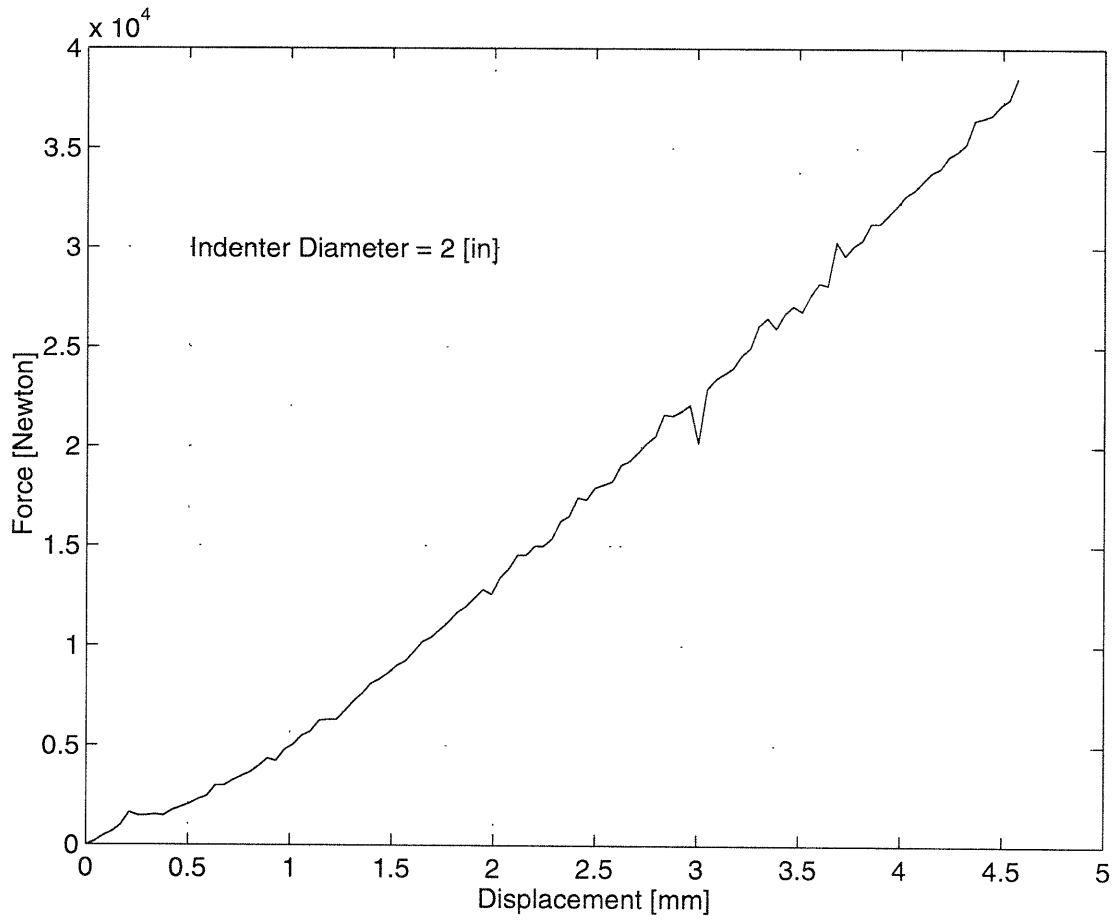
Figure D.6: Instron Machine Stiffness Experiment
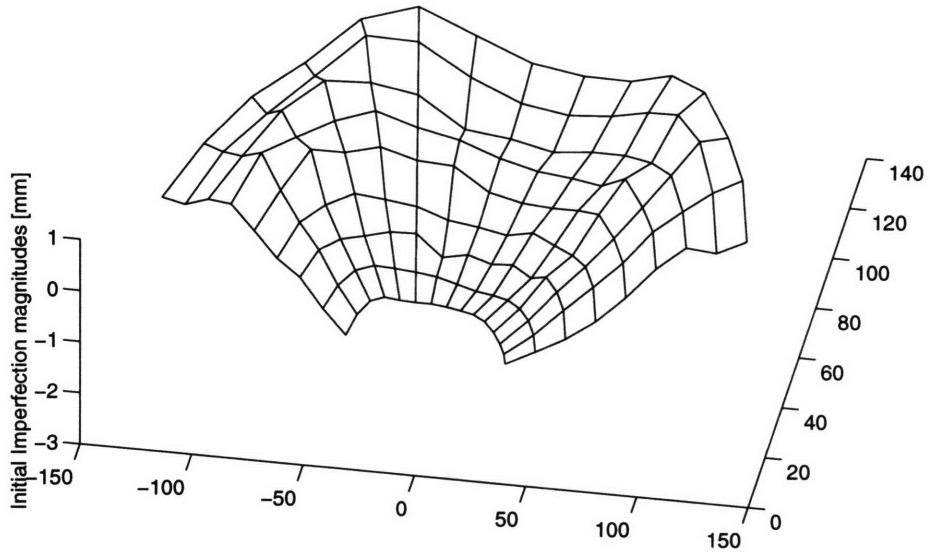
(a) Grid View
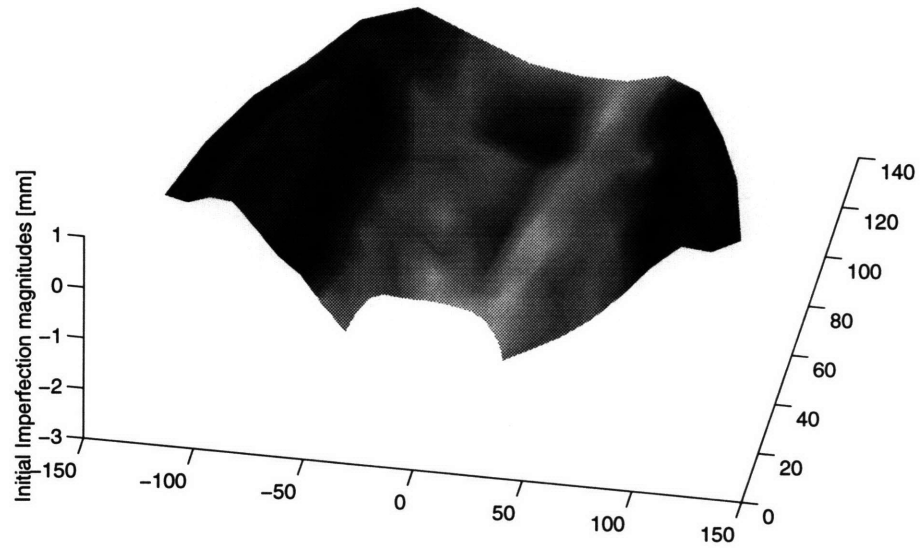
(b) Surface View

Figure D.7: Measured Initial Imperfections
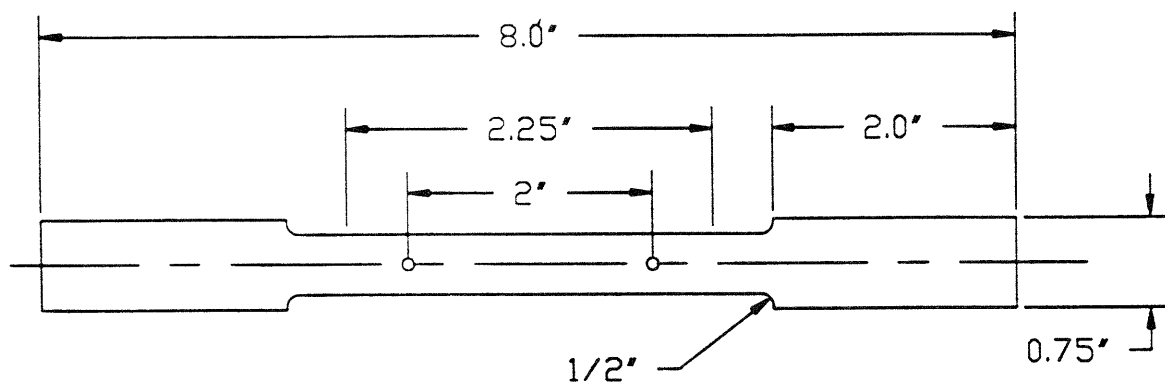
Figure D.8: ASTM A370 Flat Tensile Specimen
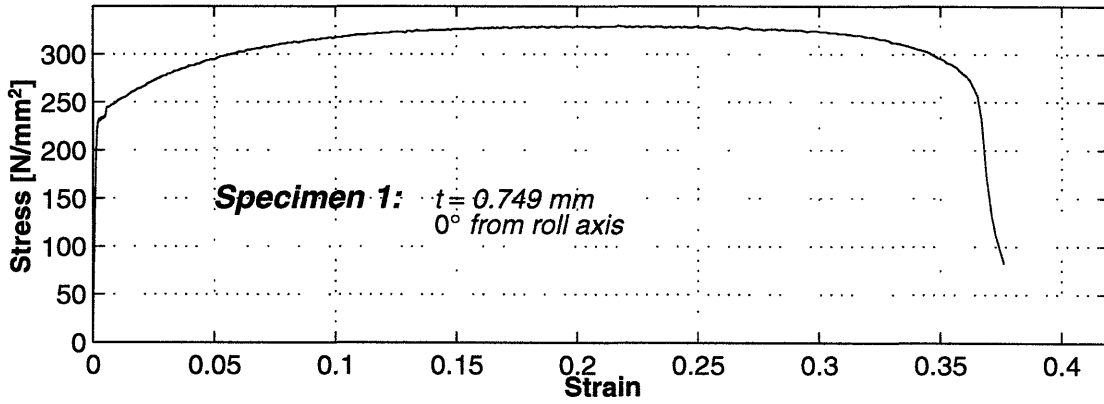
Figure D.9: Engineering Stress-Strain Curve for Specimen 1
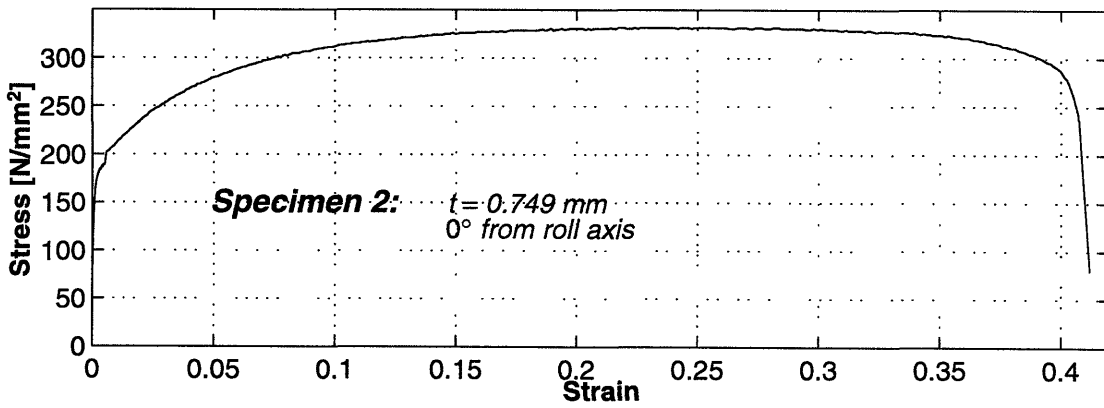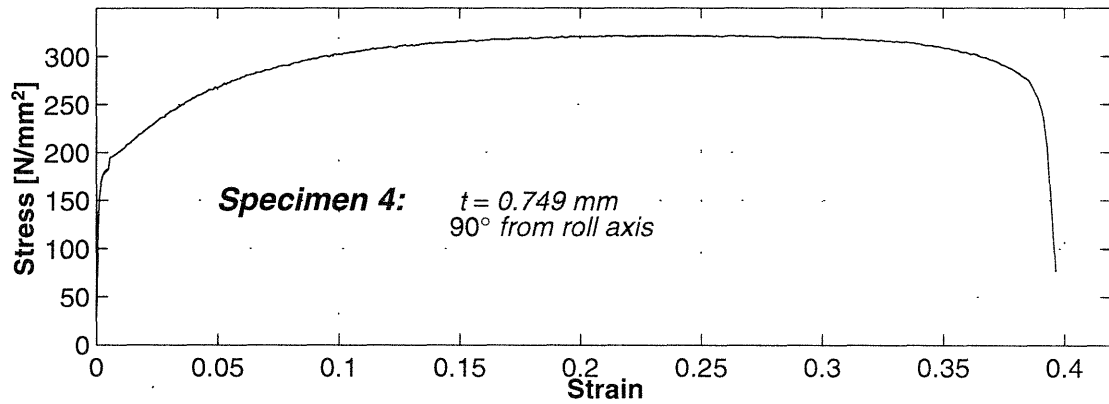

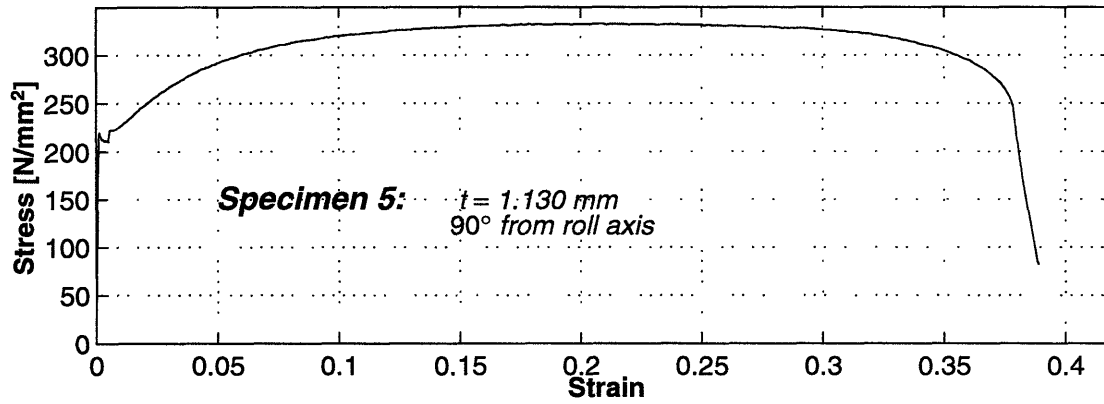**Figure D.10:** Engineering Stress-Strain Curve for Specimen 2
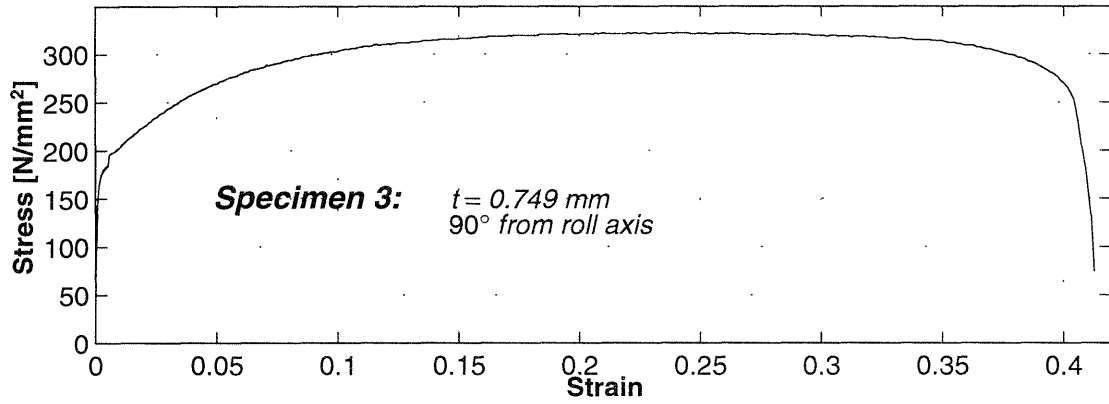
Figure D.11: Engineering Stress-Strain Curve for Specimen 3

Figure D.12: Engineering Stress-Strain Curve for Specimen 4

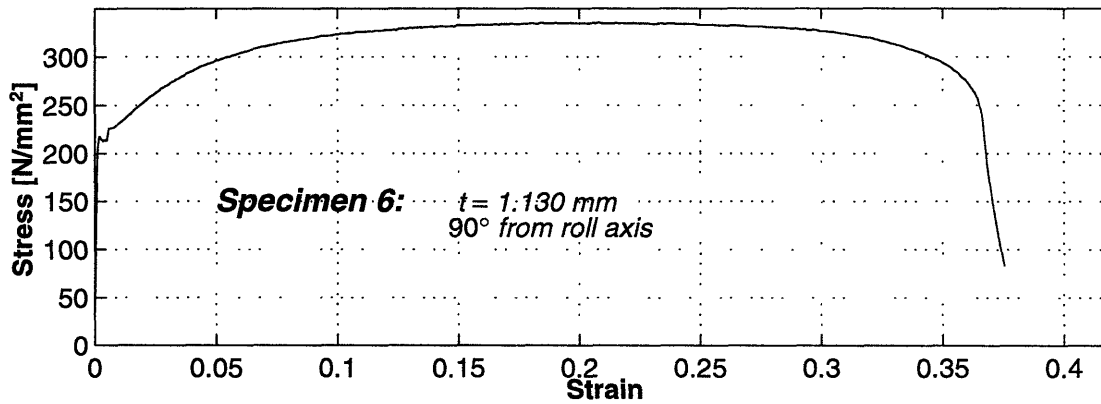**Figure D.13:** Engineering Stress-Strain Curve for Specimen 5

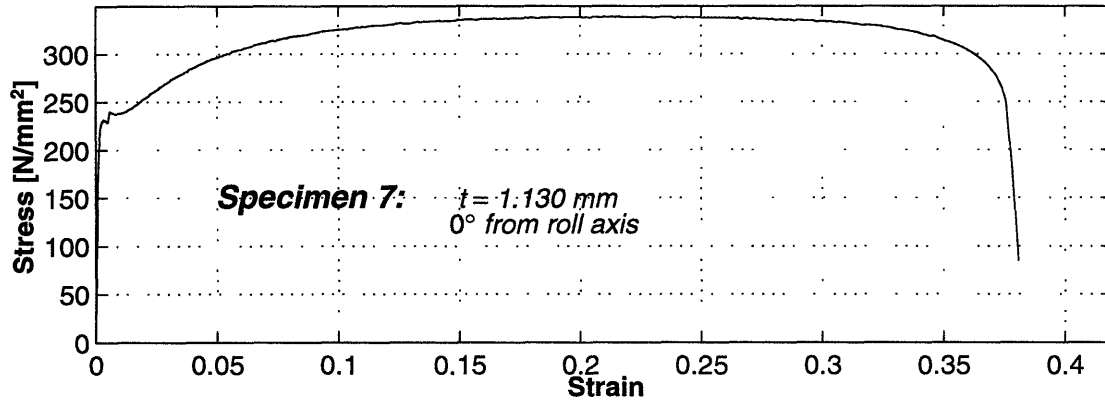**Figure D.14:** Engineering Stress-Strain Curve for Specimen 6

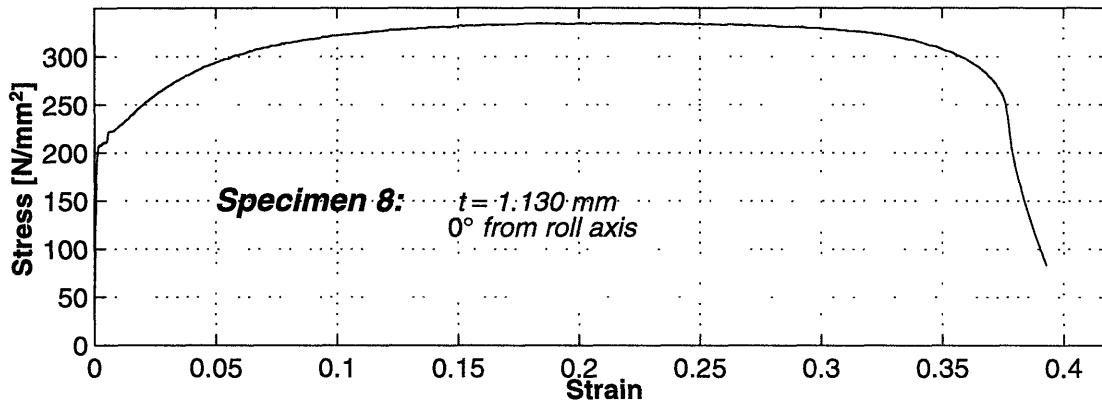**Figure D.15:** Engineering Stress-Strain Curve for Specimen 7

Figure D.16: Engineering Stress-Strain Curve for Specimen 8